UAH Research Report No. 181

# STUDIES ON IMMISCIBLE ALLOYS

by

Guenther Otto

FINAL REPORT

Prepared for

National Aeronautics and Space Administration
George C. Marshall Space Flight Center
Marshall Space Flight Center, Alabama 35812
Under Contract NAS8-27809

Submitted by

The University of Alabama in Huntsville
School of Graduate Studies and Research
Huntsville, Alabama 35807

January 1976

UAH Research Report No. 181

# STUDIES ON IMMISCIBLE ALLOYS

by

Guenther Otto

FINAL REPORT

Prepared for

National Aeronautics and Space Administration
George C. Marshall Space Flight Center
Marshall Space Flight Center, Alabama 35812
Under Contract NAS8-27809

Submitted by

The University of Alabama in Huntsville
School of Graduate Studies and Research
Huntsville, Alabama 35807

January 1976

## PREFACE

This Final Report contains the results of work performed during the period of 1 June 1973 to 31 October 1975 under Phase B of Contract NAS8-27809. The achievements are derived from a cooperative research effort between the Space Sciences Laboratory of NASA/Marshall Space Flight Center and The University of Alabama in Huntsville using the MSFC drop tower and the facilities of the Space Sciences Laboratory.

The investigation deals with the electrical and metallurgical properties of immiscible alloys solidified during free-fall conditions. Although the low-gravity duration in this installation is limited to four seconds, meaningful solidification experiments with immiscible alloys can be performed. This report also deals with two Skylab Science Demonstrations: TV-102 "Immiscible Liquids" and TV-111 "Ice Melting." These experiments were not part of the original contract but provided an opportunity to study longer term low-gravity effects.

Results of work performed during the period of 1 July 1971 to 31 May 1973 are presented in the UAH Interim Research Report No. 174, entitled "Superconducting Compounds and Alloys Research."

ACKNOWLEDGMENTS

We would like to thank Dr. L. L. Lacy of MSFC for the successful cooperation and the helpful support during the course of this work. Mr. I. C. Yates supplied us with the Ga-Bi samples and their processing parameters. The particle size distribution was evaluated by Mrs. K. West.

The technical assistance provided by Mr. D. Homesley and Mr. D. Hardin of UAH is also appreciated.

## OBJECTIVES

The objectives of this contract were (1) to demonstrate that the available free fall time of up to 4 seconds in the MSFC drop tower is sufficient to conduct solidification experiments with immiscible alloys, (2) to show the influence of zero-gravity solidification on the metallurgical microstructure, (3) to evaluate some physical properties of such alloys in regard to their microstructure, and (4) to show that there is a gravitational influence on the coalescence rate of liquid droplets.

## ACHIEVEMENTS

1. Performed meaningful solidification experiments with Ga-Bi immiscible alloys in a drop-tower.
2. Prepared homogeneous dispersions of immiscible metals in bulk form.
3. Demonstrated that the microstructure influences the physical properties of the alloys.
4. Showed that the electrical properties of Ga-Bi alloys are affected by low-gravity solidification so that a peak in the resistivity occurs, and semiconducting properties result.
5. Established a correlation of the property change with the particle size and interfacial area of the dispersant and predict full semiconducting behavior of Ga-Bi alloys with particles of 0.1 μm diameter and less.
6. Found that coalescence and creaming are essentially eliminated in zero-gravity, whereas these processes are dominant in one-gravity.
7. Eight publications and six reports.

## ABSTRACT

When dispersed or mixed immiscibles are solidified on earth, a large amount of separation of the constituents takes place due to differences in densities. However, when the immiscibles are dispersed and solidified in zero-gravity, density separation or creaming does not occur, and homogeneous composite alloys can be formed with many new and promising properties. By measuring the electrical resistivity and the superconducting critical temperature of zero-gravity processed Ga-Bi samples, it has been found that the electrical properties of such materials are different from the basic constituents and the ground-control samples. The degree of dispersion critically controls the temperature dependence of the electrical resistivity with the finest dispersions showing the greatest impact. Our results indicate that the changes in basic properties are associated with the amount of interfacial area formed.

To illustrate the behavior of immiscible liquids of different densities in zero-gravity and to determine the rate of coalescence of like droplets, a demonstration experiment (TV-102) was performed on the Skylab 4 mission. Dispersions of oil-in-water and of water-in-oil were prepared by the astronauts and their appearance photographed over a time span of 10 hours. The experiment indicates that all emulsions were stable over this period and that the coalescence rate was at least $3 \times 10^5$ times smaller on Skylab than on earth.

The recorded melting of a cylindrical piece of ice on Skylab 3 (TV-111) is used to study the mode of heat transfer for the latent heat of melting in low-gravity.

TABLE OF CONTENTS



* Co-Investigator: Dr. L. L. Lacy, MSFC

LIST OF FIGURES

Nomenclature and Reference Data for Gallium-Bismuth Samples

| NASA Code | Gravity Level ('g') | Soak Temp. (°C) | Cooling Rate (°C/sec)* | Av. Particle Diam. (μm) | Mean Standard Deviation (μm) |
|---|---|---|---|---|---|
| 2-4 | 0.04 | 270 | 5800 | 0.9 | 0.7 |
| 5-6 | < 0.002 | 346 | 5200 | 1.2 | 0.7 |
| 9-2 | 0.04 | 405 | 7000 | 3.2 | 1.7 |
| 1-3 | 1.0 | 375 | N/A | ~ 20 | - |
| B-5 | 1.0 | 325 | 2950 | N/A | - |
| C-6 | 0.005 | 328 | 954 | 2.5 | 1.3 |
| D-2 | 0.004 | 324 | 2550 | 2.9 to 5.1 | - |
| E-4 | 0.005 | 336 | 3371 | N/A | - |
| F-9 | < 0.002 | 313 | 1920 | 2.0 | 1.2 |
| G-10 | < 0.002 | 318 | 452 | 2.3 | 0.7 |
| H-11 | 0.004 | 315 | 236 | 2.2 | 0.9 |
| J-12 | 1.0 | 316 | 219 | 1.6 to 7.9 | - |
| K-13 | 0.005 | 320 | 209 | N/A | - |
| L-14 | 0.004 | 349 | 279 | 2.5 | 0.9 |
| O-11 | 0.005 | 252 | 5500 | 3.0 | 1.0 |
| O-12 | 0.005 | 480 | 5500 | 2.5 to 4.5 | - |
| O-13 | 0.005 | 265 | 5500 | 3.0 | 1.0 |

* Cooling rate determined on outside of tantalum container. The cooling rate inside the samples will be less.

Remarks: In earlier publications, like Ref. [32], sample (2-4) is called (A), (5-6) = (B), (9-2) = (C) and (1-3) = (D).

# I. INTRODUCTION

At the boundary of two phases matter shows properties which are different from those of the continuous phase. The free energy, entropy and volume of molecules forming an interface between two liquids are modified and differ from the corresponding properties of the same molecules in the pure liquid. Ordinarily, the contribution of the free surface energy to the total free energy is negligible. However, in dispersed immiscible systems, the ratio of the surface to volume can be large, and the bulk properties of such a solidified alloy will be modified to a large extent by interface effects [1].

A recent study of existing phase diagrams [2] revealed that there are about 500 binary alloy systems composed of two metals or metallic oxides showing immiscibility in their liquid state and demonstrated that the phenomenon of immiscibility is rather common. But, since the two liquids usually have different densities, gravity-induced segregation after the dispersion will occur, and the two components finally separate by creaming or by coalescence. The times for segregation can be very short and are in the order of seconds for common material systems [3].

In earth orbit, however, density differences of the liquid components are no longer important, and homogeneous dispersions of these immiscibles can be obtained which are stable over a long period of time. The absence of density segregation allows processing and solidification of immiscible alloys with new materials systems, which cannot be made on earth because of

rapid separation. These low-gravity processed immiscibles may have a wide range of applications, as in dispersion-strengthened or superplastic alloys, superconducting wires, permanent magnets, bearing materials or catalysts to give a listing of TRW [2]. In addition, materials in high-power switches could be devised with immiscible alloys where one component acts as current carrier and the other as the wear-resistant base.

The nature of the reported investigations is to determine the influence of low-gravity processing on the electrical and physical properties of immiscible alloys. The principle of free fall solidification has been verified by cooling Ga-Bi alloys through the miscibility gap during the 4 seconds of free fall in the MSFC drop tower [2, 4]. From the multitude of potential experimental investigations that could be conducted [5], we have limited ourselves to determining some of the physical processes associated with low-gravity solidification and the electrical properties of such solidified immiscibles. By means of a Skylab demonstration [6, 7], the long-term stability of two dispersed immiscible liquids prior to solidification will be investigated.

In addition, the melting of a cylindrical piece of ice at ambient temperature could be performed in a low-gravity environment during the Skylab 3 mission [6, 7]. The observed melting behavior, which is different from the ground control melting, will be described by considering surface tension effects and the lack of convective heat transfer on Skylab.

## II. INVESTIGATIONS ON GALLIUM-BISMUTH IMMISCIBLE ALLOYS

### 1. Sample Preparation

A dispersion of two liquid metals can be obtained by making use of the miscibility gap occurring in several metallic constitution diagrams [8]. With this technique, the application of a mechanical mixing device is not necessary. Samples of Ga-Bi, having a liquid miscibility gap between 262 and 222 °C as can be seen from the phase diagram in Fig. 1, were processed during 4 seconds of free fall in the MSFC drop tower [9]. In this time span, the single-phase metallic liquid (with a temperature above 262 °C) was cooled through the liquid-miscibility gap to form two liquid phases, and subsequently two phases were solidified in low-gravity by water quenching. These samples should show no density segregation or coalescence. Ground-control samples were processed under otherwise identical conditions except that the samples were not dropped in the drop tower. A representative cooling curve for a drop tower sample (H-11) is given in Fig. 2. The consolute and the first monotectic temperature (Bi solidification) are indicated by broken horizontal lines.

The Ga-Bi samples were housed in rectangular tantalum containers (1.27 x 0.635 x 0.318 cm), using metals with at least 99.999 percent purity and a concentration of 50 at.% of each element. Bismuth and gallium were separately loaded into the container under argon atmosphere and the containers were sealed by electron beam welding. Since both bismuth and gallium expand upon solidification, a small expansion volume (0.2 $cm^3$)

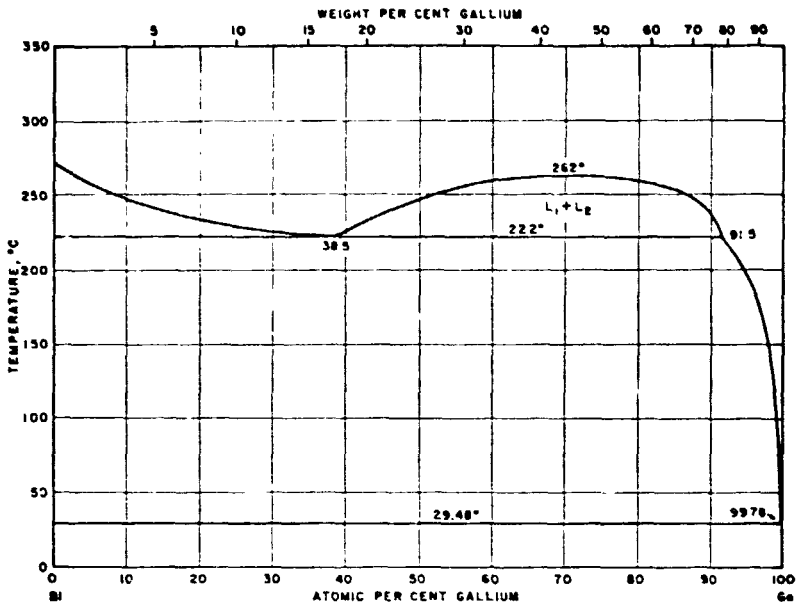


Figure 1. The phase diagram of the system bismuth-gallium [8].

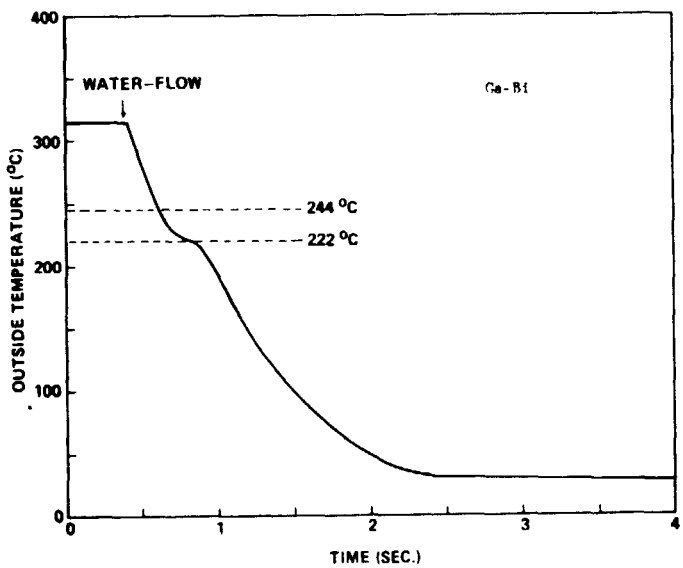


Figure 2. Cooling curve for a drop tower sample.

was left in each capsule. In order to exclude the influence of one variable, the concentration of the elements was not changed. Details of the processing procedure are given by Reger and Yates [4].

Thin slices with a thickness of about 1 mm, which had been cut with a wire saw from the original samples, were investigated for their metallurgical, electrical, and superconducting properties [10]. These samples are listed with the appropriate NASA code and preparation parameters in Table 1.

Also included in this table are the three samples, 011, 012 and 013, which were solidified in cylindrical graphite containers and thus differ in geometry and in container material from the other samples. These alloys were prepared during the performance test for a new cylindrical heating element developed at MSFC.

## 2. Microstructure

### a. Density Segregation

Once the samples are cooled below 240 °C into the two liquid regions, gallium particles (with 38.5 at.% Bi dissolved) will precipitate according to the phase diagram of Fig. 1. Since the decomposition of a liquid phase into two liquid phases as

$$L \rightarrow L_1 + L_2 \qquad (1)$$

is involved in the process, the diffusion coefficient ($D \approx 10^{-4}$ cm$^2$/s) can be assumed to be sufficiently large so that equilibrium conditions are maintained during decomposition. The densities of the liquids at 250 °C for Bi and Ga are 10.07 and 6.17 g/cm$^3$, respectively, which will cause the gallium droplets to move upwards to the surface. The velocity of the

TABLE 1

Reference Data for Gallium-Bismuth Samples

| NASA Code | Gravity Level ('g') | Cooling Rate* (°C/sec) | Av. Particle Size (μm) | Mean Standard Deviation (μm) | No. of Particles ($10^6$ per $cm^2$) |
|---|---|---|---|---|---|
| 2-4 | 0.04 | 5800 | 0.9 | ± 0.7 | 27 |
| 5-6 | < 0.002 | 5200 | 1.2 | ± 0.7 | - |
| 9-2 | 0.04 | 7000 | 3.2 | ± 1.7 | 2.1 |
| 1-3 | 1.0 | N/A | ~ 20 | - | - |
| B-5 | 1.0 | 2950 | N/A | N/A | 4.1 |
| C-6 | 0.005 | 954 | 2.5 | ± 1.3 | 4.0 |
| D-2 | 0.004 | 2550 | 5.1 | to 2.9 | 2.8 |
| E-4 | 0.005 | 3371 | N/A | N/A | - |
| F-9 | 0.002 | 1920 | 2.0 | ± 1.2 | 2.1 |
| G-10 | < 0.002 | 452 | 2.3 | ± 0.7 | 4.2 |
| H-11 | < 0.004 | 236 | 2.2 | ± 0.9 | 5.2 |
| J-12 | 1.0 | 219 | 1.6 to 7.9 | - | 1.52 |
| K-13 | 0.005 | 209 | N/A | - | - |
| L-14 | 0.004 | 279 | 2.5 | ± 0.9 | 3.7 |
| O-11 | 0.005 | 5500 | 3.0 | ± 1 | 1.3 |
| O-12 | 0.005 | 5500 | 2.5 to 4.5 | - | 0.52 |
| O-13 | 0.005 | 5500 | 3.0 | ± 1 | 1.2 |

*Cooling rate determined on outside of tantalum container. The cooling rate inside the samples will be less.

particles is controlled (in the absence of convective currents) by a modified Stoke's equation [3] which states that for a spherical particle of radius r in a liquid of the viscosity $\eta$, the velocity is given by

$$v = 2gr^2(\rho_1 - \rho_2)/9\eta \qquad (2)$$

where $\rho_1$ and $\rho_2$ are the density of the two liquids and 'g' is the acceleration of gravity. Calculated velocities of gallium droplets with different diameters, traveling in liquid bismuth are listed in Table 2, along with the distance (in terms of the particle radii) the particles will travel in one second.

TABLE 2

Velocities of Ga Droplets in Liquid Bi at ~225 °C

| Radius of Ga Droplet (μm) | Drift Velocity (mm/sec) | Radii Traveled in One Sec. |
|---|---|---|
| 1000 | 520 | 520 |
| 100 | 5.2 | 52 |
| 10 | 0.052 | 5.2 |
| 5 | $13 \times 10^{-3}$ | 2.6 |
| 2 | $2.1 \times 10^{-3}$ | 1.1 |
| 1 | $0.52 \times 10^{-3}$ | 0.5 |

For very small particles below 1 μm, the drift-velocity due to gravity is small and may be neglected. However, a particle with a radius of 5 μm travels in one second a distance which is already larger than its diameter. Micrographs of two samples solidified under the same conditions in zero-gravity and in one-gravity are given in Fig. 3. It can be seen that the low-gravity solidification leads to a uniform dispersion of gallium particles in a bismuth matrix. The shape of the gallium droplets appears to be about circular and an average diameter of 2.5 μm can be given. The

GRAVITY EFFECTS ON THE MICROSTRUCTURE OF GA - Bi

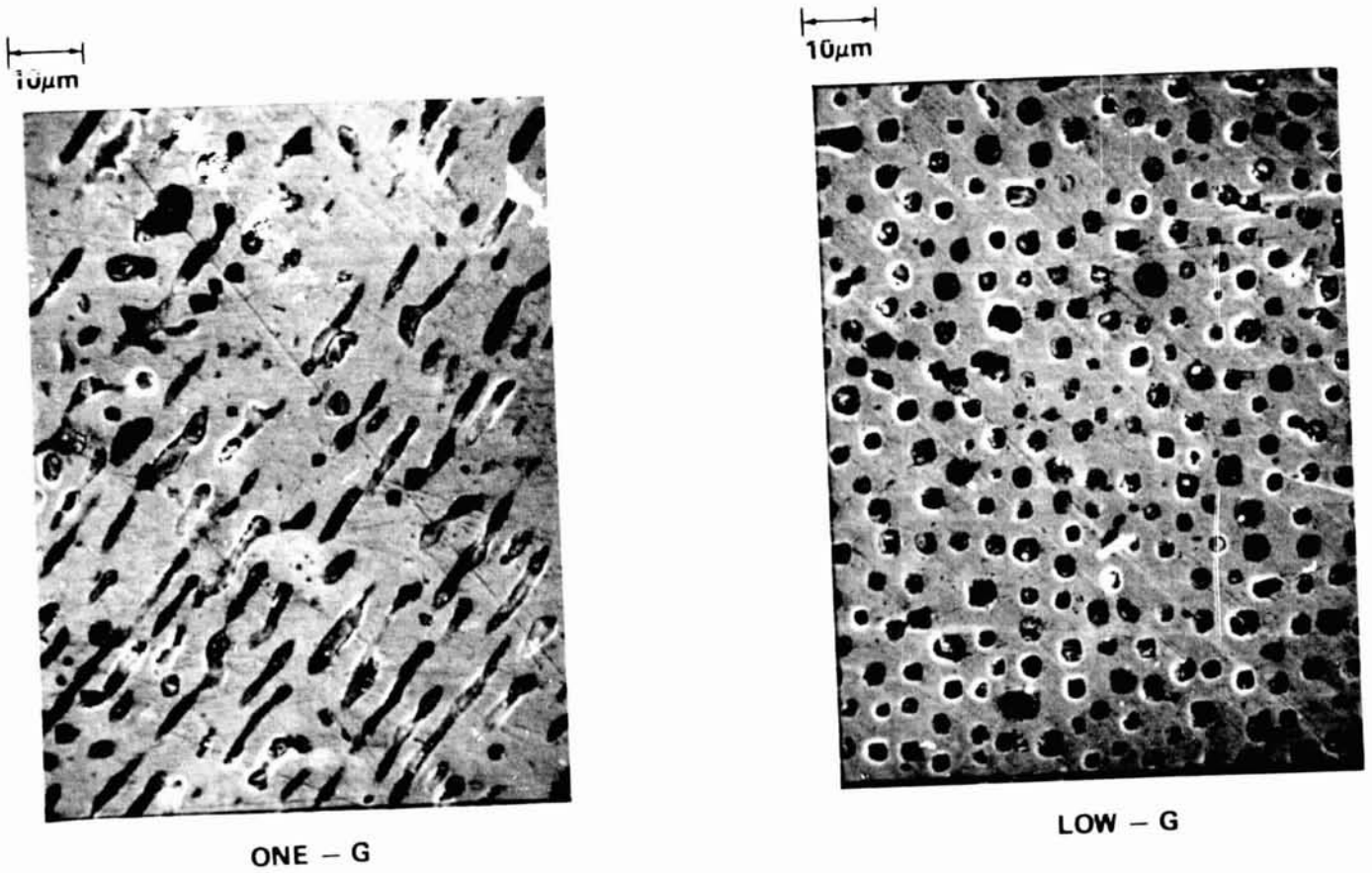


Figure 3: The effects of gravity on the microstructure of Ga-Bi alloys. Sample J-12 processed in one-g, sample L-14 processed in low-g. 1000 X.

sample which was solidified in one-g also exhibits a dispersion of gallium in bismuth. However, the particles are not spherical and they obviously become elongated by coalescence during the process of density segregation.

### b. Photomicrographs

Photomicrographs of additional samples are reproduced in Figs. 4, 5, and 6. The light colored areas in the photographs represent the Bi matrix, and the darker circular areas are the dispersed gallium particles. As expected, the low-gravity processing always resulted in a fine and uniform dispersion of Ga particles in the Bi matrix. The processing parameters for these samples as gravity level during solidification, soak temperature, particle size and standard deviation from average particle size are listed in Table 1.

Particle diameters on the photomicrographs were measured with the following technique: A number of straight lines in arbitrary directions were drawn on the photomicrographs. From those particles, which were touched or crossed by a line, the diameter was measured in two orthogonal directions. Measurements were made on a large number of particles, ranging between 100 and 200. The distribution of particle diameters for two drop tower samples are presented in Fig. 7. Sample L-14 shows a nearly gaussian particle distribution with an average diameter of 2.5 μm. The particles in this alloy are of very uniform appearance and the sample has practically no droplets above 5 μm diameter. This observation is in contrast to ground-control sample J-12 which shows a large number of elongated particles, and, therefore, a second maximum in the diameter above 5 μm becomes apparent.

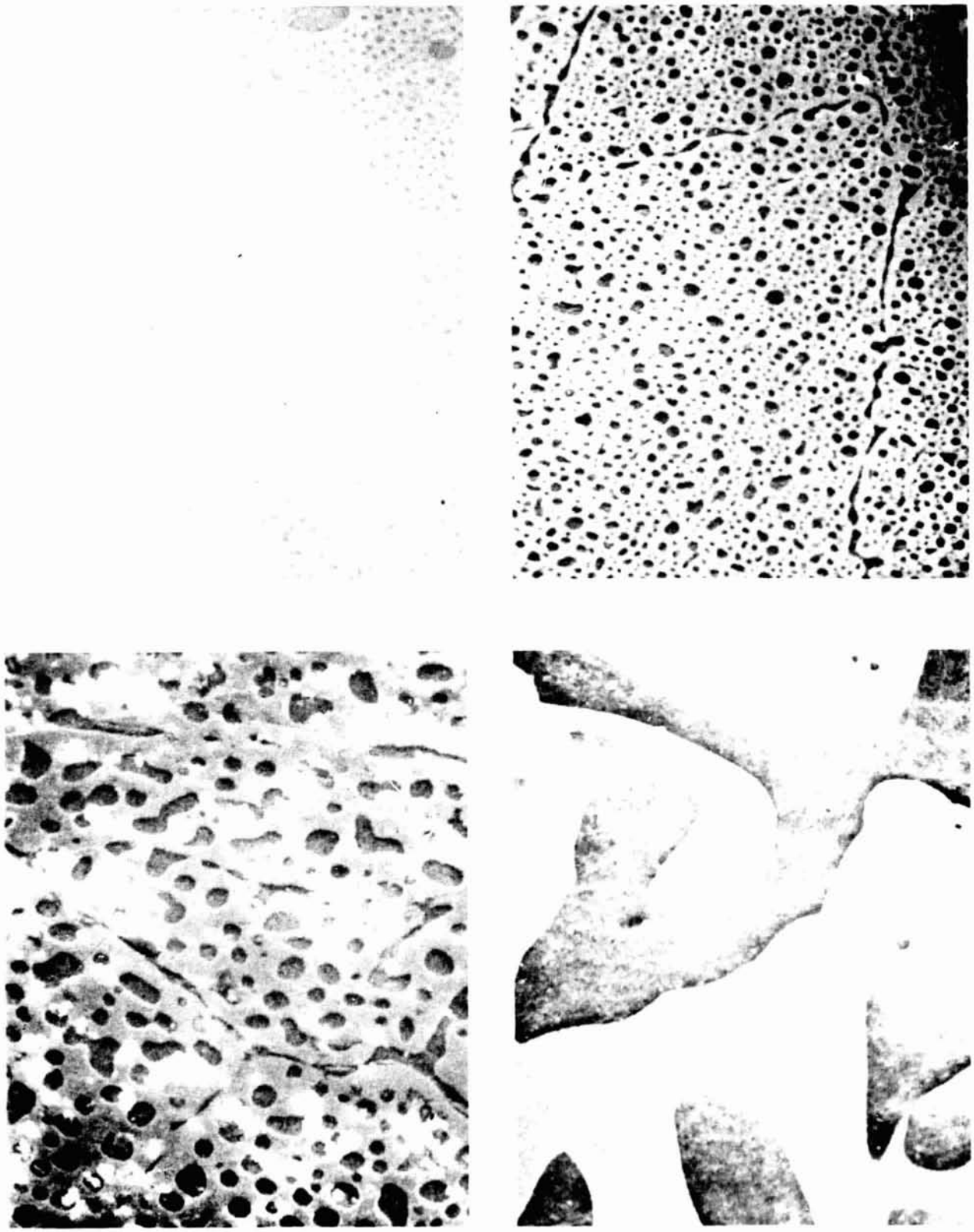

Figure 4. The microstructure of low-gravity solidified Ga-Bi alloys. Photo (d) is from a ground-control (one-g) sample. The dark areas represent gallium particles, the light regions are the bismuth matrix. (a) Sample (2-4), (b) Sample (5-6), (c) Sample (9-2), (d) Ground-control sample (1-3). 1000 X.

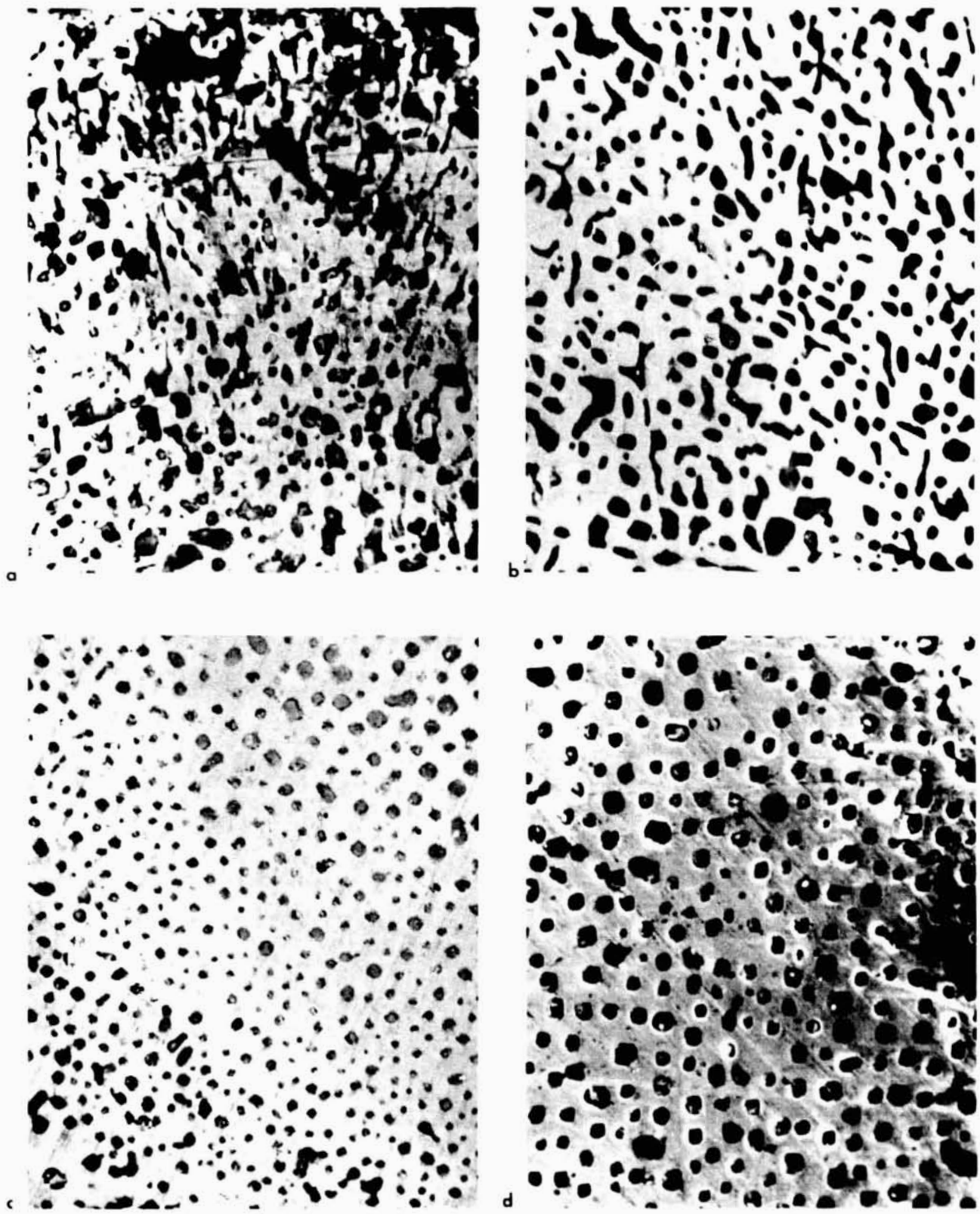


Figure 5. The microstructure of low-gravity solidified Ga-Bi alloys. Photo (a) is from a ground-control (one-g) sample. (a) Ground-control sample (B-5), (b) Sample (C-6), (c) Sample (H-11), (d) Sample (L-14). Magnification 1000 X.

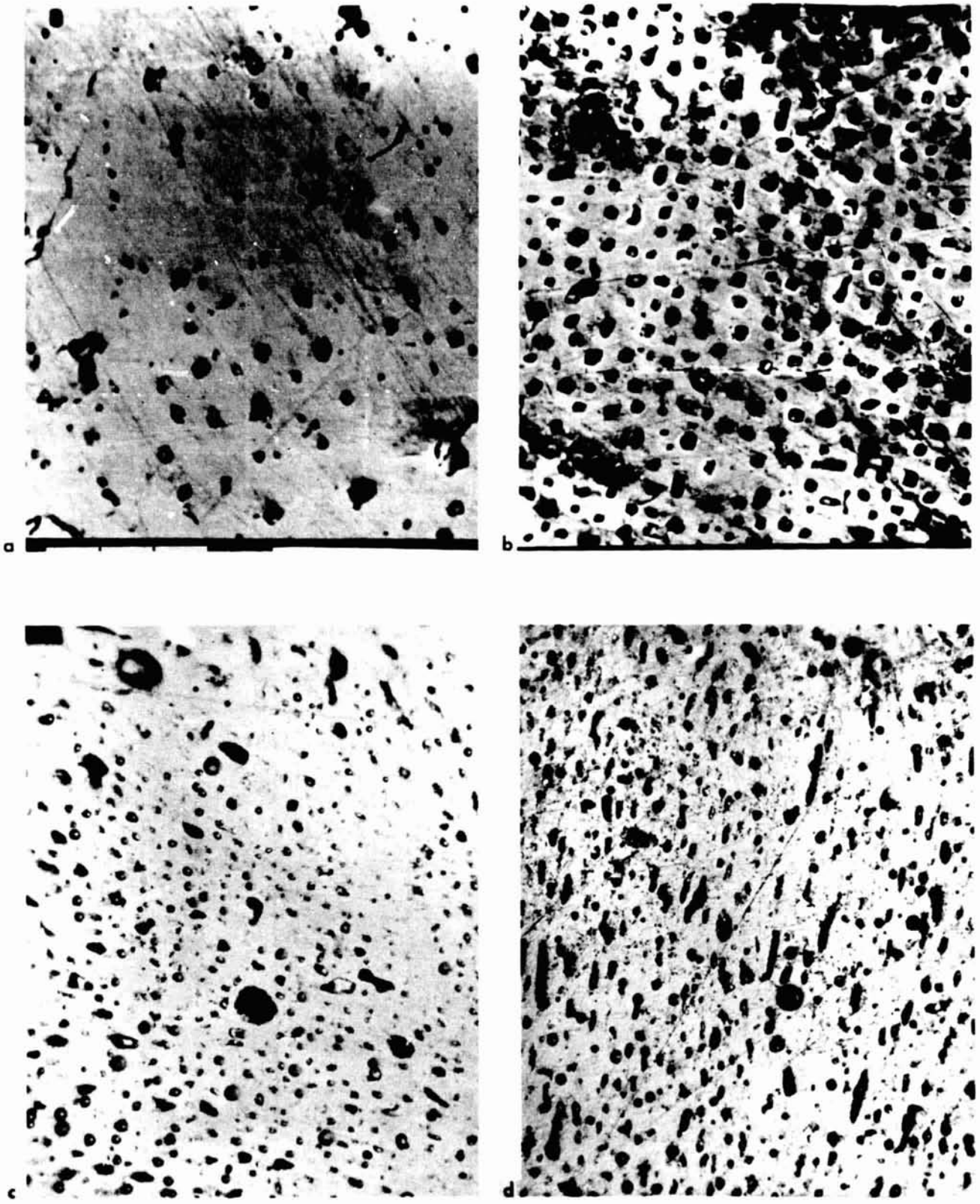


F ;ure 6. The microstructure of low-gravity solidified Ga-Bi alloys. (a) Sample (F-9), (b) Sample (G-10) 1000 X, (c) Sample (0-11), (d) Sample (0-13) 500 X.

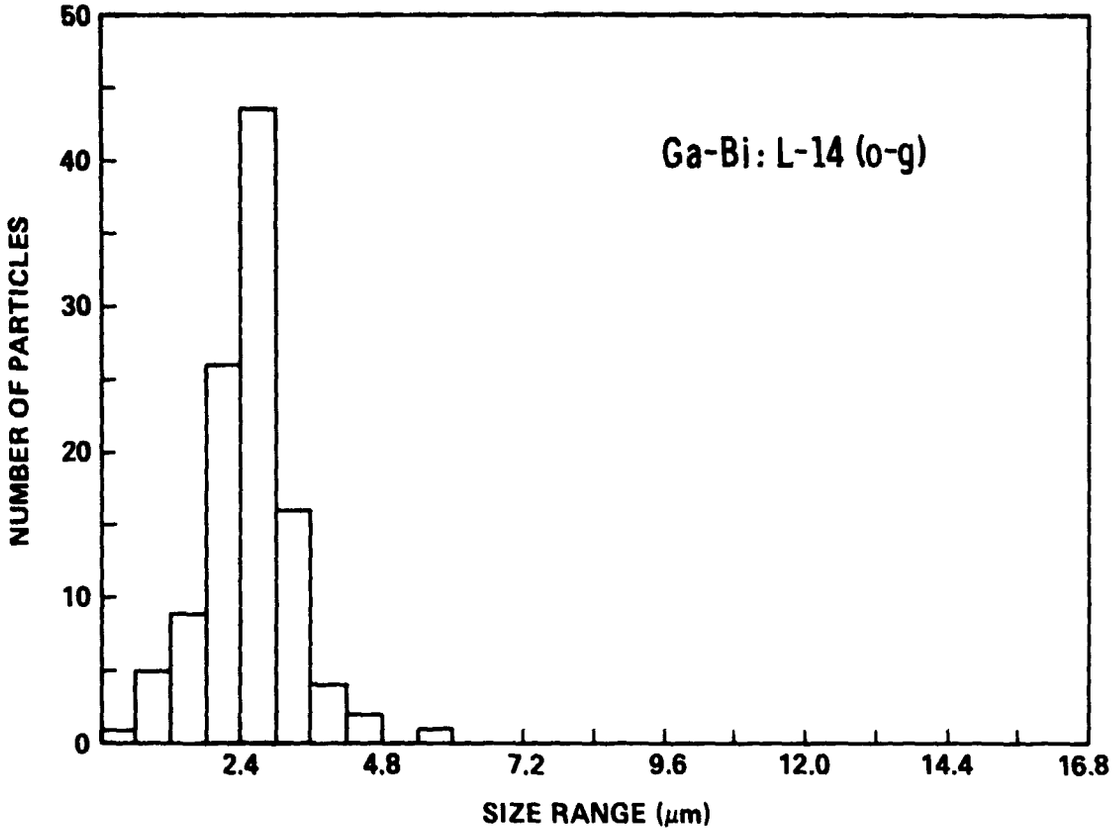


Figure 7. Particle size distribution for low-g and one-g processed samples.

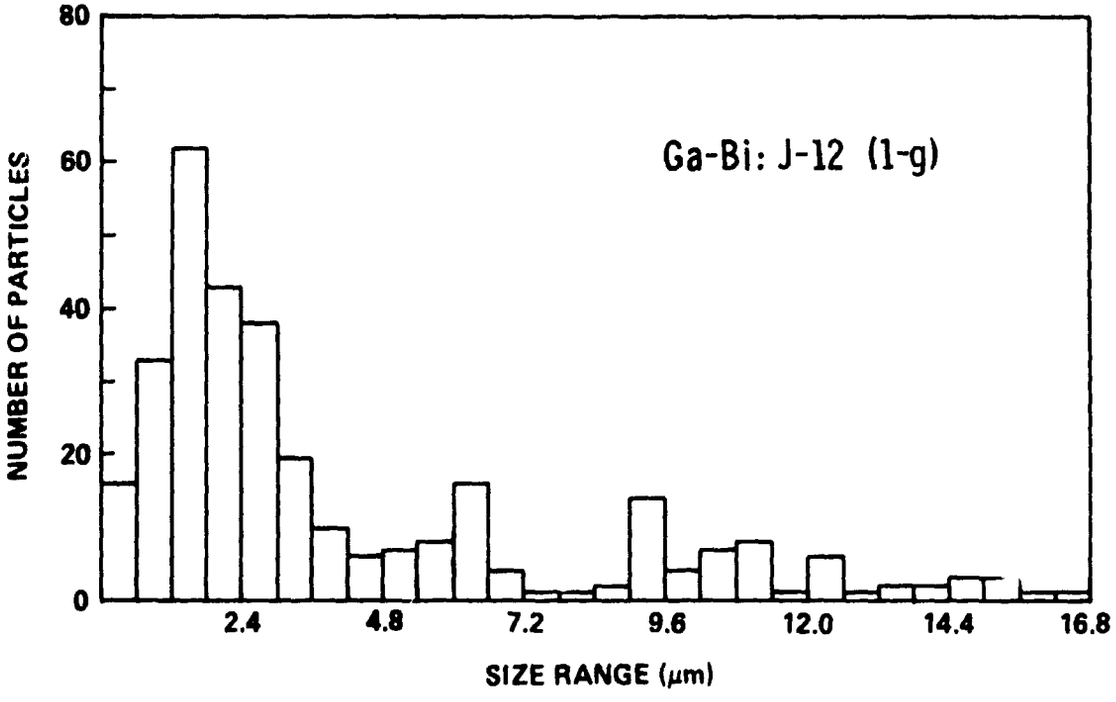

The average number of particles per $cm^2$ has been computed from the photomicrographs which all have a magnification of 1000X. The Ga particles were counted in the total picture area of 103 x 89 μm. The number of particles per $cm^2$ is also listed in Table 1.

For completeness, we also give low-magnification micrographs in Fig. 8 of particular areas of sample 011, 012, and 013. These samples do not fit very well in the above considerations because of several unusual features and it may be possible that the cylindrical configuration of the capsules has further influenced the resulting microstructure. We note a number of large voids which could have been filled with gallium before polishing. There are also areas with a cell-like structure showing different particle configurations which may have resulted from convective material currents prior to quenching. In the micrographs of Fig. 8, we also realize banded regions which are completely void of gallium particles. It is likely that the cellular structure represents a pseudo-electric solidification pattern, experiencing a fast progressing solidification front, as was observed by Chadwick [11] in lead-cadmium alloys. This inhomogeneous appearance has not been observed on the low-g solidified samples with a rectangular cross section, which will be investigated solely further.

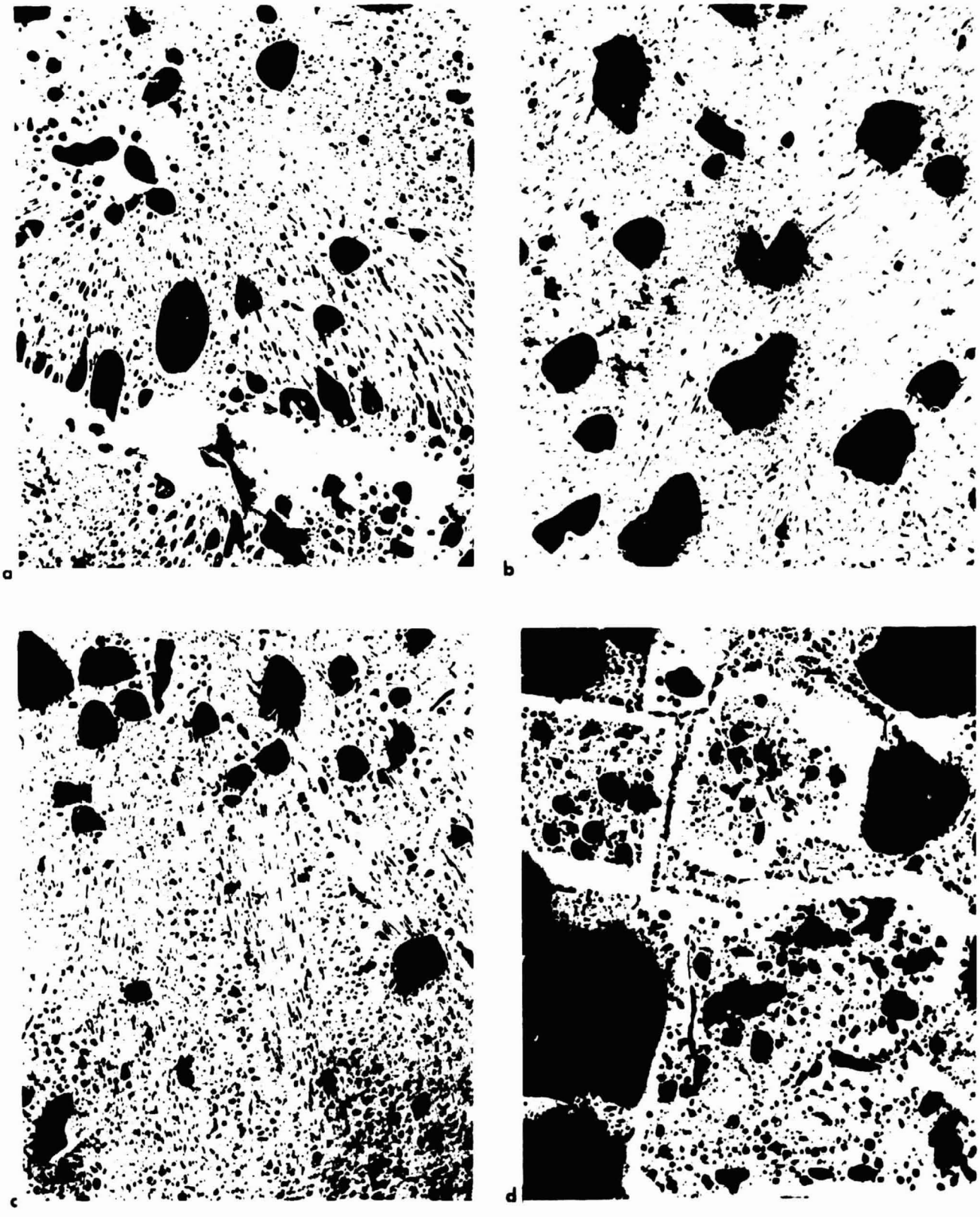


Figure 8. The microstructure of Ga-Bi alloys solidified in cylindrical containers during low-gravity conditions. (a) Sample (0-11), (b) Sample (0-12), (c) Sample (0-13) all center area, (d) Sample (0-13) border area. The dark areas are large voids. 100 X.

## c. Fineness of Dispersion

It can be seen from the micrographs and from the diameters listed in Table 1 that the low gravity processing leads to homogeneously dispersed samples. However, there is considerable variation of the particle size for the different drop tower specimens. Since the nucleation and growth of gallium particles is affected by the cooling rate, we expect this parameter to have a major influence on the particle size.

Some information about the quantities involved can be given by the classical theories of nucleation which were developed by Becker and Döring [12] and Turnbull and Fisher [13]. The nucleation rate, I, in liquid/liquid systems is determined by an expression of the type

$$I = K \exp(-[\Delta G^* + \Delta G_A]/kT) \qquad (3)$$

where $\Delta G^*$ is the work of nucleation (i.e. tne change in free energy necessary for a nucleus to form) and $\Delta G_A$ is the energy of activation for diffusion across the boundary separating the phases; k is the Boltzmann constant. Thus, the rate is a combination of two terms having the required change of free energy in connection with the probability of an atom diffusing to the subcritical nucleus. The form of Eq. (3) means that the rate of nucleation will be extremely sensitive to the undercooling, $\Delta T$, which determines the term $\Delta G^*$. Undercooling of 25% below the melting temperature (absolute) has been found for the nucleation of solids from liquids [14]. At this amount of undercooling, the critical radius of the droplets is about $10^{-3}$ μm, and the nucleus would contain approximately 200 atoms.

In order to obtain a finely dispersed alloy by increasing the nucleation rate, a high degree of supercooling is required. One way to achieve a large supercooling is by fast quenching. In our case, the samples are cooled rapidly through the miscibility gap by spraying the container with water and different cooling rates may have been obtained. Cooling data are available for the drop tower samples, and in Fig. 9, we have plotted the average particle diameter of the different samples against the cooling rates. There is a large scatter in the data and no clear trend can be recognized. For several samples, it appears as if the particle size is independent of the indicated cooling rate. In this case, it is most likely that the cooling rates, which were determined with a thermocouple mounted on the outside of the sample, do not represent the true cooling rates inside the sample. Since for inside areas the true cooling rate is determined by the heat flow through the liquid alloy, this heat flow is limited by the conduction mechanism and should not exceed a rate of about 400 °C/sec for the specified geometry [51]. We, therefore, believe that the true cooling rates inside the samples are between 200 and 400 °C/sec and are not clearly related to the indicated cooling rates.

To better resolve the influence of cooling rate on particle size in low-gravity, a slow cooling experiment with a rate of about one degree per second would be helpful. Such a slow cooling rate, which cannot be realized in the drop tower, would be sufficiently distant from those rates already obtained that the uncertainty of the drop tower cool rates would become insignificant. However, a zero-gravity duration of about 3 minutes is required for such experiment.

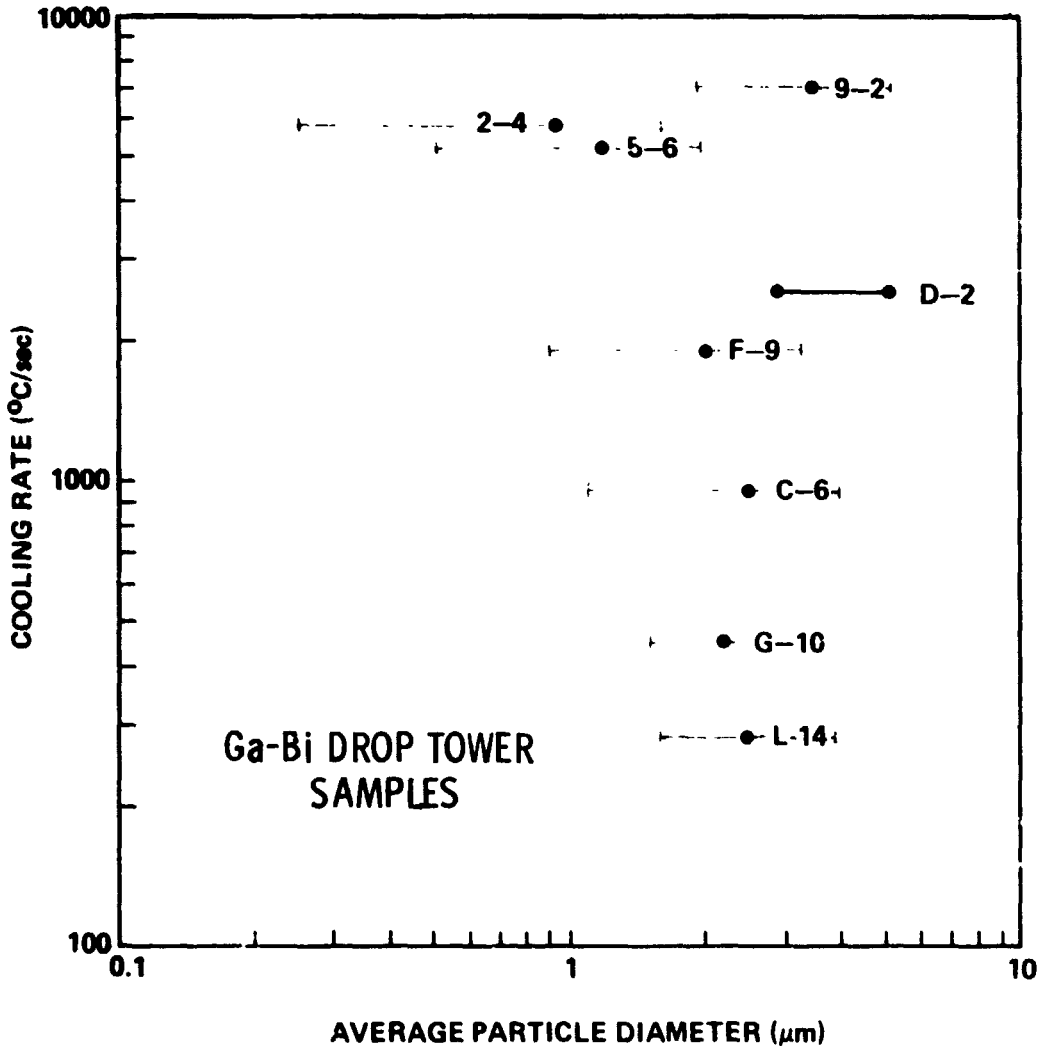


Figure 9. The influence of the indicated cooling rate on the average particle diameter of gallium. The error bars indicate the range of particle size distribution.

## 3. Resistivity Measurements

Changes in the electrical properties of bismuth due to the presence of dispersed gallium can be determined by resistivity measurements. In the case of coarse metallic mixtures where the two components are mutually insoluble, the resistivity of the mixture is expected to be roughly the weighted average in terms of the volume of the two conductivities. However, when the dimensions of the second phase come in the magnitude of the mean free path of the electrons, large interfacial scattering contributions should occur, which can be determined by this nondestructive technique. In the following, we wish to show that the electrical properties of these dispersed alloys are influednced by the microstructure.

### a. Measuring Techniques

The temperature dependence of the electrical resistivity, $\rho(T)$, was measured on thin slices of material (dimensions: 1.0 x 0.3 x 0.1 cm) with the conventional four-probe technique. A constant current of 10 mA was passed through the sample by means of fine spring-loaded copper wires contacted to the alloy by silver conductive paint. The corresponding voltage drop was measured on two separate potential leads and could be recorded as a function of temperature. The sample temperature was measured with a calibrated platinum-resistance thermometer to 20K and below this temperature with a calibrated germanium-resistance thermometer. A schematic of the experimental set-up is given in Fig. 10. An absolute determination of the resistivity for all samples is limited by the small sample geometry to within 8%, indicated by a room temperature error bar. However, the relative values of $\rho$ for a given curve are accurate to better than 1%.

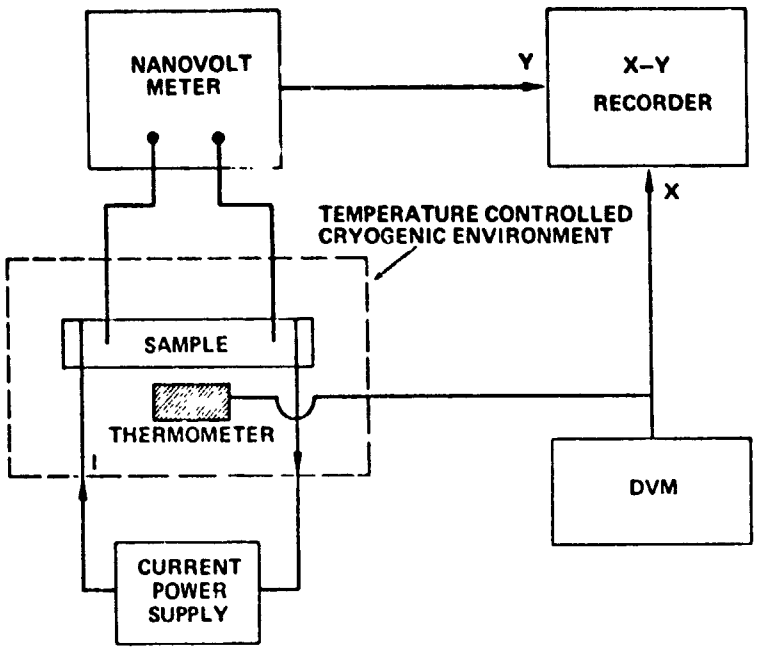


Figure 10. Block diagram for resistive measurement of the transition temperature.

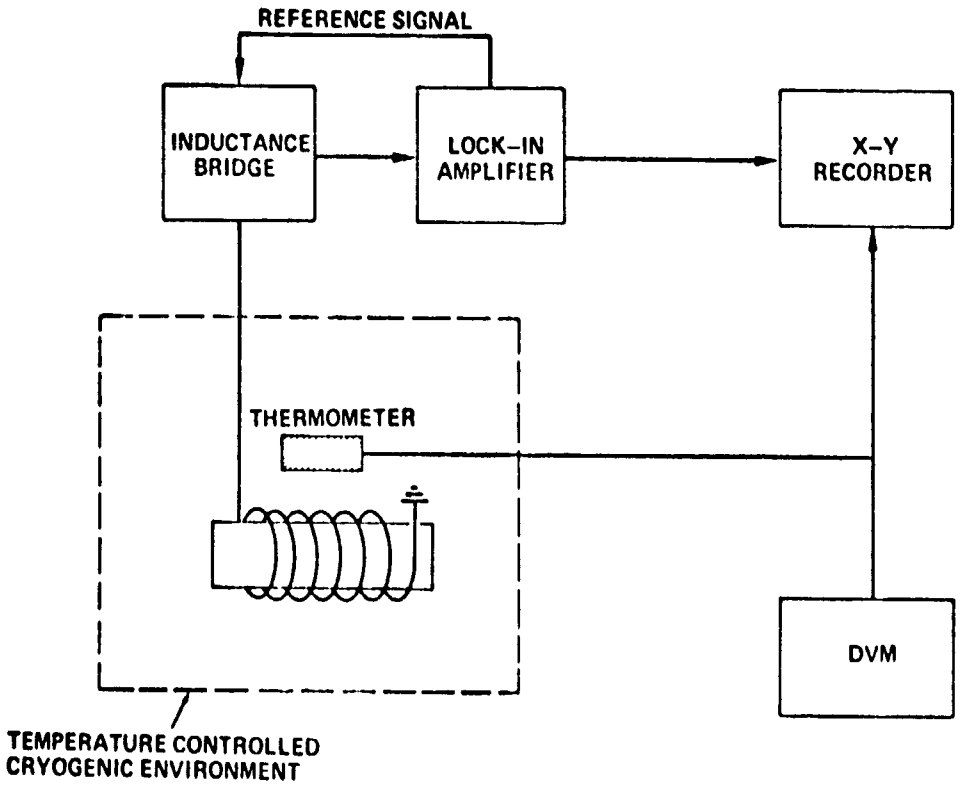


Figure 11. Block diagram for inductive measurement of the transition temperature.

Superconducting transition temperatures were measured by the inductance technique. A schematic of the experimental set-up is given in Fig. 11. The sample is placed inside a coil and the temperature-dependent change in inductance is measured with a bridge circuit. The material becoming superconducting exhibits diamagnetism (Meissner-Ochsenfeld Effect) and excludes the magnetic flux from its volume, thereby changing the inductance of the coil. In order to increase the sensitivity of the system and to reduce susceptibility to noise, the a-c signal is processed in a lock-in amplifier. The advantage of this method, in addition to its high sensitivity, is that the volume of the superconducting phase can be determined in a multiphase alloy by calibration with a known superconducting volume.

b. Resistivity Curves

The results of the resistivity measurements in the temperature range between 4.2 and 290 K are given in Figures 12a and 12b. Each letter and number on the curves refers to the sample whose preparation parameters are identified in Table 1. For comparison, the resistivities of pure Bi and pure Ga [15] have also been included in Fig. 12a. The room temperature value for all samples is approximately the same as for the pure Bi. An absolute determination of $\rho$ for all samples is limited to within 8 percent by the sample geometry, as indicated by the room-temperature error bar. However, the relative values of $\rho$ for a given curve are accurate to better than 1 percent. What is of interest here is that the changes in resistivity as a function of temperature for the samples are quite different and that a peak develops in the resistivity of some samples at about 100 K.

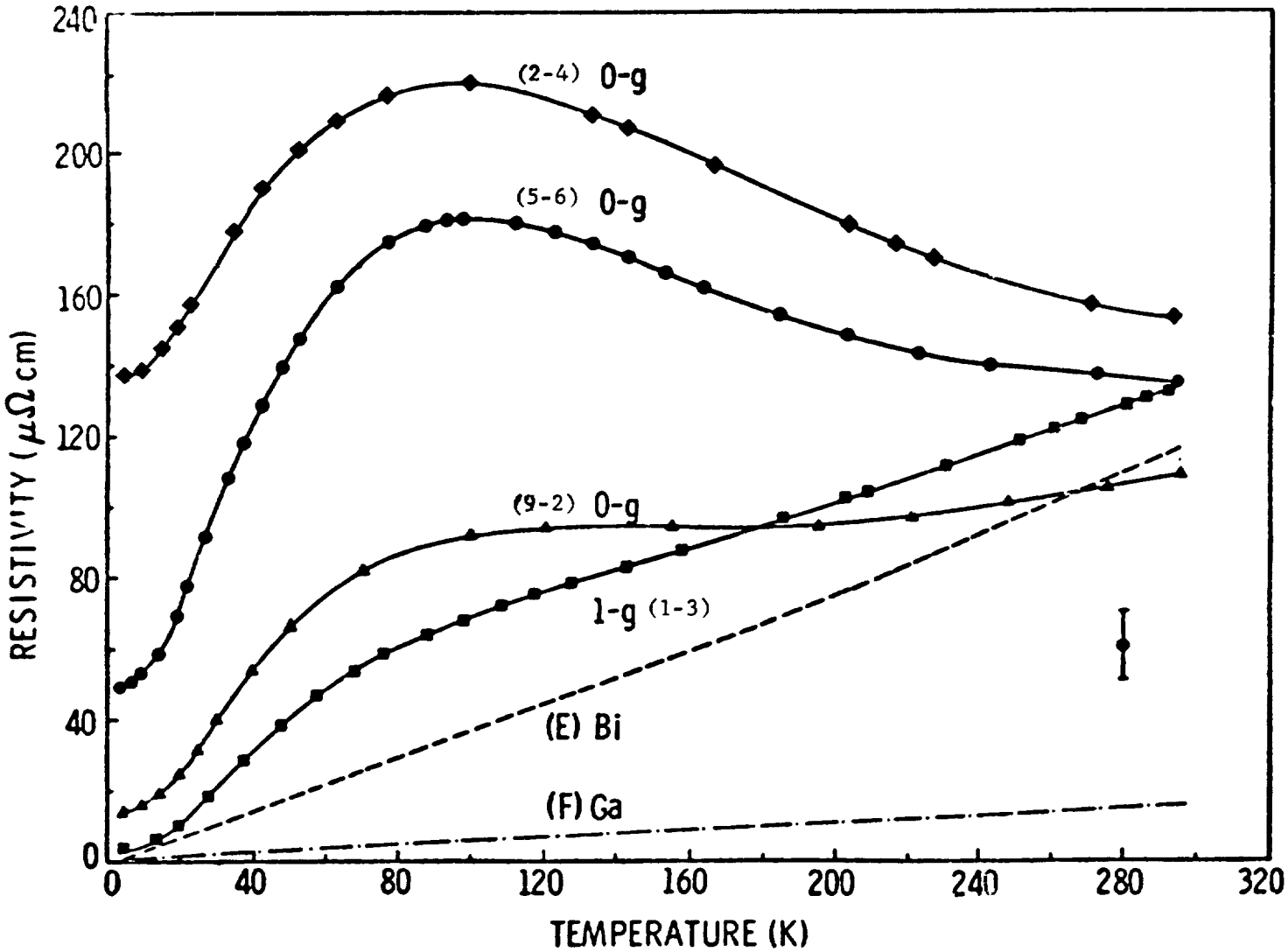


Figure 12a. The temperature dependence of the electrical resistivity of the zero-g and one-g solidified samples. Curves (E) and (F) are for the pure elements bismuth and gallium respectively.

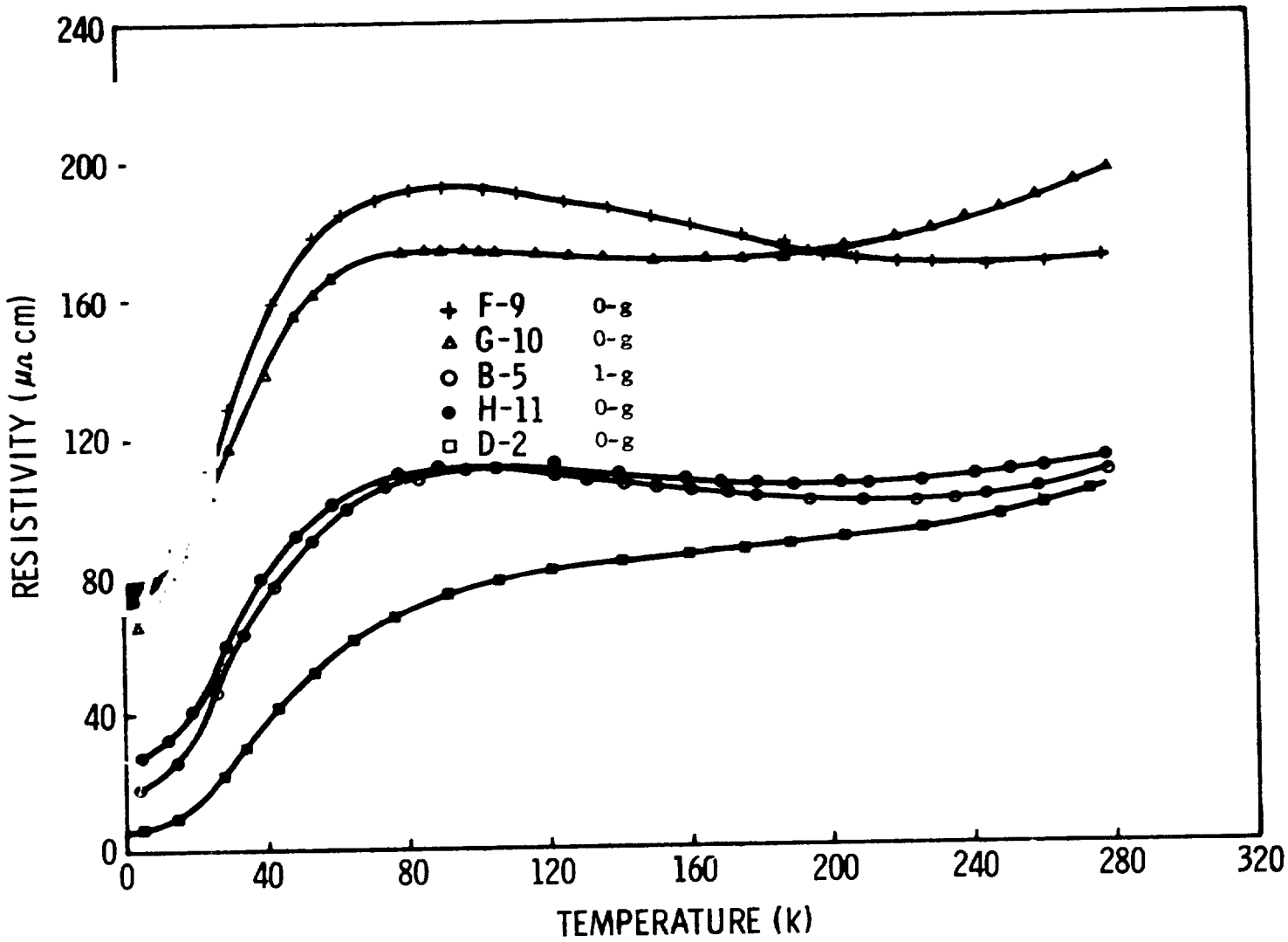


Figure 12b. The temperature dependence of the electrical resistivity for low-g and one-g solidified samples.

This unusual electric behavior of the drop tower solidified samples will be discussed in terms of the resistivity in three different temperature intervals: the low temperature (4.2 - 30 K), high temperature (100 - 300 K) and intermediate temperature (30 - 100 K) region.

a. Low Temperature Range (4.2 - 30 K)

For temperatures between 4.2 and about 30 K, all samples show typical metallic behavior. A selection of some resistivity curves in this region is given in Fig. 13. The resistivity may be expressed for low temperatures as the sum of a temperature-independent term, $\rho_o$, and a temperature-dependent term, $\rho_i(T) = CT^n$, as stated in Matthiessen's rule [16],

$$\rho = \rho_o + \rho_i(T). \tag{4}$$

The residual resistivity, $\rho_o$ at $T = 0$, can be associated with electron scattering from impurities, defects or interfaces and is, indeed, very high for sample (2-4), having the finest dispersion of all available alloys. We have plotted in Fig. 14 the residual resistivity, $\rho_o$, as a function of the average particle diameter $<d>$ and find that $\rho_o$ increases very rapidly as the particle size becomes smaller. The exact relationship between $\rho_o$ and $<d>$ is somewhat uncertain due to scattering in the data caused by the mean standard deviation, $\Delta d$.

If the residual resistivity is affected by the surface area of the scattering particles, we expect a relation in the form of

$$\rho_o = \rho_o^* + F/d^2. \tag{4a}$$

The term $\rho_o^*$ will represent the resistivity for very large particles ($d \to \infty$) and may be chosen between 0.005 and 0.13 $\mu\Omega$cm. For samples with particle sizes smaller than 10 $\mu$m, this term can be neglected because of

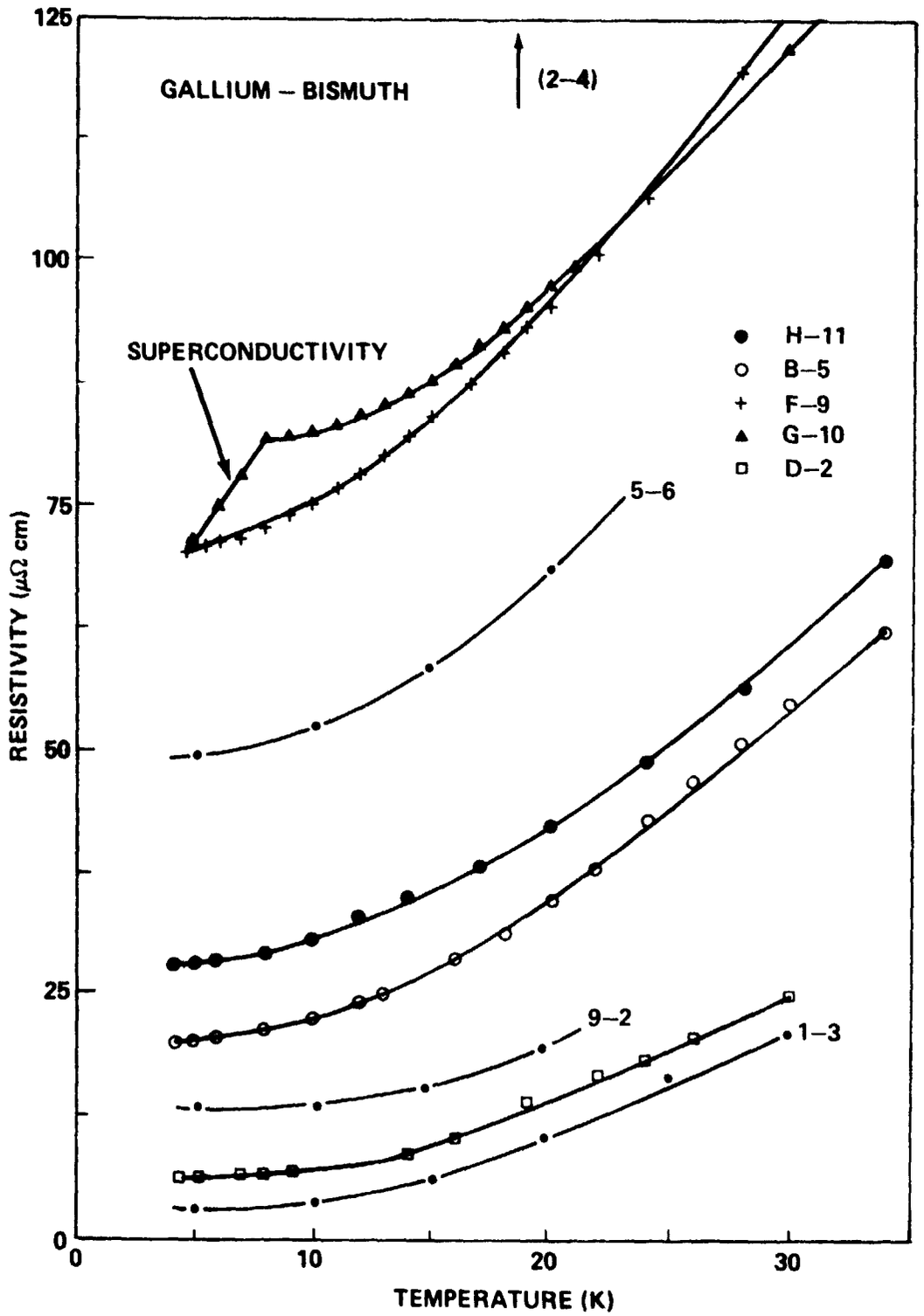


Figure 13. Low temperature resistivity of various Ga-Bi alloys.

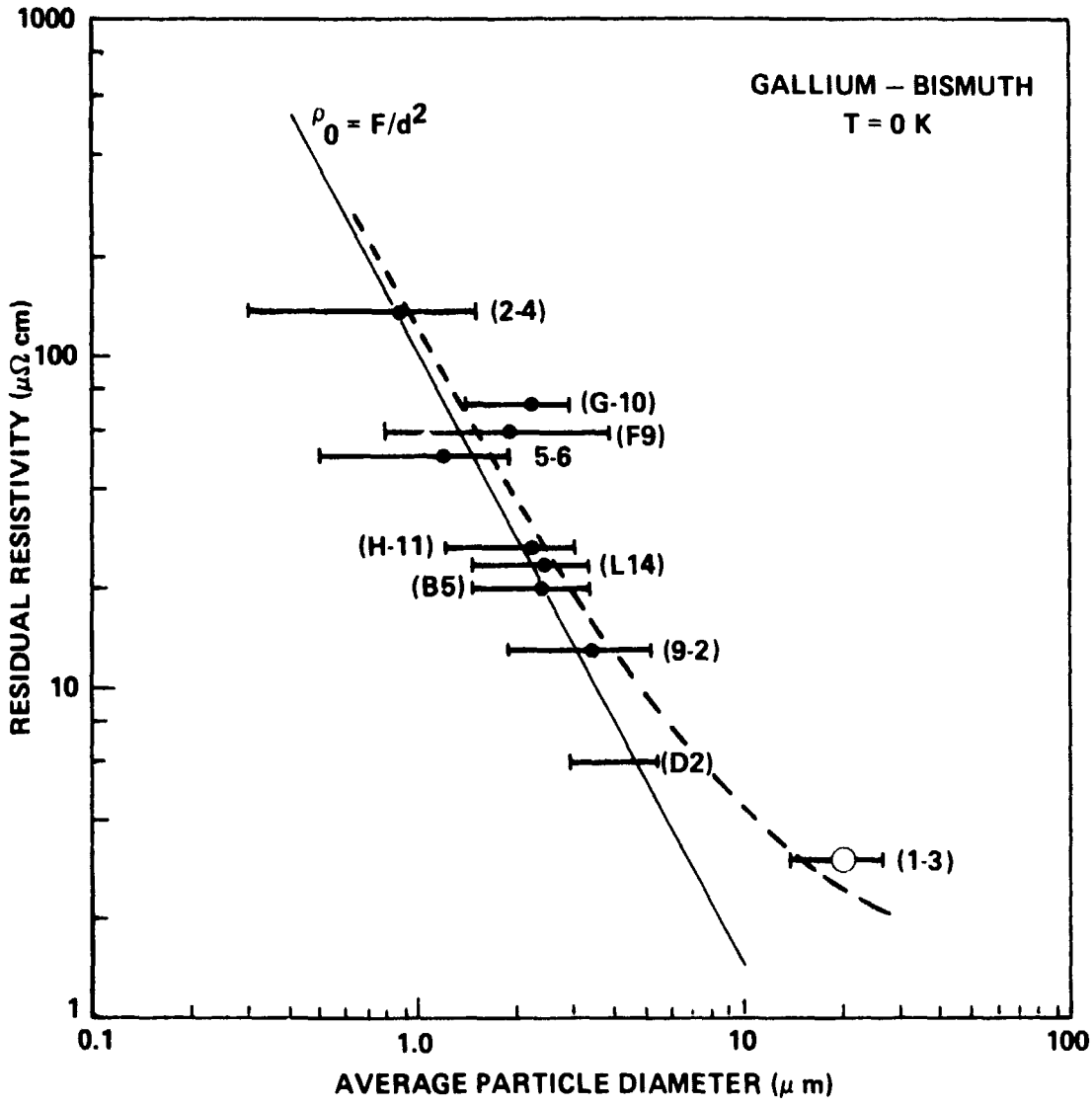


Figure 14. The dependence of the residual resistivity on the average particle diameter at T=0. The error bars indicate the range of particle distribution. The solid line gives an expected trend when considering the scattering contribution from the surface area.

the dominance of $F/d^2$. In Fig. 15, the reduced resistivity is plotted as a function of the reciprocal surface area and we find that the experimental data can be expressed in the form of Eq. 4a. Since the surface area is derived from the average particle diameters, a correlation of Fig. 14 and 15 exists so that the slope in Fig. 14 is twice the unity slope.

The temperature-dependent term, $\rho_i$, for all samples can be expressed according to Equation (4) with $n$ varying between 2 and 4.5. Figs. 16a and 16b contain the experimental data for the measured samples. In this log/log graphs, where the reduced resistivity $(\rho - \rho_o)$ is plotted against the absolute temperature, the exponent $n$ can be read as the slope of the straight part of the curve connecting corresponding data points. The value of $C$ is obtained for $T = 1$ K. Deviations from Matthiessen's rule are generally observed for $T > 20$ K. A summary of the characteristic values, $\rho_o$, $C$, and $n$ as obtained from the different samples are listed in Table 3 and are also compared with the corresponding literature data for the pure elements.

The following trends in the characteristic constants can be observed from the data of Table 3 for the immiscible alloys:

With increasing fineness of the dispersion, the values for $\rho_o$ and $C$ simultaneously increase, whereas the exponential value $n$ slowly decreases from its characteristic number of 4.5. For the finest dispersion obtained (sample 2-4), the exponent $n$ is already very close to the value measured for pure bismuth. Even finer dispersions should result in a further steep increase of $\rho_o$ in accordance with Fig. 14. However, little changes are expected for $C$ and $n$ which seem already to be saturated. Judged from the data obtained for $C$ and $n$, it is apparent that the

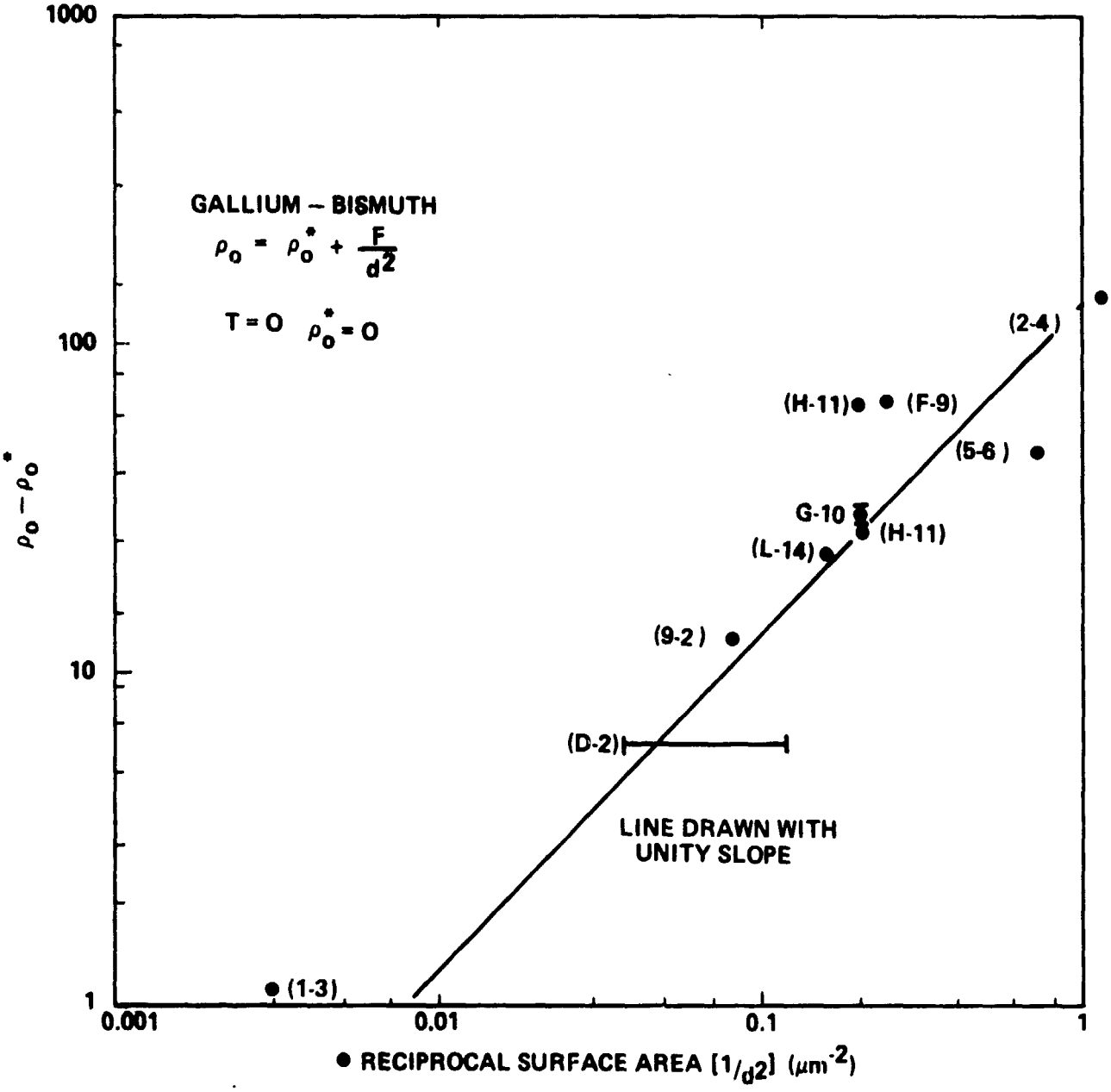


Figure 15. The effect of interface area on the residual resistivity of Ga-Bi alloys at T = 0. $\rho_o^*$ is the resistivity of the sample for very large particles ($d \to \infty$).

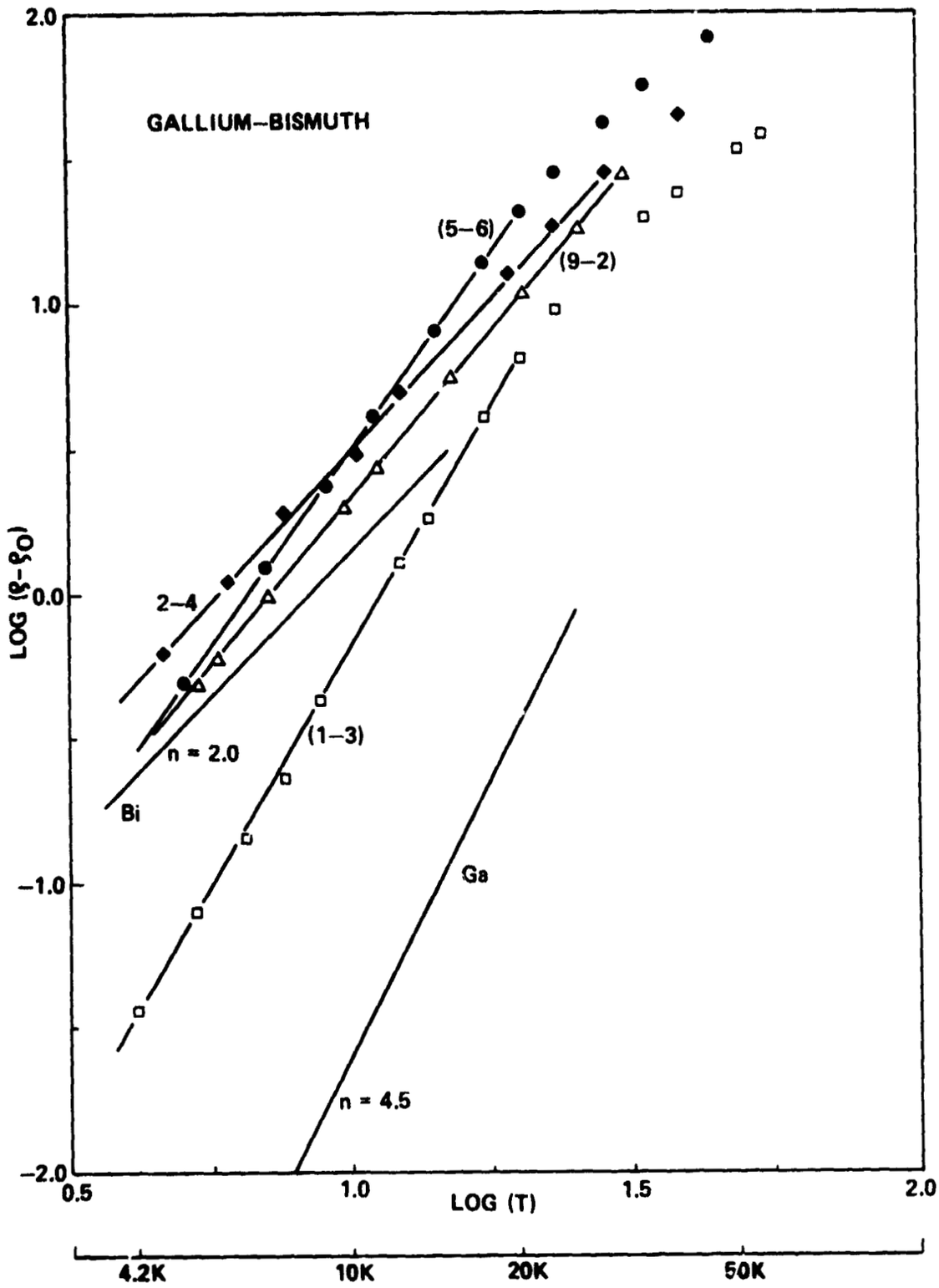


Figure 16a. Logarithmic plot of the reduced resistivity as a function of absolute temperature.

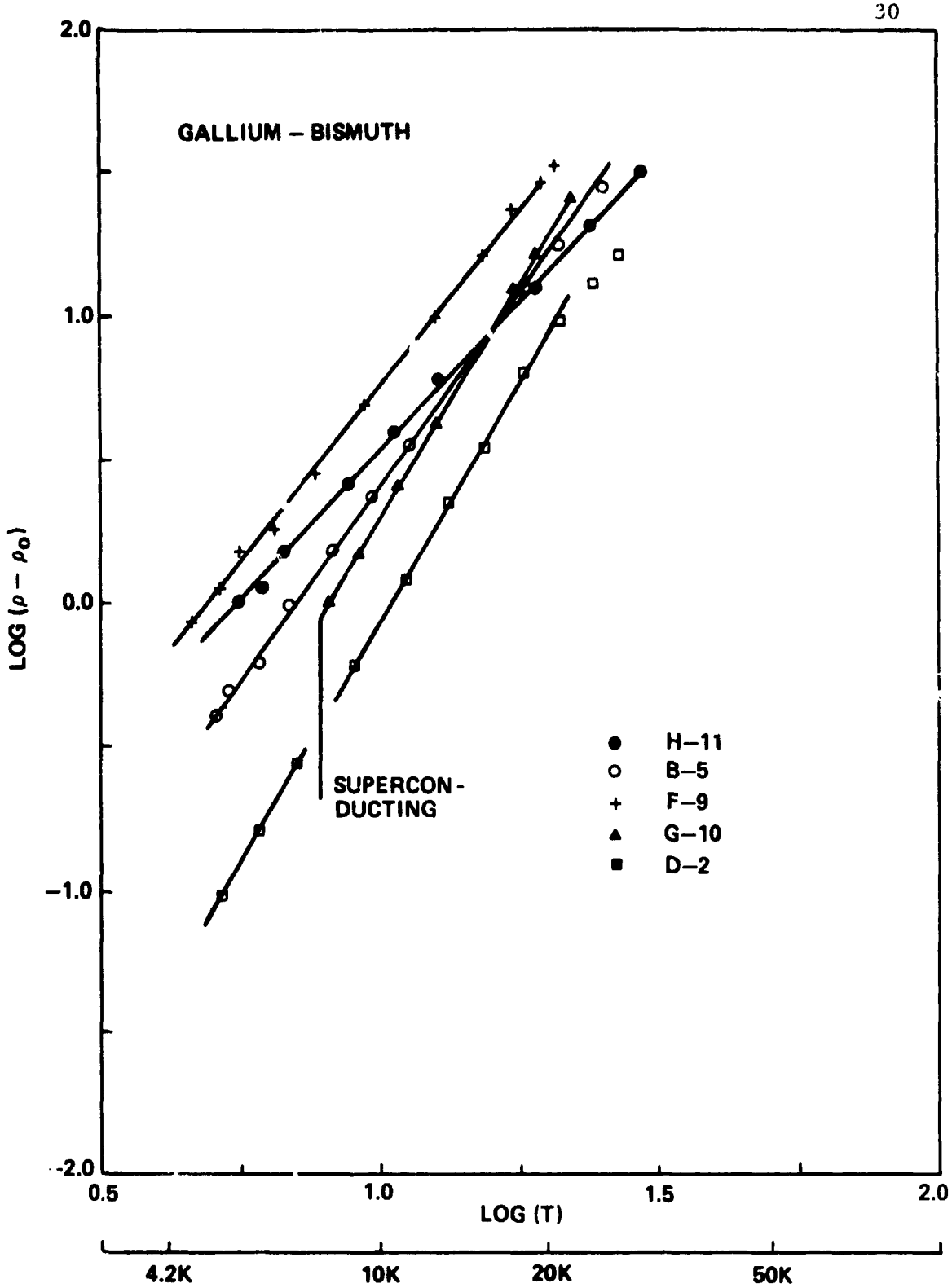


Figure 16b. Logarithmic plot of the reduced resistivity as a function of the absolute temperature.

TABLE 3

Low Temperature Data for Ga-Bi Alloys (50 at.%)

| Sample | $\rho_o$(μΩ cm) | C(μΩ cm $K^{-1}$) | n | Range (K) | Particle Diameter (μm) | Comments and References |
|---|---|---|---|---|---|---|
| Ga (polycryst.) | 0.005 | $0.7 \times 10^{-6}$ | 4.5 | 4.2-10 | bulk | [17] |
| 1-3 | 3.07 | 0.00023 | 3.45 | 4.2-20 | 20 ± 7 | ground control |
| D-2 | 6.26 | 0.0005 | 3.33 | 4.2-20 | 5.1 to 2.9 | elongated particles |
| 9-2 | 13.2 | 0.001 | 2.33 | 4.2-20 | 3-5 ± 1.7 | |
| B-5 | 19.80 | 0.006 | 2.61 | 4.2-20 | - | ground control |
| H-11 | 27.8 | 0.032 | 2.04 | 4.2-20 | 2.2 ± 0.9 | |
| J-12 | 39.9 | 0.002 | 3.15 | 5-25 | 1.6 to 7.9 | elongated particles |
| 5-6 | 48.6 | 0.010 | 2.52 | 4.2-20 | 1.2 ± 0.7 | |
| F-9 | 69.5 | 0.011 | 2.62 | - | 2.0 ± 1.2 | |
| G-10 | 80.65 | 0.0010 | 3.28 | 8-20 | 2.3 ± 0.7 | |
| 2-4 | 136.5 | 0.027 | 2.07 | 4.2-20 | 0.9 ± 0.7 | |
| Bi (polycryst.) | 0.13 | 0.01 | 2.0 | ~ 4.2 | bulk | [18] |

gallium loses its identity in the immiscible alloys when the dispersion comes into the submicron range. The different samples in Table 3 are ordered according to increasing $\rho_o$.

b. Intermediate Temperature Range (30 - 10 K)

Deviations from the $T^2$ behavior of the electrical resistivity for pure Bi are observed by several authors above 20 K [19]. This change in n is expected because at temperatures above the Debye-temperature, the resistivity of a metal is determined by the mean square amplitude of the lattice vibrations. This amplitude varies proportional with the absolute temperature, and, thus, the resistance should then change proportionally with the absolute temperature. We do not observe this expected behavior on Ga-Bi alloys with dispersions of less than 5 microns in diameter. An exception would be the ground-control sample (1-3). Instead, a peak in the resistivity is developing at about 100 K, which increases in magnitude with the degree of dispersion (see Fig. 12). The value of the resistivity at 100 K is plotted as a function of particle diameter in Fig. 17. It can be seen that the height of the peak is correlated with the particle diameter and that a strong effect is observed only for dispersions finer than 5 μm. However, when the particles become smaller, the absolute peak resistivity does not increase as fast as the residual resistivity does for the same amount of size reduction.

Similar resistivity peaks have been reported by Thompson [20] for bismuth samples containing Pb, Sn and Ge. However, these maxima are observed for solid solution type of alloys and are dependent on the concentration of the second constituent. Thomson explains the resistivity behavior in Bi-Pb alloys by the following mechanism: Since Pb has fewer

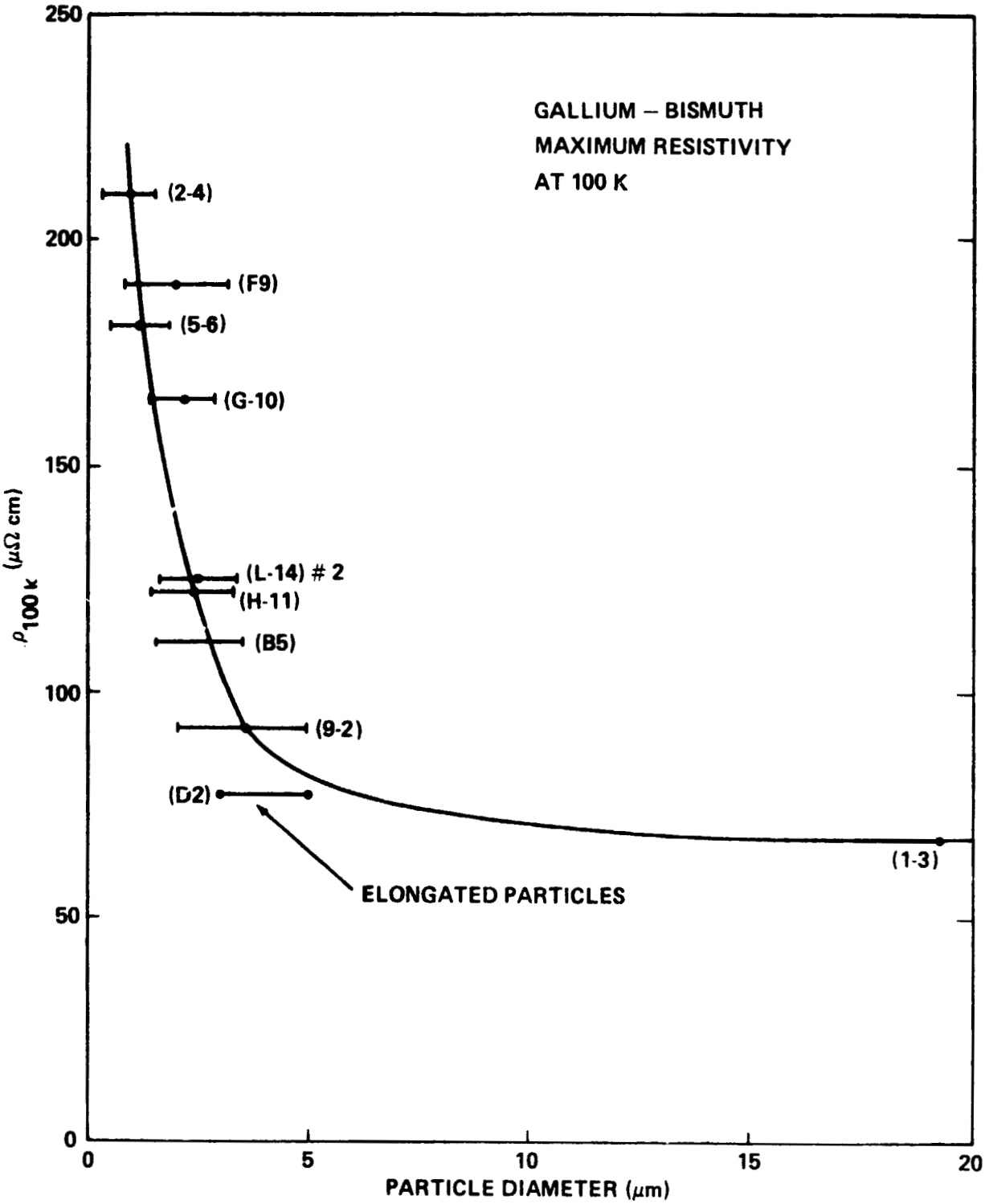


Figure 17. The absolute height of the resistivity peak as a function of the average Ga-particle diameter at T = 100 K. The error bars represent the mean deviation of the particle diameter.

valency electrons than Bi, the replacement of an atom of bismuth by lead in the crystal lattice reduces the number of free electrons in the upper Brillouin zone. If sufficient lead is dissolved, there will be no electrons in the upper Brillouin zone, but there will be some vacant levels (holes) in the lower zone. The resistance of such an alloy behaves normally at low temperatures, i.e., the resistance increases with the temperature since the mean-free path decreases. But when the temperature is such that the thermal energy is of the same order as the energy required to raise an electron to the upper zone, the resistance will decrease, since the decrease in the free path will be more than offset by the increase in the number of electrons excited and of the number of holes produced. When the number of holes is increased by the addition of more lead, the energy required to excite an electron is increased, and thus the excitation of the electrons only becomes apparent at a higher temperature, which is observed.

Our results are not expected to be influenced by a concentration variation of the second constituent. Since the solid solubility of Bi in Ga is less than 0.5 at.% [21], our alloys are always saturated with regard to this component. In addition, Thompson [20] finds that 0.5 at.% Ga in Bi only slightly changes the resistance curve for Bi and does not lead to a resistivity peak, like in Bi-Pb. His results on Ga-Bi are comparable with those obtained on our ground-control sample (1-3). The resistivity peak for our alloys, which all have the same composition of 50 at.%, is caused by the gallium phase being finely dispersed.

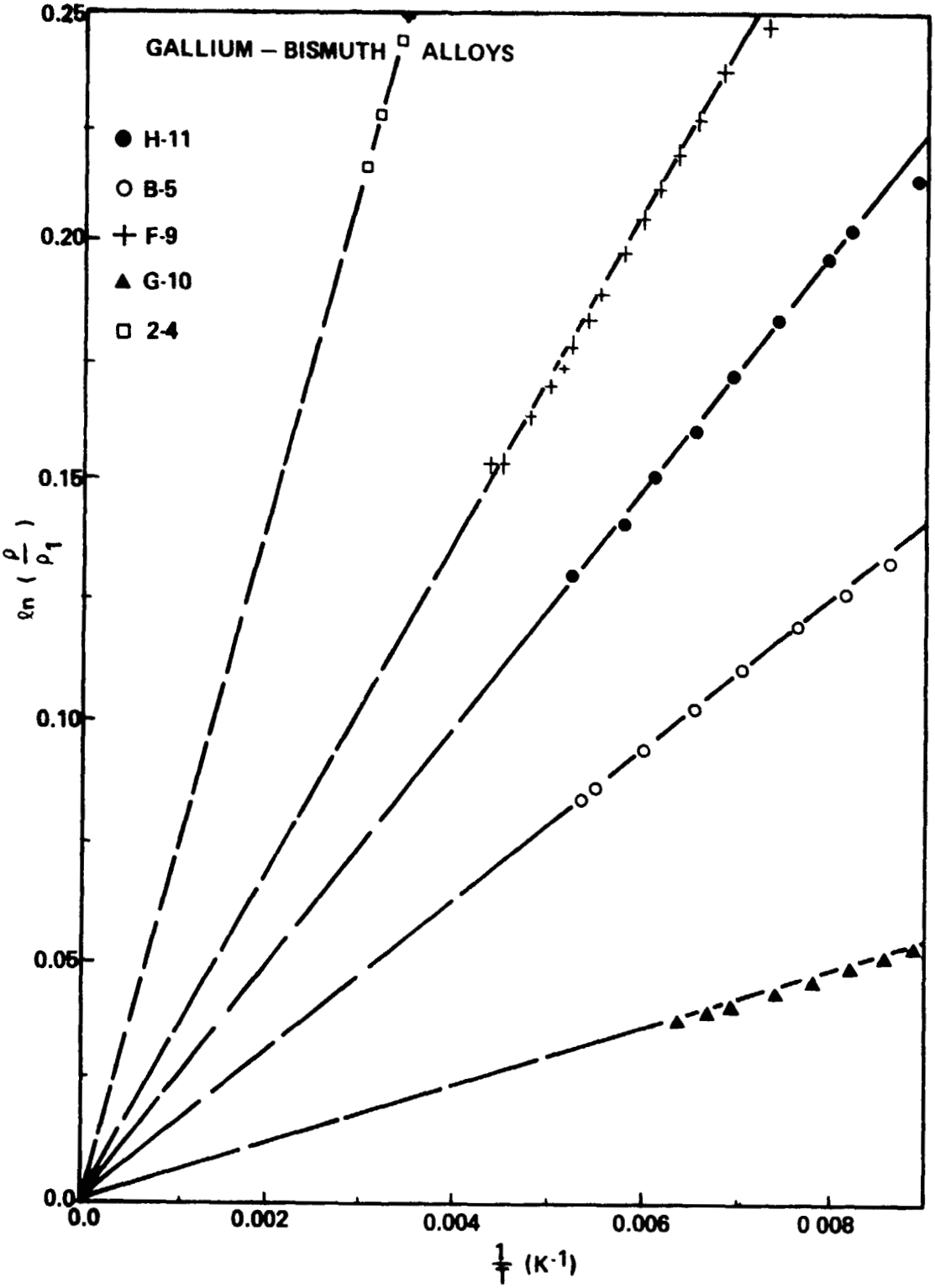


Figure 18. The energy gap, as derived from resistivities, for various Ga-Bi alloys. $\rho_1$ is a sample-dependent constant.

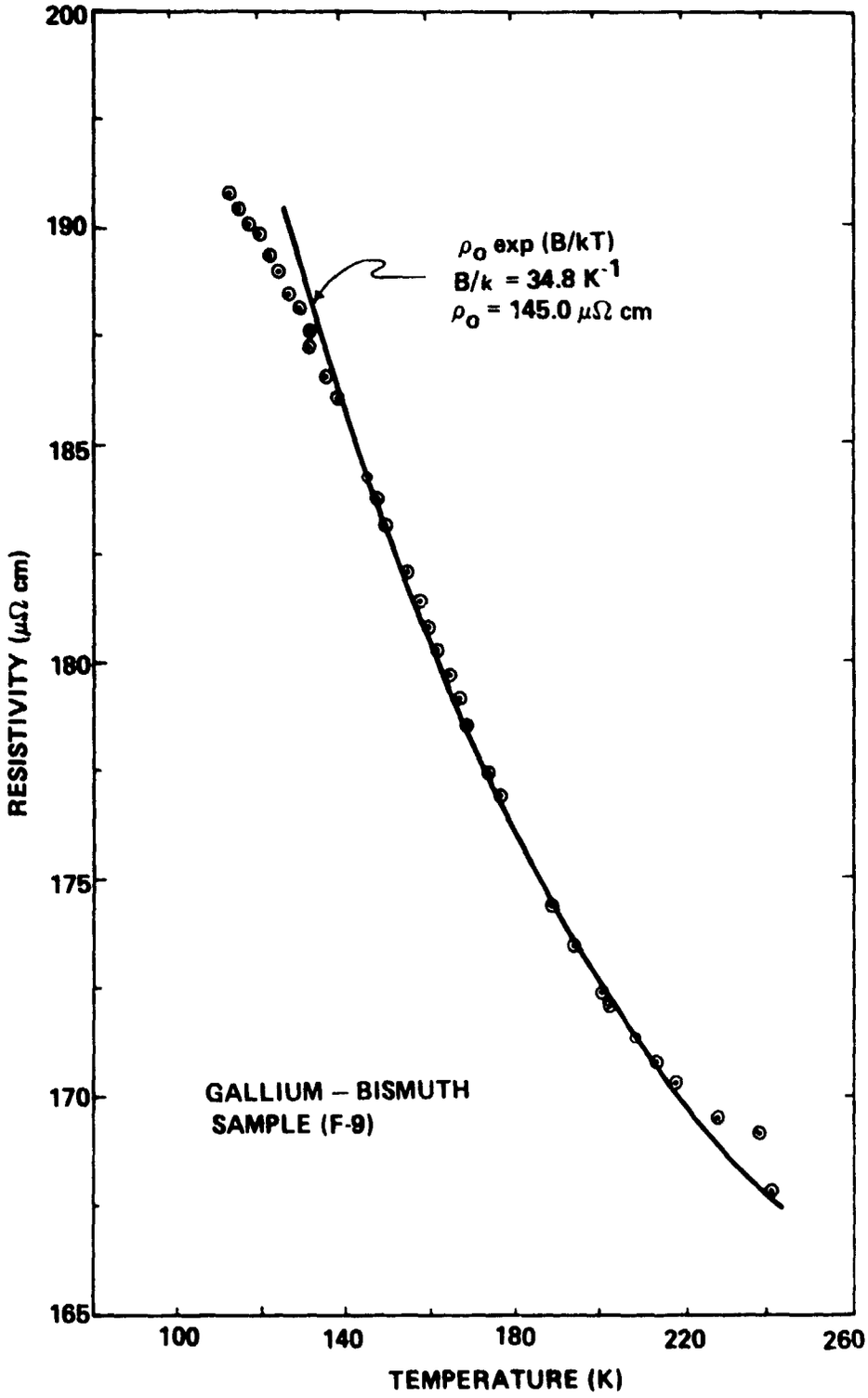


Figure 19. Exponential fit of the resistivity in the semiconducting region for sample (F-9).

### c. High Temperature Range (100 - 280 K)

The slopes ($d\rho/dT$) of the resistivity curves for Bi, Ga and sample (1-3) in Fig. 12 are all positive, which is typical of an electronic conductor. The coarse dispersion of the ground-control sample (1-3) has resulted in a material with essentially the same electrical characteristics as for pure Bi. However, when the dimensions of the dispersed Ga particles become small ($d \lesssim 5$ m), the electrical characteristics of the Bi matrix is changed (i.e., $d\rho/dT \sim 0$). For even smaller dispersions ($d < 2$ μm), as seen in the zero-gravity samples, the conductivity of the matrix has completely changed so that $d\rho/dT \sim 0$ and a broad maximum occurs at about 100 K. The high temperature resistivity ($T < 120$ K) of the finely dispersed samples behaves similar to an intrinsic semiconductor.

Indeed, the resistance can be analytically described with an exponential relationship. In the temperature interval between 120 and 300 K, the resistivity changes as

$$\rho = \rho_1 \exp(B/kT) \qquad (5)$$

where $\rho_1$ is a characteristic resistivity and $B$ is an energy gap for the conduction process. This relationship is applicable to samples with particles below an average diameter of 3 μm. A graphic representation of Eq. (5) for several samples is given in Fig. 18 and the resulting constants are listed in Table 4. The quality of the data and the temperature-range of the agreement between the experimental resistivity and the exponential relationship are demonstrated in Fig. 19 for sample F-9.

TABLE 4

Constants for the Semiconducting Range of Ga-Bi Alloys

| Sample | Diam. (μm) | d-Δd (μm) | $\rho_1$ (μΩcm) | B/k ($K^{-1}$) | B ($10^{-3}$ eV) |
|---|---|---|---|---|---|
| G-10 | 2.3 | 1.6 | 164.7 | 6.1 | 0.53 |
| B-5 | - | - | 97.5 | 16.0 | 1.38 |
| H-11 | 2.2 | 1.3 | 88.8 | 25.2 | 2.2 |
| F-9 | 2.0 | 0.8 | 144.9 | 34.8 | 3.1 |
| 2-4 | 0.9 | 0.2 | 85.0 | 72.5 | 6.25 |

It can be seen from Fig. 19 that the experimental data follow an exponential relation over a temperature interval of about 100 K. Deviations occur for high temperatures (> 240 K) as well as low temperatures (< 140 K). A small energy gap, which increases in magnitude with decreasing particle size, develops in the Ga-Bi alloys for dispersions below 5 μm. As can be seen from the data of the third column of Table 4, the particles with minimum diameter (d - Δd) contribute most to the energy gap. The semiconducting behavior does not extend to very low temperatures (< 100 K) where normal conducting behavior exists, as has already been discussed.

### d. Room Temperature Resistivity

Neglecting interface scattering effects at room temperature, we expect a composite resistivity between 80.6 and 38.8 μΩcm if all the Ga particles are either electrically connected in series or in parallel. The room temperature resistivity should then also be independent of particle size. We find that all room temperature resistivities are higher and lie between 110 and 180 μΩcm. We know, however, that the mean free path for Bi

at room temperature is exceptionally high with about 7 μm [22]. Therefore, we can expect a scattering contribution from particles in the micron range. This fact is also revealed in the residual resistivity.

The laboratory experiments further indicate a jump in the sample resistance by 300 or 400 % at 30 °C, when the gallium melts. These changes in resistivity are not very reproducible, but they are far beyond the expected increase of about 15 % by melting of the gallium phase. There is a possibility that the large resistivity jumps may be caused by a phase transformation of Bi at room temperature. Brigman [23] has measured a resistivity decrease of 600 % for Bi when the phase transformation at 25 kbar is achieved (Bi I → Bi II).

Gallium expands on solidification by 3%. Can sufficient pressure be generated by the freezing of Ga particles to justify a phase transformation in solid Bi at an interface region?

Assuming infinite stiffness of Bi, the pressure generated by freezing of gallium would be about 15 kbar. This pressure alone is not sufficient to generate the transformation at 26 kbar. Some additional pressure should be generated by the unequal expansion coefficients which are $40 \times 10^{-6}$ $deg^{-1}$ and $15.6 \times 10^{-6}$ $deg^{-1}$ for Bi and Ga respectively, at room temperature [24]. Although the internal pressures generated by freezing of Ga are too small, a phase transformation of Bi in an interfacial region cannot be ruled out.

In summary, our results show that the electrical properties of the Bi alloys are drastically changed in each temperature range by dispersion and zero-gravity processing. The finer the dispersion, the greater the change in the properties of the composite. An extrapolation of the resistivity

data for a hypothetical Ga-Bi alloy with gallium partices of of 0.1 μm diameter will be given in Section 6.

## 4. Superconductivity Measurements

In many instances the superconducting properties of a material can be used as a supplemental means to analyze its conditions of state. Although Bi in its bulk form is not superconducting [25] above a temperature of 0.5 K, gallium should show a transition to the superconducting state at 1.08 K [26].

Transition temperature measurements have been made on these samples by both the resistance and inductance technique. Whereas, with the resistance measurement, the formation of the first superconducting path of electrons across the sample is observed, the inductive technique reveals the amount of flux excluded from the material as it becomes superconducting.

### a. Inductance Measurements

Typical results of inductance measurements, where the sample is located inside a coil with the inductance L, are shown in Fig. 20. There, the relative change in inductance $\Delta L/L$, based on the inductance measured at 6.0 K, is plotted against temperature. A distinct change in inductance (which is caused by the superconducting transition) is observed on all samples at 7.9 K. This signal change is quite small, and using a calibration sample of known superconducting volume, the volume fraction of the superconducting phase in the Ga-Bi samples can be calculated. Some samples were cooled to 4.2 K so that the superconducting transition of the tantalum capsule ($T_c$ = 4.39 K) could be measured and used also as a calibration volume. The results of the measured transition temperature and the superconducting volume are given in Table 5.

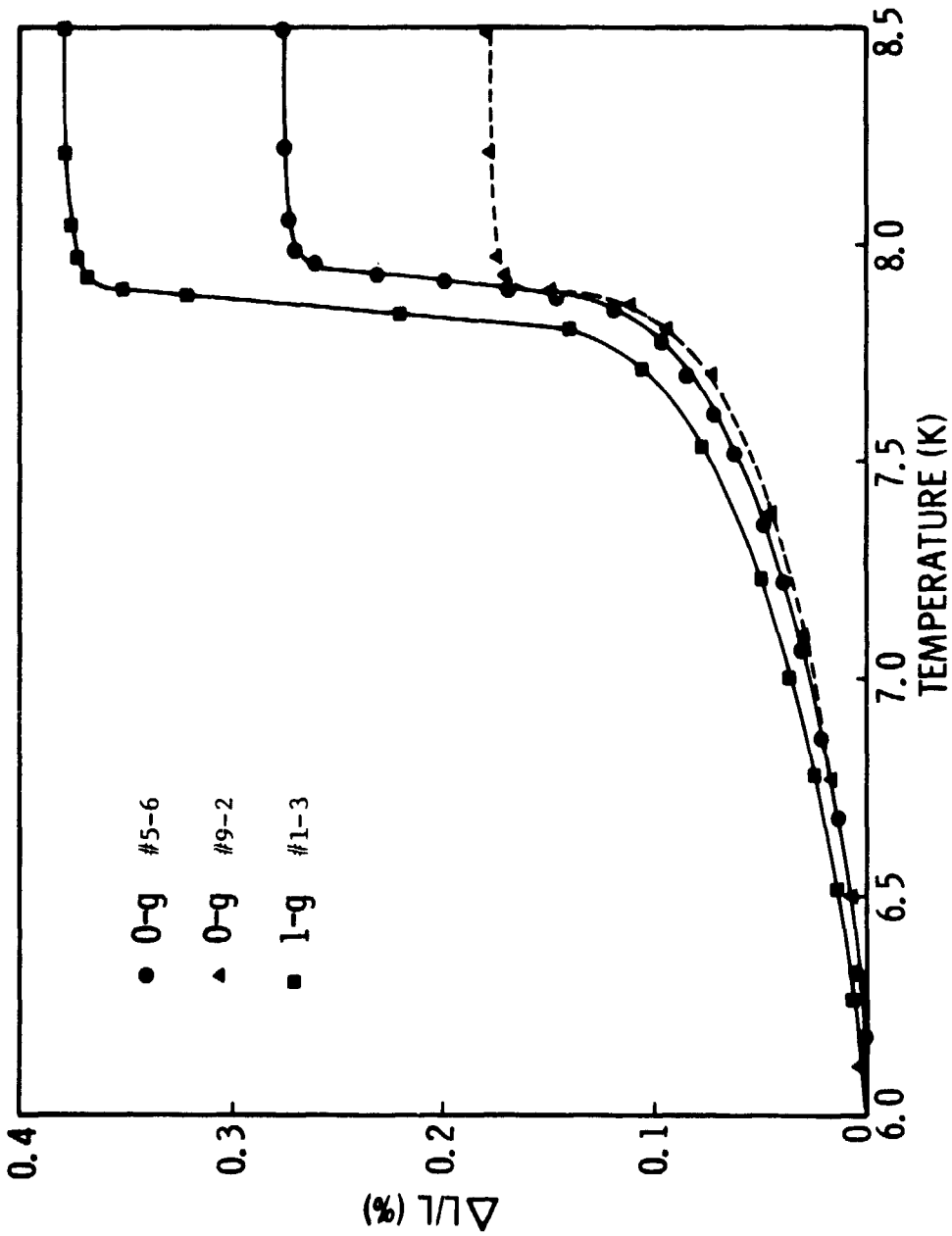


Figure 20. Inductively measured transition curves for various Ga-Bi alloys.

TABLE 5

Transition Temperatures and Superconducting Volumes of Low-Gravity Processed and Ground-Control Ga-Bi Alloys

| Sample | 0-g Duration (sec)* | Onset of $T_c$ (K) | Supercond. Vol. (%) (7.9 to 6.0K) | $\Delta L/L$ (%) for Ta** |
|---|---|---|---|---|
| 5-6 | -- | 7.99 | 1.7 | -- |
| 9-2 | -- | 7.96 | 1.6 | -- |
| 1-3 | 0 | 7.95 | 3.0 | -- |
| G-10 | 3.6 | 7.90 | 1.89 | 6.7 |
| H-11 | 3.9 | 7.90 | 0.87 | 7.0 |
| J-12 | 0 | 7.90 | 1.24 | 7.3 |
| K-13 | 2.9 | 7.91 | 1.31 | 7.0 |
| L-14 | 4.2 | 7.91 | 0.94 | 7.7 |
| B-5 | 0 | 7.93 | 0.74 | 6.8 |
| C-6 | 3.2 | 7.92 | 1.95 | 7.0 |
| D-2 | 2.8 | 7.91 | 1.41 | 6.6 |
| E-4 | 2.8 | 7.89 | 1.27 | 6.1 |
| F-9 | 3.0 | 7.92 | 0.57 | 7.0 |

* Duration of cooling from ~300 °C to ~20 °C.

** Change of inductance caused by the Ta-housing becoming superconducting.

It can be seen that all samples exhibit a rather sharp superconducting transition between 7.9 and 8.0 K. However, only 0.5 to 3 volume percent of the material show this behavior. The superconducting phase is formed in the ground control as well as in the zero-gravity processed samples with the same transition temperature. Annealing of the alloys up to 100 °C for 40 minutes leaves the amount of superconducting phase nearly unchanged.

b. Resistivity Measurements

Although part of the samples becomes superconducting, the resistivity does not drop to zero at temperatures below 7.9 K as may be seen from Fig. 13. In fact, the resistance at this particular temperature around 8 K was constant to within 0.5 %, and no sudden drop could be observed within the relative accuracy of the resistance measurements. This indicates that the superconducting phase consists of isolated regions which are not interconnected. An exception is observed only on sample G-10 which shows the beginning of a resistive transition starting at 8.0 K. The results of the resistivity measurements on this sample from two heating and cooling cycles are given in Fig. 21. The data are plotted on an expanded scale to show more clearly the superconducting transition, which is very broad and not completed at 4.2 K. In its microstructure, this sample is not any different from the others, and it is unclear why a resistive transition is observed for this sample only.

The fact that portions of the samples become superconducting at 8 K cannot be attributed to processing in zero-g, since the ground control sample shows the same transition. This behavior may be attributed to a change in state of some of the gallium or bismuth. Both materials are

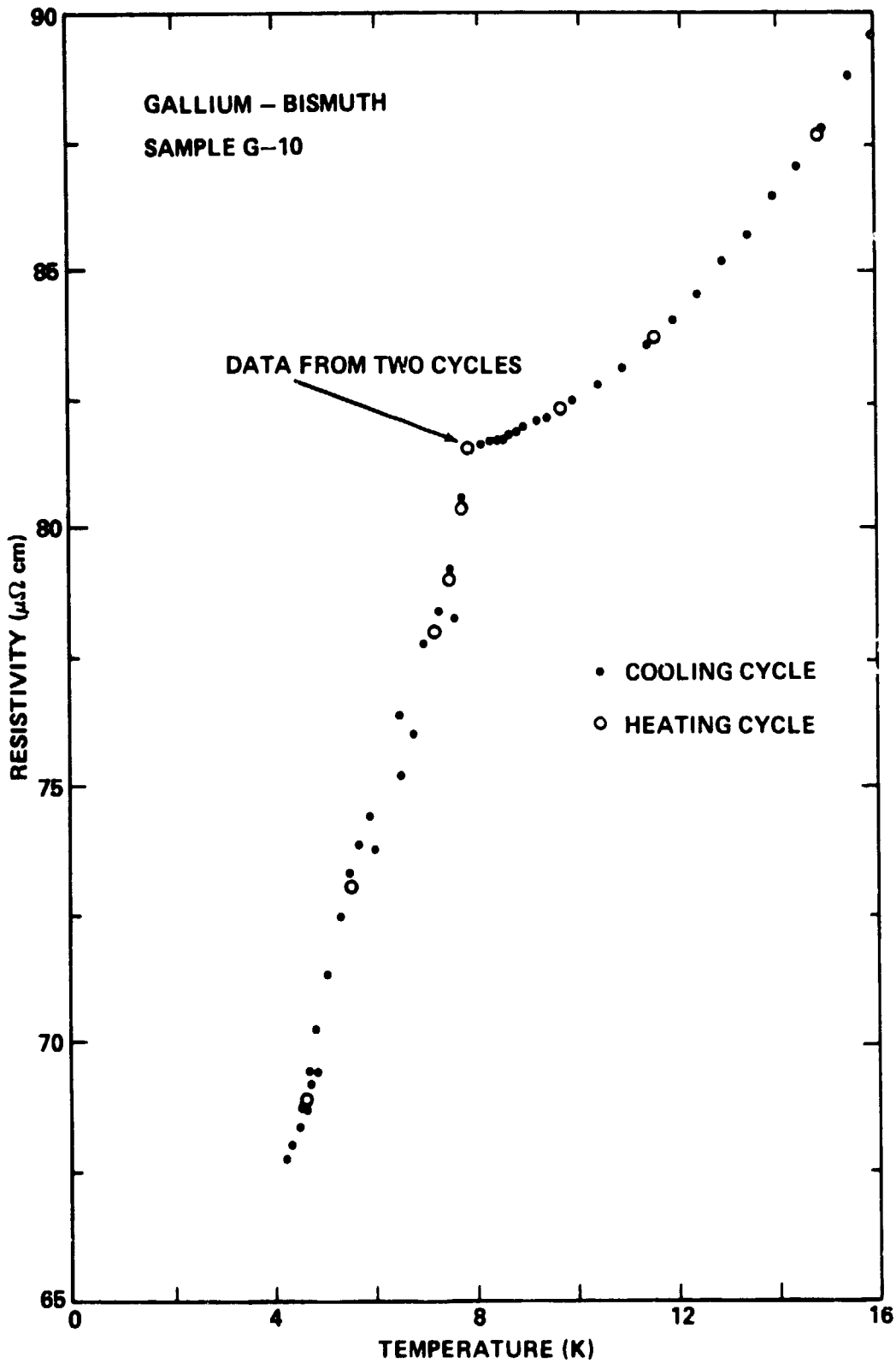


Figure 21. Superconducting transition of sample G-10, measured with the resistive technique.

known to produce phase changes when put under sufficiently high pressure [27] or when fabricated in thin films [28, 29]. The transition temperature can be as high as 8.55 K for Bi under a pressure of 90 kbar or 8.4 K, respectively, for thin film gallium. There is a possibility that either of these phases may be present in the samples. However, we can state that the high temperature superconductivity is associated with the fact that the gallium exists as dispersed particles in the alloy. In their nondispersed state, samples do not show a transition above 4.2 K. The occurrence of a superconducting phase with a transition temperature of 7.9 K has not been reported in the literature and such a phase cannot be predicted on the basis of the Ga-Bi phase diagram.

### 5. Hall Effect Measurements

The resistivity measurements have resulted in nonlinear resistivity versus temperature curves, and several samples exhibit a broad maximum in the resistivity. Since the samples behave like semiconductors over an intermediate temperature range, Hall effect measurements were initiated to gain more information about the unusual conduction behavior. Such measurements permit determination of the charge of the current carriers, their mobility and their concentration [16].

When a conductor (thin plane slab) is placed in a magnetic field perpendicular to the direction of current flow, a voltage is developed across the specimen in the direction perpendicular to both the current and the magnetic field. This voltage is called the Hall voltage. The sign of

the Hall voltage indicates the kind of charge carriers: negative for free electron carriers and positive for hole carriers. The following relations will apply:

$$E_H = JB/ne \qquad E_H/E_L = \mu B \qquad J = ne\mu E_L \qquad (6)$$

where $J$ is the current density, $B$ is the magnetic flux density, $e$ is the charge of the carrier, $\mu$, their mobility, $n$, the concentration of charge carriers per unit volume, $E_H$ and $E_L$ are the Hall and sample potential. These equations can be used to calculate the mobility and the concentration of charge carriers from the known quantities.

Observed values of the Hall constant for several common metals are listed in Table 6. The anomalous large value for Bi in comparison with Na, Cu, and Ag is interpreted by the band theory and caused by a low concentration of electrons outside the nearly filled bands. Actually, there is one free electron for every thousand Bi atoms [16].

TABLE 6

Observed Hall Constants for Common Materials at Room Temperature [16]

| Metal | $R_H \times 10^{11}$ (V-cm/A-G) |
|---|---|
| Na | -25.0 |
| K | -42 |
| Cu | - 5.5 |
| Ag | - 8.4 |
| Al | - 4.0 |
| Zn | + 3.3 |
| Cs | -78 |
| Bi | -1500 |
| F-9 | - 700 |
| G-10 | - 240 |
| D-2 | - 210 |

Reversal of the Hall constant from negative to positive values, indicating a transition from negative to positive charge carriers, has been observed for several alloy systems, as the Cu-Sn and Bi-Sn system [30]. It is further possible for the Hall coefficient to change the sign as a function of temperature as has been found on bismuth doped with 0.1 at.% Sn [30].

Assuming the possibility of doping bismuth with gallium, the gallium would act in the alloy as an acceptor of charges, and absorb some or all of the few free electrons from Bi. Therefore, we may expect an increase in the ohmic resistance and decrease or eventual reversal of the Hall constant for finely dispersed Ga-Bi alloys.

Measurements of the Hall effect on Ga-Bi alloys have been made in small magnetic fields up to 2,000 G. The results [31] obtained on four different samples including pure Bi are listed in Table 7. Compared with Bi, we observe an increase in the Hall constant upon the dispersion of gallium, indicating an increase in the number of charge carriers. The additional negative charge carriers are introduced by the gallium particles. These results also show a correlation of Hall constant with the particle size, with the finer dispersions having the smallest increase in the number of charge carriers. A reversal of the Hall constant has so far not been observed and could occur for dispersions with particle sizes below 1 μm, when the contribution of bulk gallium becomes less important.

The temperature dependence of the Hall constant can be interpreted from the measurements at room temperature and liquid nitrogen. For sample F-9 and G-10 decrease of the Hall constant (to more negative values)

TABLE 7

Hall Data for Ga-Bi Alloys

| Sample | T(K) | Hall Constant, $R_H$ ($cm^3/C$) | Carrier Density, n $10^{19}(1/cm^3)$ | Mobility, $\mu$ $10^3(cm^2/Vs)$ | B(Gauss) |
|---|---|---|---|---|---|
| G-10 | 300 | -0.238 | 2.62 | 1.20 | 2100 |
| G-10 | 78 | -0.326 | 1.92 | 1.87 | 2100 |
| D-2 | 300 | -0.212 | 2.95 | 2.01 | 2100 |
| D-2 | 78 | -0.118 | 5.30 | 1.68 | 2100 |
| F-9 | 300 | -0.700 | 0.89 | 4.09 | 1100 |
| F-9 | 78 | -1.14 | 0.55 | 5.93 | 1100 |
| Bi(poly.) | 300 | -1.53 | 0.41 | 13.41 | 2100 |
| Bi(poly.) | 300 | -0.810 | 0.82 | 7.10 | 1100 |
| Bi(poly.) | 78 | -3.47 | 0.18 | 115 | 1100 |
| Ga(poly.) | 298 | $-5.0 \times 10^{-4}$ | 12.50 | 0.033 | any |

Conversions for $R_H$:

$1\ cm^3/As = 1\ cm^3/C = 1 \times 10^{-6} m^3/C$

$1\ m^3/C = 1 \times 10^{-2}\ V\ cm/A\ G = 1 \times 10^{-2}\ \Omega\ cm/G$

$1\ V\ s/m^2 = 1\ Wb/m^2 = 10^4$ Gauss (G)

From CGS to $m^3/C$ multiply by $9 \times 10^{13}$

is observed with decreasing temperature. This change is most pronounced for sample F-9 and less for G-10. This behavior is caused by a reduction of the number of carrier electrons and the small band gap that develops with decreasing temperature. Indeed, sample F-9 exhibits a resistivity peak, whereas the maximum is considerably lower for G-10 (see Fig. 12b). Sample D-2 shows no resistivity peak and, accordingly, the Hall constant increases with decreasing temperature. The correlation of the resistivity maxima with the behavior of the Hall constant indicates that the resistivity peaks are caused by a reduction in the concentration of free electrons.

## 6. Summary and Outlook

We have demonstrated the influence of density segregation on the microstructure of Ga-Bi alloys when cooled through the miscibility gap. Bulk homogeneous dispersions of gallium particles in a bismuth matrix could be obtained by low-gravity solidification of the alloys in a drop tower. The particle sizes for different samples ranged between one and twenty microns. A quantitative correlation of particle size and cool rate, which can be expected from nucleation and growth theory, could not be shown. However, the electrical properties of the different alloys could be correlated with the microstructure.

The results clearly show that the resistivity of the finely dispersed low-g samples is quite different from the behavior of the pure constituents and strongly depends on the degree of the gallium dispersion. This is especially true for alloys with Ga particles of 5 μm diameter and less where the basic properties of bismuth are modified and the samples exhibit the unusual combination of semiconducting, and normal-conducting behavior.

As the size of the gallium particles is reduced in the Bi matrix, a maximum develops in the resistivity of the alloys at about 100 K caused by a reduction in the number of free electrons. Simultaneously, the residual resistivity steeply increases proportionally with the amount of interface area generated.

At this point, it would be interesting to extrapolate the resistivity data for a hypothetical alloy with a finer dispersion than was actually obtained. We will now estimate the properties a sample should have with a particle size of 0.1 μm, by extrapolating the experimental results obtained for particle diameters $\geq$ 0.9 μm. Figure 22a gives on a logarithmic scale the residual resistivity at T = 0 and the absolute peak height at 100 K for different particle diameters. These data can be extrapolated to the desired dispersion size. It can be seen that the slope of the resulting two curves for $\rho_o$ and $\rho$(100K) is different so that they intercept at a size of about 0.5 μm. This crossover indicates that the peak in resistivity will disappear for alloys with particles of less than 0.5 μm diameter. A monotonically decreasing resistivity with increasing temperature should result for such samples. A further distinctive property of the alloys is the magnitude of the energy gap. This can be determined from the experimentally obtained data for different samples which are also plotted in Fig. 22a. Since we have noticed earlier that the value for the energy gap is related to particles with the smaller diameter, the range between the smaller particles, d-Δd, and the average diameter is indicated. The value of the energy gap does not change very much for the finer dispersions and a value of $10^{-2}$ eV seems reasonable for the desired alloy.

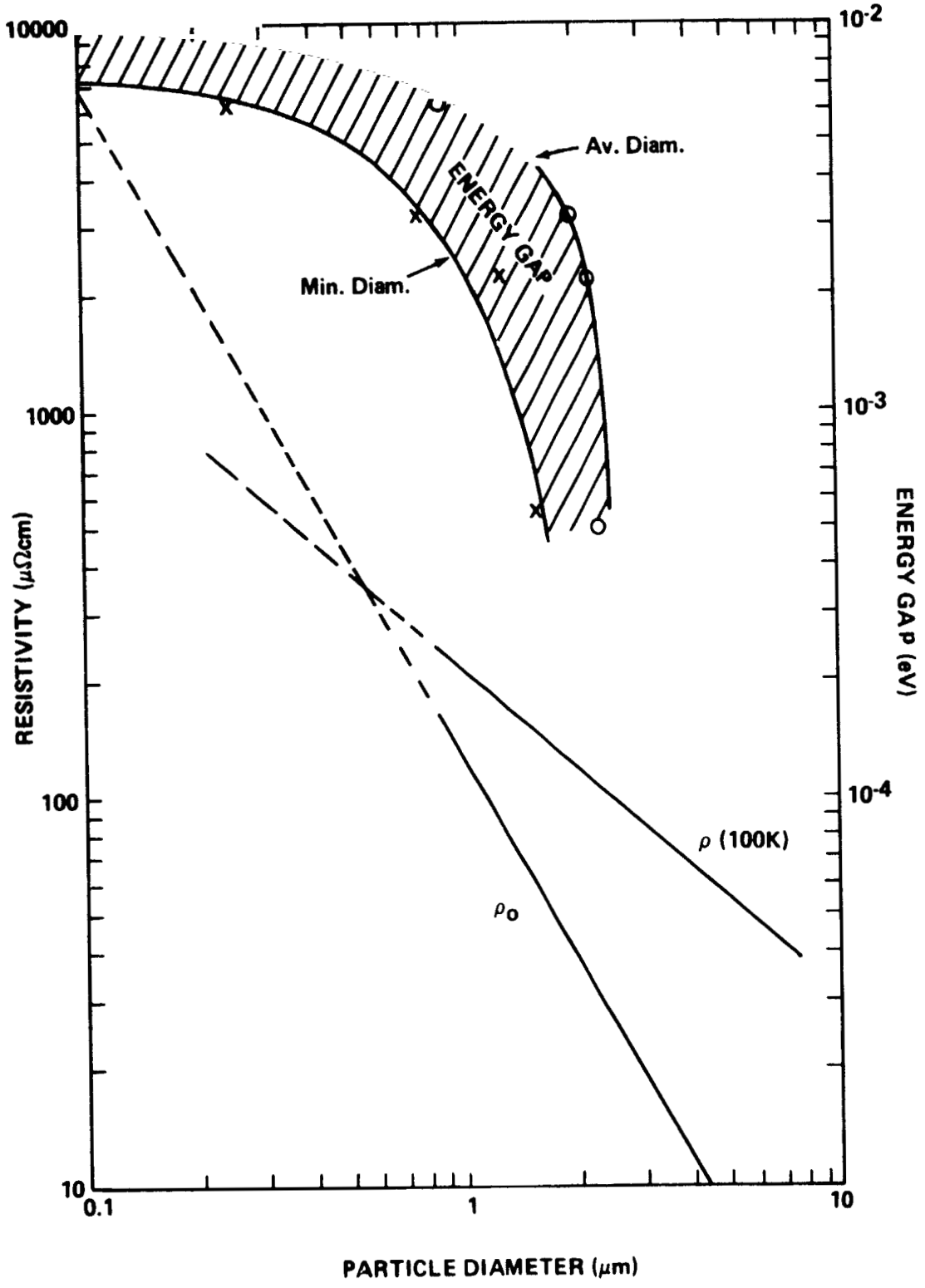


Figure 22a. Extrapolation of the experimental data to a particle diameter of 0.1 μm for residual resistivity, peak resistivity at 100 K, and energy gap.

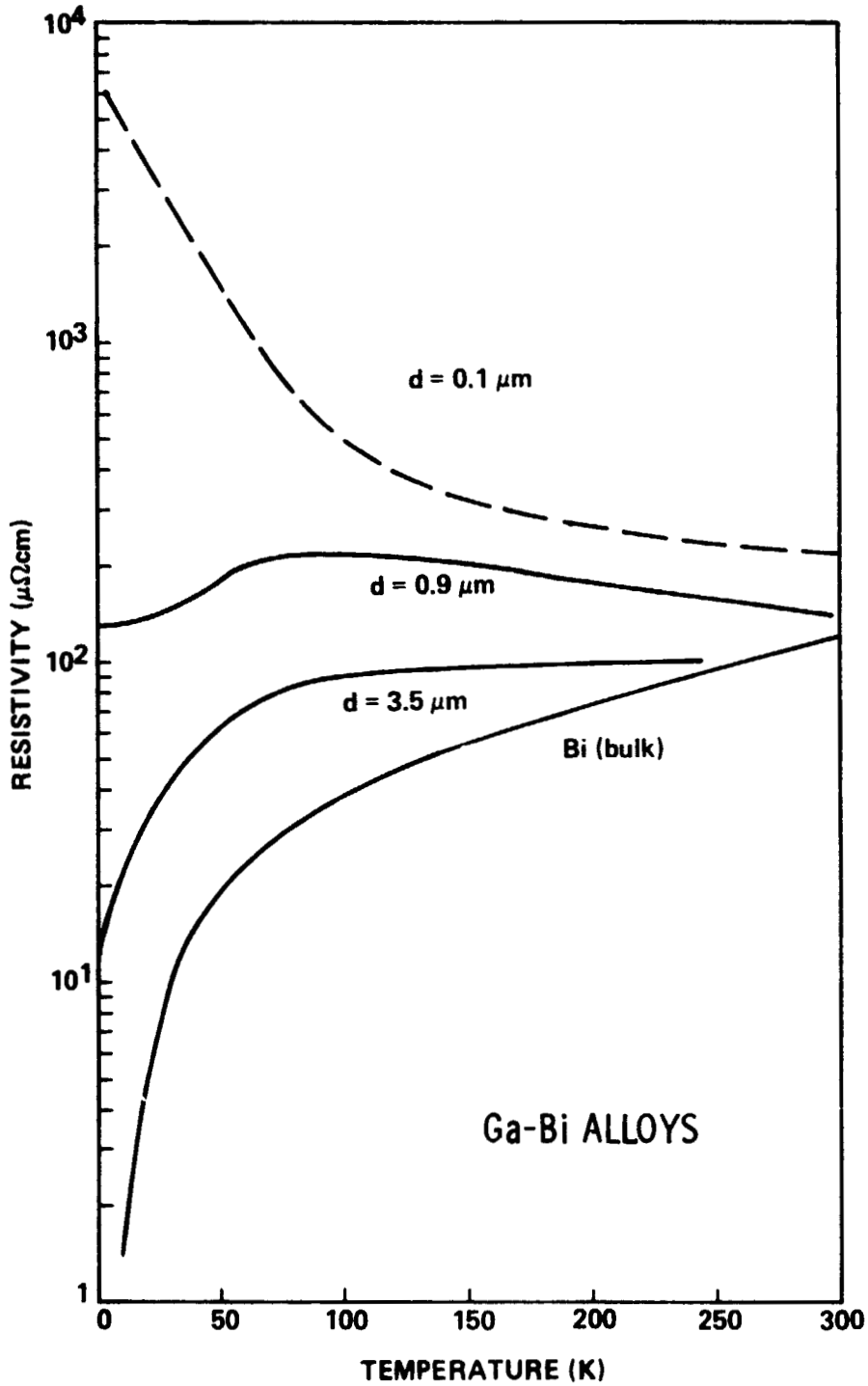


Figure 22b. The extrapolated resistivity curve (dashed) for a Ga-Bi alloy with an average particle diameter of 0.1 μm. The experimental curves (solid) for alloys with larger particle diameters are also included.

Fig. 22b then shows the expected resistivity curve for an alloy with a particle size of 0.1 μm in comparison to selected experimental curves. We realize the dramatic increase of several orders of magnitude in the residual resistivity with decreasing particle size and the disappearing peak. In contrast to a pure semiconductor, the residual resistivity will stay finite at very low temperatures. The electrical properties of such an alloy would eventually resemble those of a semiconducting compound GaBi which, however, does not exist in the phase diagram.

# III. SKYLAB 4 SCIENCE DEMONSTRATION TV-102: IMMISCIBLE LIQUIDS*

## 1. Introduction

A demonstration experiment (TV102) was performed [6] on Skylab 4 to visibly study the behavior of immiscible liquids of different densities in low-gravity as compared to earth. The purpose of the experiment was to investigate the rate of coalescence of two well-characterized liquids, Krytox 143 AZ oil and water, after the liquids were finely dispersed on board Skylab. It was anticipated that, despite the lack of density segregation, a visible amount of separation of the two fluids would occur by coalescence over a time span of 10 hours.

TABLE 8

Characteristic Data for Krytox Oil [33] and Water at Room Temperature (20 °C)

| | Krytox (143 AZ)† | Water |
|---|---|---|
| Viscosity (Centipoise) | 63 | 1.0 |
| Density ($g/cm^3$) | 1.86 | 1.0 |
| Thermal Coefficient of Volume Expansion ($°C^{-1}$) | $11 \times 10^{-4}$ | $2.1 \times 10^{-4}$ |
| Surface Tension (dyne/cm) | 16.0 | 72 |
| Refractive Index | 1.30 | 1.33 |

† Krytox oil is a nontoxic-fluorinated oil with excellent oxidative and thermal stability, and with a high degree of chemical inertness, complete inflammability, and good compatibility with metals, plastics and sealing materials.

* Co-Investigator: Dr. L. L. Lacy, MSFC

## 2. Experimental Details

To study the behavior of immiscible liquids in a low-gravity environment, the classic example [34] of oil and water was chosen because the fluids are transparent and are well characterized by the data given in Table 8. Since the two components of the system are considerably different in density, the dispersion obtained on earth is highly unstable and will separate completely in 10 seconds.

The experimental package designed for the Skylab 4 mission, as shown in Figure 23, consisted of three transparent plastic vials (Oak Ridge Type Centrifuge Tubes, manufactured from unbreakable polycarbonate), each containing a different fraction of oil and red-colored water and mounted in a stainless steel frame. Three vials, each having a total volume of 10 ml., were filled, respectively, with 25, 50, and 75 percent volume of degassed Krytox 143 AZ oil and the remaining volume filled with colored degassed water. To prevent air from being trapped, the vials were sealed while submerged under water, using a screw cap coantaining an O-ring seal. Vacuum tests were performed on ground to insure that the vials would not leak while in orbit. A small brass nut was included in each vial to disperse the liquids when the vials were shaken in zero-g. To separate the two fluids while in orbit, a 50-cm long string was attached to the top of the stainless steel frame containing the vials. The string allowed the astronaut to swing the vials in a circular arc and therby generate a centrifugal force of about 2-g. To enhance visibility and aid in evaluating the results, a card with black parallel lines was installed behind the frame so that the lines would be visible through the liquids. The experiment was designed such that the parallel lines were invisible for a good emulsion and clearly visible when the liquids were separated.

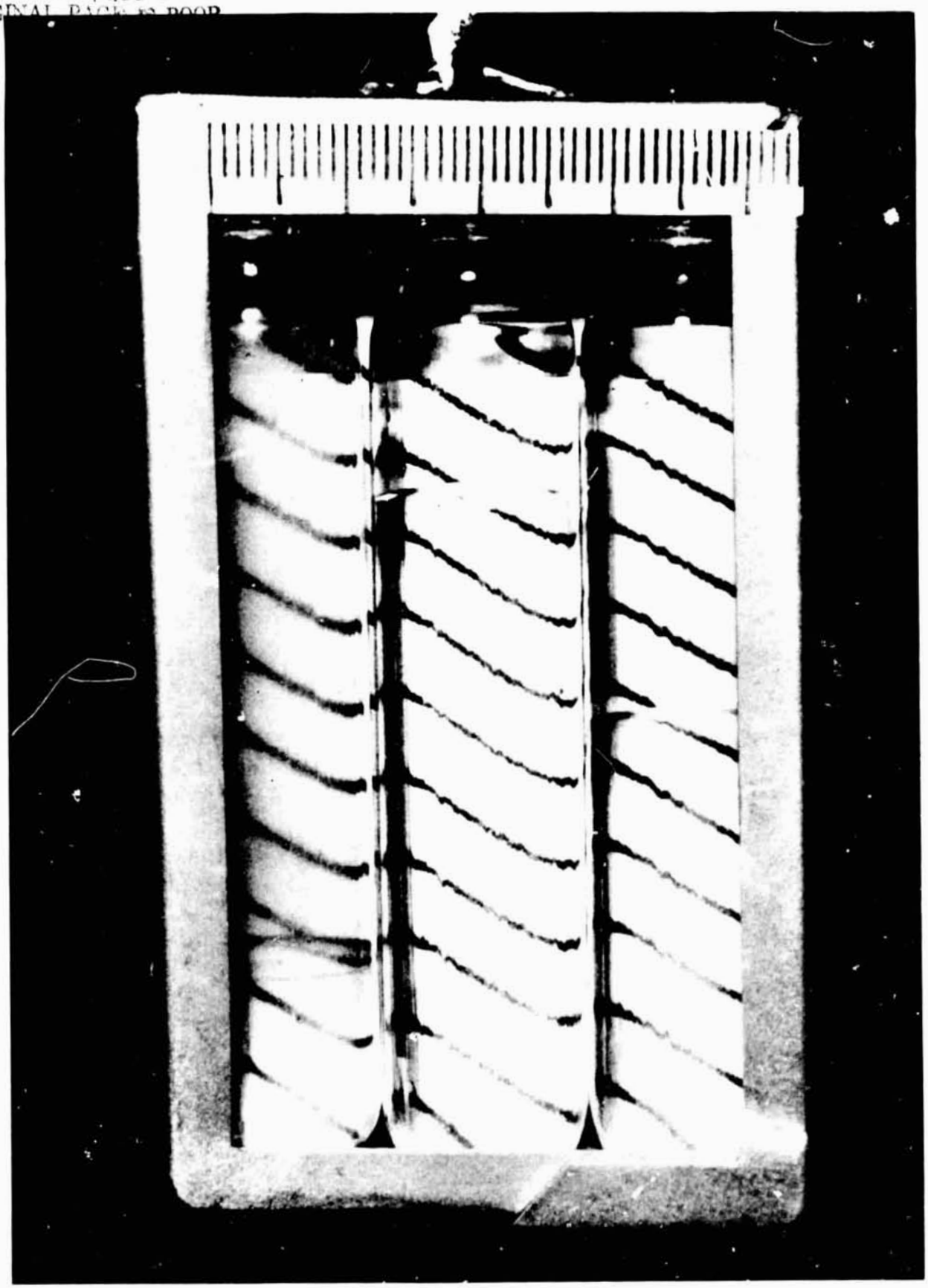

Figure 23. The experimental package of immiscible liquids, as designed for the Skylab 4 mission.

## 3. Experimental Results

Black and white photographs of the emulsions prepared on earth are shown in Figure 23. It can be seen that the dispersions obtained are highly unstable and completely separate in about 10 seconds. The concentrations of oil and water in the three vials are chosen such that, in vial #1 (from left to right), water is the matrix, in vial #2, oil is the matrix, and and vial #3, with a volume ratio of 50 percent, water is again the matrix. At 0.7 second, after the end of the mixing action, it can be seen from Figure 23a that the dispersed oil has completely cleared from the water matrix in vial #1 and #3 because of the low viscosity of the water. Gravity-induced coalescence of the dispersed oil droplets has already occurred. In contrast, vial #2 does not yet show an appreciable amount of density segregation because of the relatively high viscosity of the oil matrix. After 3 seconds, as seen in Figure 23b, the degree of separation by coalescence has progressed, whereas, after 15 seconds (Figure 23c), a complete separation of the two liquids is observed. An evaluation of the high-speed photography reveals that the water droplets are cleared from the oil in the suprisingly short time of 0.1 to 0.2 second, whereas, the oil is cleared from the water in about 10 seconds. The high-speed photographs also reveal that an approximate droplet diameter of 1 mm or smaller can be assumed for the dispersed phase immediately after the dispersing action.

This science demonstration was performed by the Skylab 4 crew (Pilot W. Pogue) on January 3, 1974. After shaking the vials, the appearance of the three emulsions was video taped over a period of 4 minutes and also sequentially photographed over a period of 10 hours. Suprisingly, all emulsions were stable over the entire time period. With an applicable resolution of

# KRYTOX-WATER DISPERSIONS (one-g)

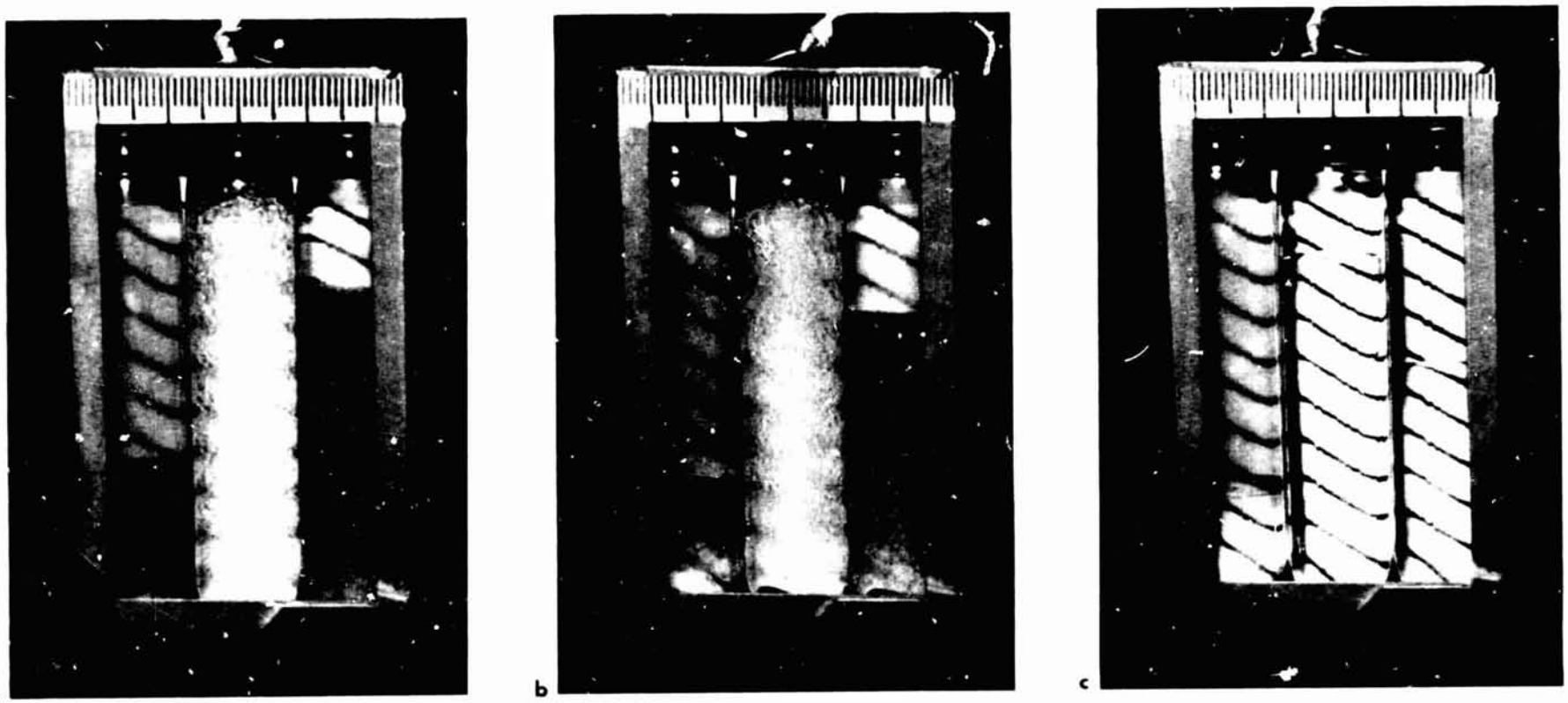


Figure 23. The appearance of the immiscible liquids on earth. a) 0.7 seconds, b) 3 seconds, and c) 10 seconds after mixing. The oil is colorless and located on the bottom of the vials. One division on the scale represents 1

at 2 mm for the pictures, no coalescence or droplets can be observed and none of the background lines are visible through the liquids. Pilot Pogue, however, observed [35] a "cellular structure that grew coarse during the elapsed 10 hours." His observation indicates that there was some coalescence which cannot be resolved in the photographs. Black and white reproductions of color photographs taken from the video tape are given in Figure 24, showing the appearance of the emulsions after 4 minutes. Figure 25 contains two views of the vials (reproduced from 24 x 36 mm slides) after 1.5 minutes and 10 hours. It should be noted that the quality of the original data is much higher than can be reproduced here. The emulsions were indeed separated several times by centrifugal forces, with background lines becoming clearly visible through the liquids (Fig.24b).

The relative stability of the low-g and one-g emulsions was determined by two techniques. The first technique consisted of determining the volume fraction of separation of the dispersions, using the parallel background lines. As gravity-induced segregation separates the emulsions into clear oil and water, the background lines become visible in the pictures and can be counted. The results of such an analysis are shown in Figure 26 where the percentage of separation is shown for vials #1 (water matrix) and #2 (oil matrix) as a function of time after mixing. As seen in Figure 26, the emulsions are highly unstable on earth, with the 25 percent oil mixture showing significant separation in only 0.1 sec, and the 75 percent oil emulsion, a comparable amount of separation in only 0.8 sec. Both vials show complete separation in 2 and 10 sec., respectively. The results for vial #3 (50 percent oil) are intermediate between vials #1 and #2 and have been omitted for clarity. The horizontal error bars for the ground-based experiment represent the

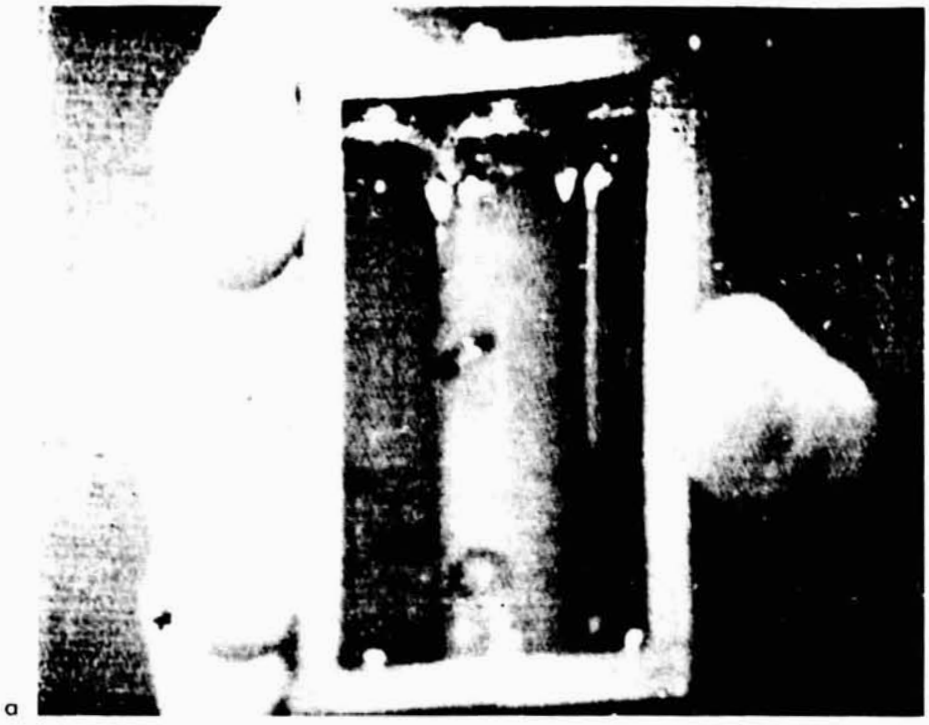

a

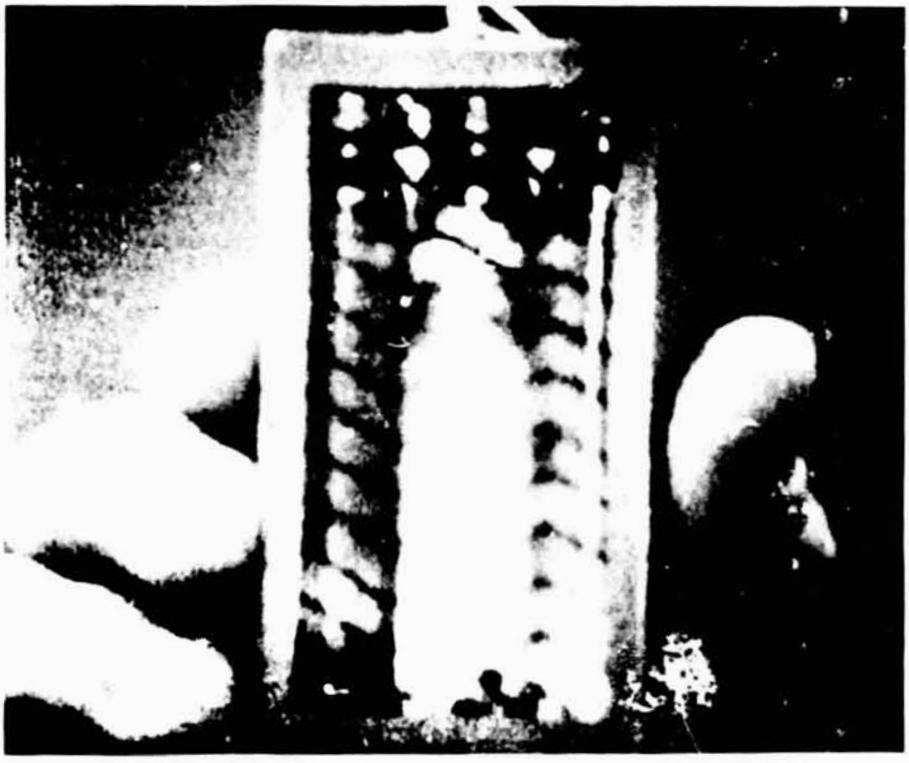

b

Figure 24. Immiscible liquids on Skylab. a) Demonstration of the increased stability of the dispersion in low-gravity. This picture was taken 4 min after mixing and is represen. tive of all the Skylab data. b) Separated liquids by centrifuging on Skylab.

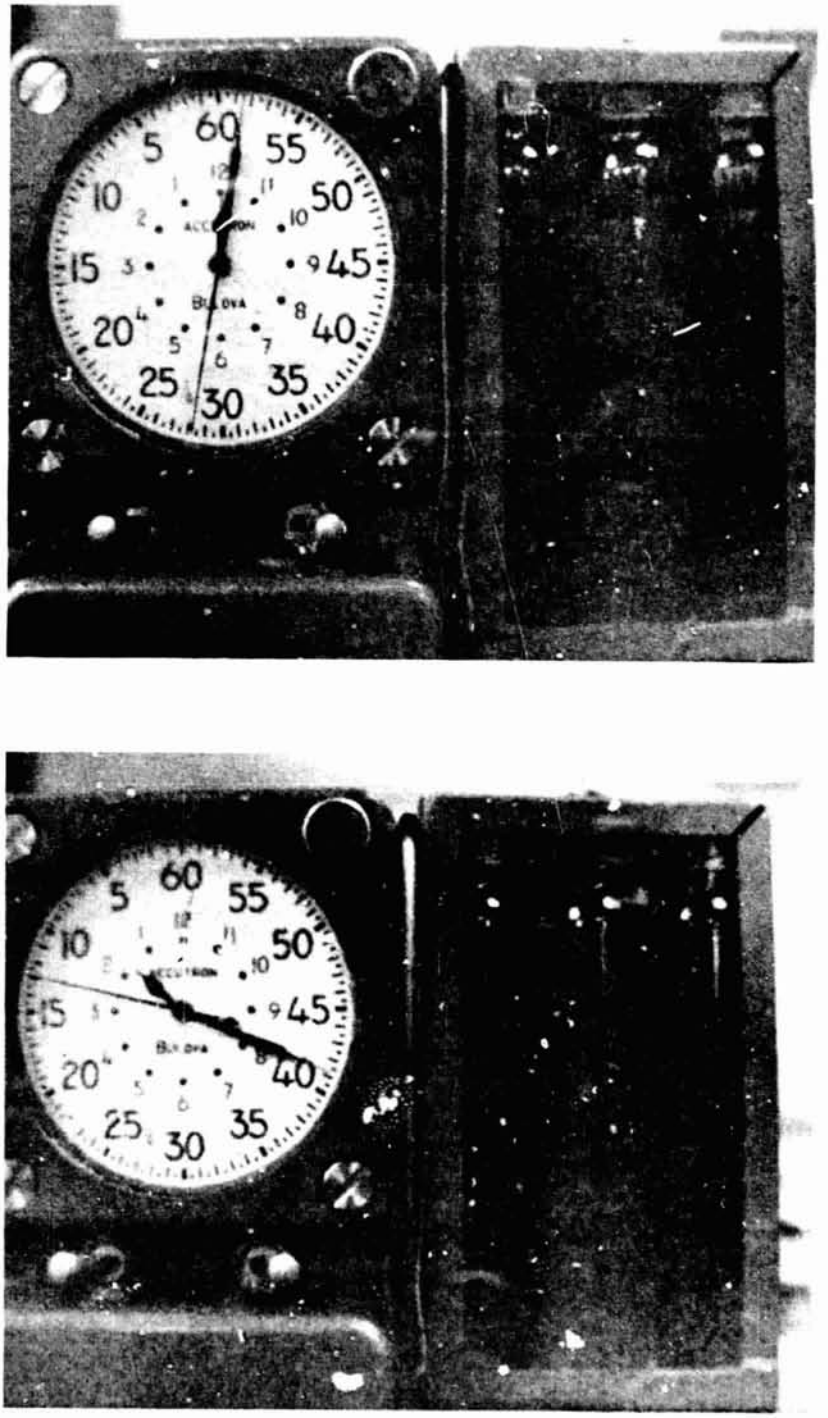


Figure 25. Demonstration of the increased stability of oil/water dispersions in low-gravity. Reproductions from 24x36 mm color slides. The dispersions a) after 1.5 min and b) after 10 hrs.

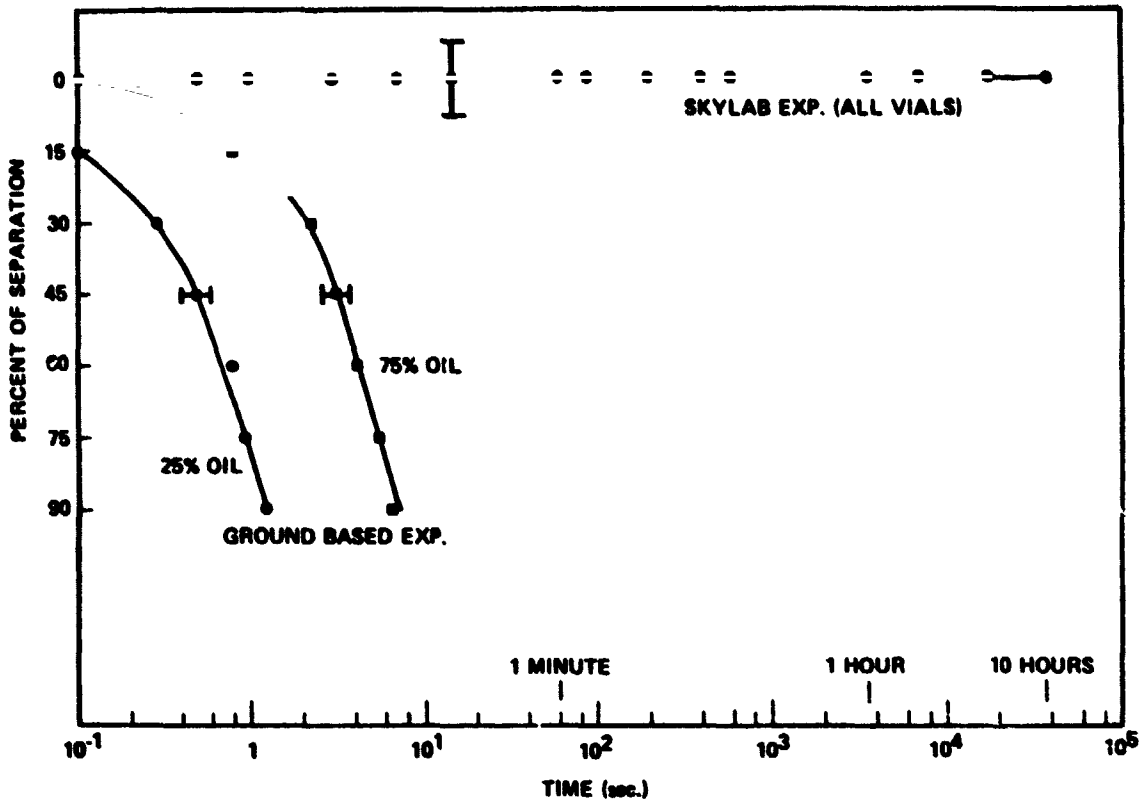


Figure 26. The volume fraction of separation of two oil-water emulsions in low-g and 1-g compared as a function of time. The 25 percent oil mixture is more separated after 0.1 sec on earth than the same mixture is after 10 hr on Skylab.

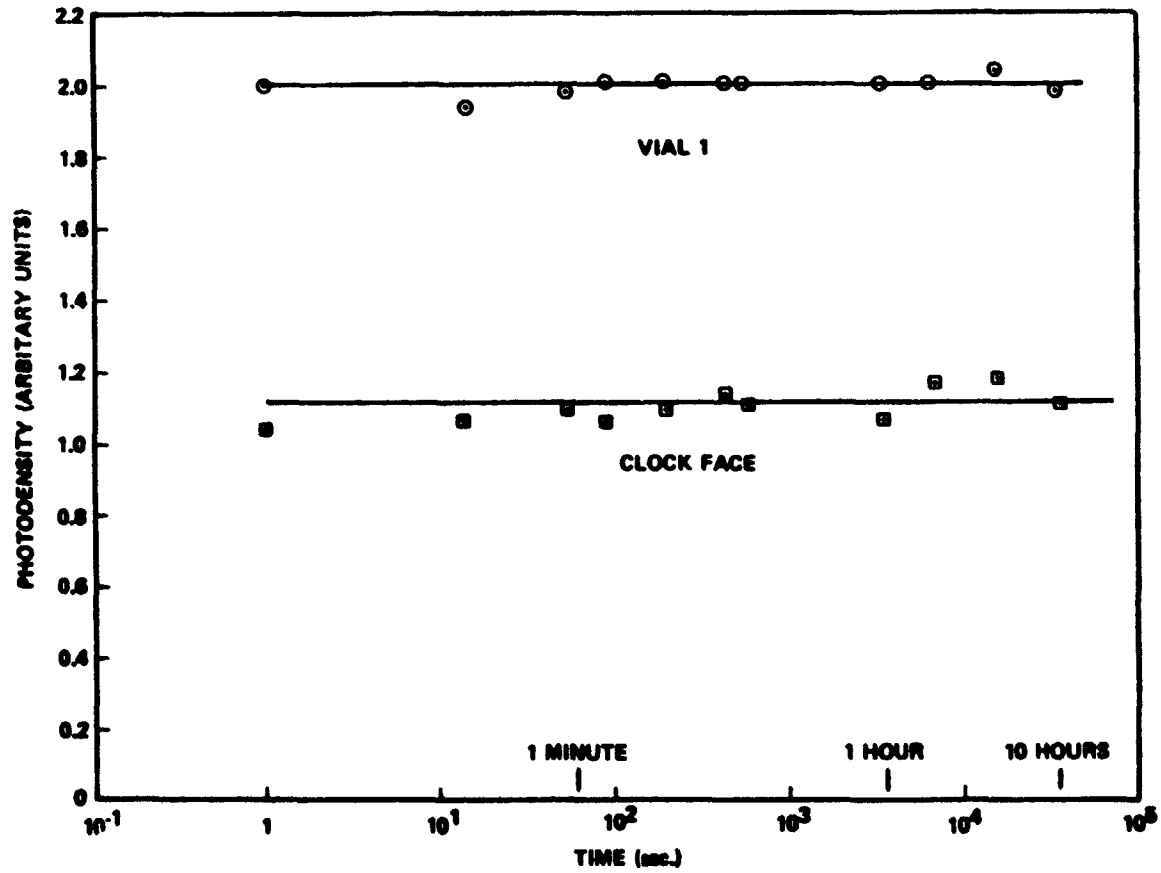


Figure 27. Red (magenta) color density of the returned Skylab film as a function of time after mixing. The white clock face served as a standard.

uncertainty of establishing the time for a given visibility of the background lines. The vertical error bar for the Skylab experiment represents the probable sensitivity for the technique.

As shown in Figure 26, dispersed liquid immiscibles are many orders of magnitude more stable in low gravity than on earth. An estimate of the increased stability in low-g can be made by realizing that the Skylab emulsions are less separated after 10 hr ($3.6 \times 10^4$ sec) than the 25 percent oil mixture is after 0.1 sec on earth. Thus, these results indicate that such dispersed immiscibles are at least a factor of $3.6 \times 10^5$ more stable on Skylab than on earth. Likewise, it can be concluded that the coalescence rate has been reduced on Skylab to $3 \times 10^{-6}$ times that on earth. As shown by the Stokes model calculation, the Skylab emulsions are between one and two orders of magnitude more stable than was expected.

The stability of the low-g dispersions has also been studied by a photodensitometry technique. This technique consisted of measuring the red color density (magneta film dye) of the returned 35 mm color transparencies as a function of time. The results are shown in Figure 27, along with the results of similar measurements made on the white clock face, which acts as a standard. The relatively small scattering of the data is probably associated with the film exposure and processing conditions. The results of the photodensity studies indicate, as with the previous technique, that the low-g dispersions were stable during the 10 hr of observation time.

## 4. Theoretical Considerations and Discussion

When two liquid immiscibles are mixed, one of the fluids will break up into small spheres and be dispersed in the other component which acts as the matrix phase. On earth, the dispersion is often temporary since differences in the density of the two fluids will provide a gravity-dependent buoyancy force. This force will cause the dispersed droplets to move and to collide with other droplets of different velocities and to coalesce. In this section, we will theoretically study the movement (creaming) and coalescence of dropletes with a simple Stokes-model and estimate the minimum time for complete density segregation as a function of the prevailing gravity level.

In gravitational or acceleration field, the spherical droplets will move after the end of the dispersing action, with a velocity, v, given by

$$v = v_t[1-\exp(-t/\tau_o)], \qquad (7)$$

where $v_t$ is the terminal velocity and $\tau_o$ is a characteristic time for achieving the terminal velocity. The droplets will move either upward or downward, depending on the density of the components. One may see from Eq. (7) that the terminal velocity is achieved in a very short time when the exponent becomes negligibly small ($t >> \tau_o$). Using Stokes Law [36], the terminal velocity can be shown to be proportional to the gravity level, g, with

$$v = 2r^2g(\rho_d - \rho_m)9\eta_m, \qquad (2) \text{ and } (8)$$

where $\rho_d$ is the density of the dispersed phase (which consists of spheres with a radius ', and $\rho_m$ is the density of the matrix phase with a viscosity

of $\eta_m$. The characteristic time $\tau_o$ is independent of $g$ and is given by

$$\tau_o = 2r^2\rho_d/9\eta_m. \tag{9}$$

For the oil and water emulsions used in this Skylab experiment, it can be shown, with Eq. (9) and the data of Table 8, that $\tau_o$ is always less than 0.4 second for droplets with $r > 1.0$ mm. This holds for both cases, either the water or the oil being the matrix. Thus, the liquid droplets whose radii are less than 1 mm can always be assumed to be traveling at their terminal velocity as given in Eq. (8). According to Eq. (8), the larger droplets in an emulsion will move with a higher terminal velocity than the smaller droplets. This leads to collisions between the droplets of different diameters and to a subsequent coalescence. In effect, the larger spheres will sweep out and separate the two liquids in an expected separation of coalescence time $\tau_c$ given by

$$\tau_c = L/v_t'(r), \tag{10}$$

where $L$ is a characteristic length, smaller than the length of the vial, and the prime indicates a $v_t$ corresponding to the radius of the larger particles. In this model, we have assumed that coalescence occurs during the time interval it takes for the larger particles to have traveled a distance of approximately the length of the vials. The calculated $\tau_c$ are minimum times needed for a complete separation of the fluids because not every collision will result in coalescence [37]. Calculated values of $\tau_c$ for a one-g field are given in Table 9 for different droplet radii for the 25 percent and 75 percent oil mixtures. The coalescence times for the 50 percent oil mixture (water matrix) will be approximately the same as for

the 25 percent oil emulsion. The slight deviation is caused by different values of the characteristic length.

TABLE 9

Calculated Minimum Coalescence Times for Water/Oil Emulsions Formed in One-g

| Droplet Radius (mm) | $\tau_c$ (sec) for 25% oil | $\tau_c$ (sec) for 75% oil |
|---|---|---|
| 1.0 | 0.027 | 1.7 |
| 0.8 | 0.042 | 2.6 |
| 0.5 | 0.11 | 6.7 |
| 0.4 | 0.17 | 10 |
| 0.3 | 0.30 | 19 |
| 0.1 | 2.7 | 170 |

It can be seen from Table 9 that there is a difference of nearly two orders of magnitude in $\tau_c$ for the same particle size, depending on which fluid forms the matrix. Since the estimated segregation times are very short for the 25 percent oil mixture, it was necessary to use the high-speed photography to study the segregation process in one-g. The results of the high-speed photography indicate that the oil droplets are cleared from the water matrix (vial #1) in 0.1 to 0.2 second and that the water droplets are cleared from the oil matrix (vial #2) in about 10 seconds (see, for example, Fig. 23). Comparing the observed segregation times with the data in Table 9 indicates that the mixing action generates particles with an average radius of 0.3 to 0.4 mm, which is consistent with direct measurements of the radius.

Using a characteristic particle radius of 0.4 mm, we can estimate the minimum times needed to observe segregation in the Skylab experiment. An average acceleration level, during the time $\tau_c$, can be defined as

$$\bar{g} = \int_0^{\tau_c} g(t)dt/\tau_c. \qquad (11)$$

Estimates of minimum $\tau_c$ for various $\bar{g}$ are given in Table 10.

TABLE 10

Estimated Minimum Coalescence Time $\tau_c$ for Various Acceleration Levels $\bar{g}$ That Could be Experienced on Skylab

| $\bar{g}$(g) | $\tau_c$(25% oil) | $\tau_c$(75% oil) |
|---|---|---|
| $10^{-3}$ | 2.8 min | 2.9 hr |
| $10^{-4}$ | 28 min | 29 hr |
| $10^{-5}$ | 4.7 hr | 12 days |
| $10^{-6}$ | 47 hr | 120 days |

In Table 10, the coalescence or separation times estimated by a Stokes-model show that $\tau_c$ is very sensitive to 'g' and to the matrix-forming fluid. Estimates [38] of the prevailing 'g' on Skylab vary between $10^{-3}$ and $10^{-4}$ g. Thus, a minimum coalescence time of less than 30 minutes is expected for vial #1 and of less than 30 hours for vial #2. According to these calculations, a separation of the two fluids should be observed at least in vial #1 and to a lesser degree in vial #2. This, however, is not the case, and, therefore, further refinements have to be made to the model. In conclusion, the model does predict low coalescence rates in space, but these are higher rates than are actually observed. To understand the phenomenon of coalescence in low-g emulsions requires additional studies [39], such as consideration of the vectorial variations of g, and the coalescence efficiency of touching droplets.

## 5. Conclusions

It has been demonstrated that stable dispersions of two immiscible liquids which are unstable on earth can be prepared in space. The amount of coalescence observed over the period of several hours is smaller by a factor of at least $3 \times 10^{-6}$ in low-g compared to one-g and could not be observed photographically because of limitation in resolution. Theoretical estimates, however, support the evidence that the rate of coalescence is small at the normally experienced gravity levels ($10^{-3}$ to $10^{-4}$ g) in space. A simple Stokes model for the fluid segregation works well for the one-g case, but requires further refinements, such as the gravity dependence of the coalescence rate, for the low-g case.

# IV. SKYLAB 3 SCIENCE DEMONSTRATION TV-111: ICE MELTING*

## 1. Introduction

The low-gravity environment associated with Skylab has recently provided extensive experimental results in the area of materials sciences [41]. These investigations consisted mainly of studying the returned materials that were melted and then resolidified in low-gravity. The purpose of this science demonstration (SD-16) was to visibly study the melting process in space with the absence of convective heat transfer and compare it with the same process on earth. The experiment was made possible by the request of the Skylab 3 crew during their mission for additional scientific investigations [6]. This science demonstration [42] was designed to simulate the essential aspects of the melting process in low-gravity as a representation for the technique of containerless melting. The ice/water system was selected because of the availability of the necessary materials on board, the negligible impact on the mission, the ready availability of all significant data, and the good visibility of the solid/liquid interface which represented a "transparent furnace".

In this section, we will discuss the heat flow into a solid material which is melted by an isotropic heat source. The integrated heat input into such a system is experimentally available through the image of the time-dependent solid/liquid interface of the melting ice. This melting process, both on the ground and in a low-gravity environment, will be analyzed in regard to the classical modes of heat transfer by radiation, conduction, and convection. It can be expected in low-g that the heat input is strongly affected by the reduced mode of convective heat transfer.

---

* Co-Investigator: Dr. L. L. Lacy, MSFC

## 2. Experimental Details

An ice cylinder was frozen by the crew on-board Skylab 3 by receiving instructions from the ground. A specified amount of water from the drinking water dispenser was injected in an empty plastic pill container (30 mm dia. and 75 mm long) which had a wooden cotton swab inserted to provide support for the ice. Astronaut Jack Lousma reported [42] that he "shook the water to the point where it did not have any bubbles to speak of in the solid mass." After freezing overnight in the on-board food freezer [43], the ice and container were weighed in space and, from five mass measurements, an average value of 49.4 $\pm$ 0.2 g was given. After making the necessary corrections for container and cotton swab, the mass of the ice to be melted was found to be 39.7 $\pm$ 0.2 grams (1.40 oz). With the heat of fusion for ice being 79.8 cal/g, a total of 3,170 cal or an equvalent of 13,250 Wsec is needed for the complete melting process.

The ice, contained on a cotton swab, was mounted in the field of view of a data acquisition camera so that the cylinder could melt freely into a sphere of water as shown in Fig. 28. Also visible were a portable clock and a thermometer. The air velocity at the location of the experiment was measured by the astronaut and was found to be negligible. The air temperature at this location was read as 78 °F (25.5 °C). These background data are summarized in Table 11.

The Skylab experiment was carefully duplicated in the laboratory with regard to air temperature, atmospheric pressure (5 psia) and gas composition (75% $O_2$, 25% $N_2$). A partial view of the ground-control setup in a bell jar is shown in Fig. 29. For the ground-control experiment, the melt-water was collected in a measuring beaker. Volume readings ($\pm$ 0.1 $cm^3$) were made every 5 min, and thus an accurate value of the accumulative heat

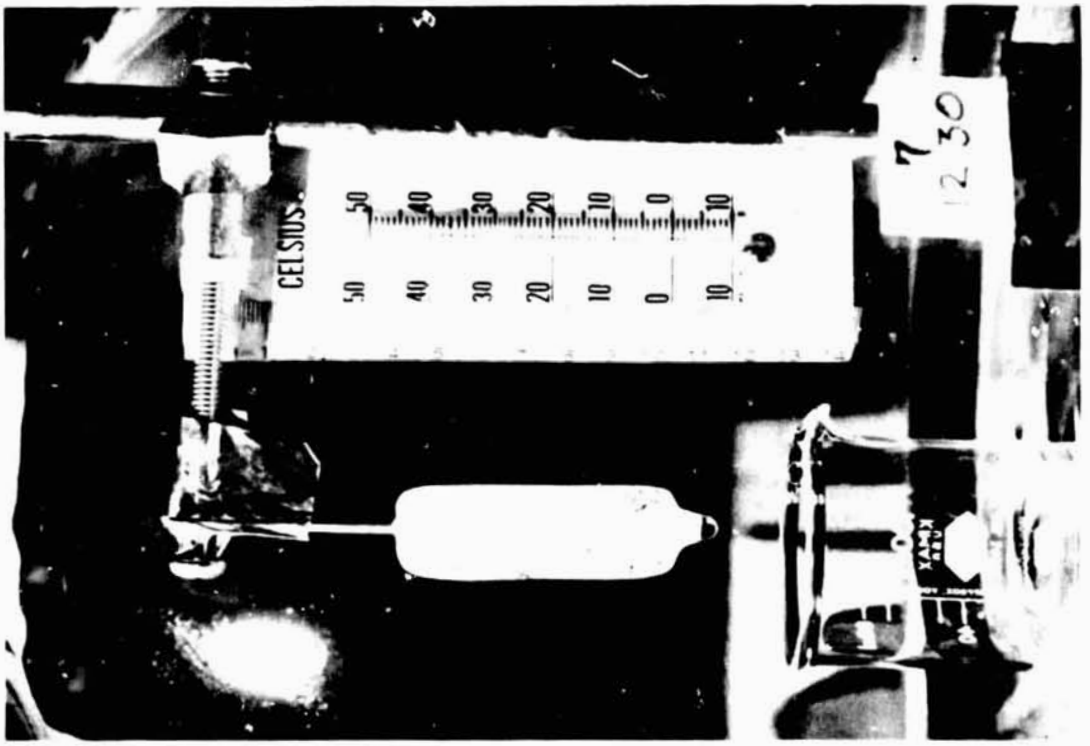


Figure 29. The experimental set-up for the ground control ice melting.

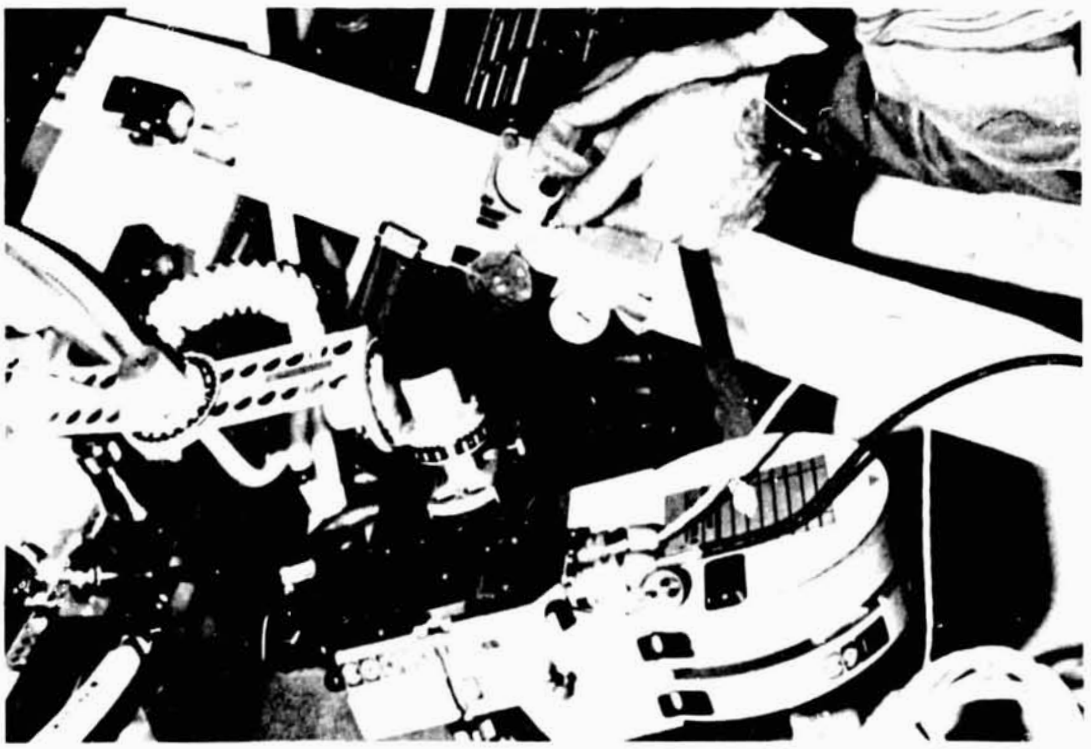

Figure 28. The experimental set-up for the Skylab ice melting.

TABLE 11. SUMMARY OF DATA FOR THE LOW-G ICE MELTING EXPERIMENT

| | |
|---|---|
| **Primary Skylab Data** | |
| Mass of ice with container and swab (g) | 49.4 ± 0.2 |
| Inner diameter of plastic container (cm) | 3.0 |
| Air temperature (°C) | 25.5 ± 0.3 |
| Air velocity (cm/s) | 0 ± 0.5 |
| Total melting time (min) | 190 ± 5 |
| **Derived Data** | |
| Mass of ice (g) | 39.7 ± 0.2 |
| Ice cylinder: | |
| Volume ($cm^3$) | 43.2 |
| Diameter (cm) | 3.0 |
| Length (cm) | 6.1 |
| Surface Area ($cm^2$) | 71.6 |
| Density ($g/cm^3$) | 0.918 |
| Water sphere: | |
| Volume ($cm^3$) | 39.7 |
| Surface Area ($cm^2$) | 56.3 |
| Radius (cm) | 2.12 |

input into the ground-control ice cylinder was obtained. The first derivative of this curve with respect to time gives the instantaneous heat flow rate ($\dot{Q}_{total}$). Average values for the length and diameter of the melting cylinder were obtained from the photographic record. Similar curves were generated from the Skylab data.

## 3. Experimental Results

### a. General Observations

The melting ice cylinder was intermittently photographed by the astronauts 22 times with an approximate time interval of 10 min. Some selected views are given in Fig. 30. Although the pictures are slightly out of focus, the objectives of this investigation are completely fulfilled and the following details can be taken from the photographs:

1. General appearance of the ice
2. Time-dependent shape of the water-ice globule
3. Time-dependent location of the water-ice interface
4. Total melting time

A study of the returned film results in some of the following observations:

1. The total melting time in zero-gravity for the specified ice cylinder was 190 $\pm$ 5 min. This duration is in accordance with voice transcripts from the astronauts [42] which can be correlated with the photographs. The total melting time for an identical ice cylinder on earth is 130 $\pm$ 2 min.

2. The cylindrical ends melt first, while the diameter of the ice decreases slowly.

3. The water from the melting ends is driven by surface tension onto the cylindrical surfaces.

45 min

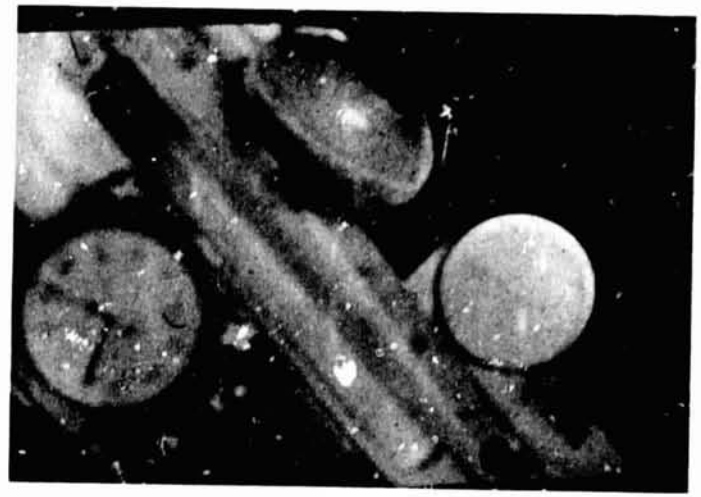

80 min

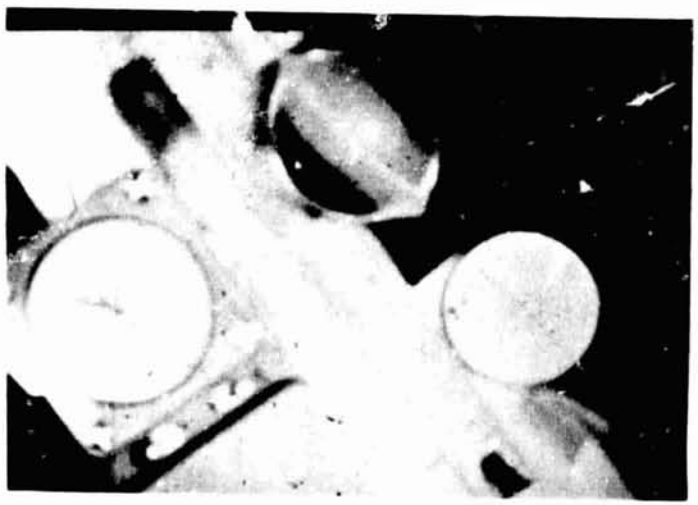

115 min

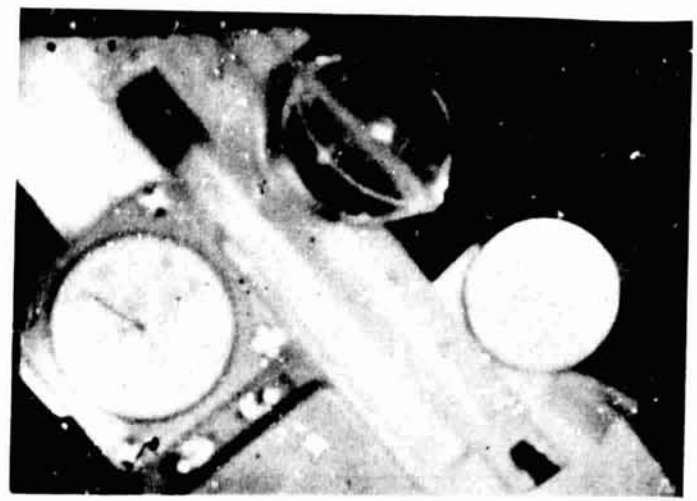

180 min

Figure 30. The melting ice cylinder on board Skylab after 45, 80, 115, and 180 minutes.

4. The overall shape goes from cylindrical to spherical with an intermediate approximate ellipsoidal shape. A spherical shape of the water ice globule is first evident at half of the total melt time when the water completely surrounds the melting ice.

b. Dimensional Analysis

In order to obtain the temperature-dependent amount of melt water in the low-g melting needed for heat flow consideration, the volume of the remaining ice was calculated from the dimensions obtained from the photographs. A cylindrical shape of the ice could be reasonably taken during the whole melting process. The photographic dimensions were tied to the real dimensions of the system by our knowledge that the total amount of water in spherical form was 39.7 $cm^3$. Corrections have been applied for the diameter of the ice cylinder because of a distortion due to the lens effect of the water globule and for the differences in specific volume between water and ice. The measured length and diameter of the ice cylinder in zero-g, as a function of melting time, are given in Fig. 31. Whereas, the total melting may be defined as a condition existing for d = 0, the length approaches a finite value as the diameter approaches zero. The same considerations apply for melting in one-g. For the ground control case, the dimensions of the cylinder are also plotted in Fig. 31. In comparing the dimensions for the low-g and one-g melting, a large difference in length and diameter is noted. The length, in the low-g case, decreases faster with time when compared with the one-g conditions; however, after 100 min, it reaches a finite value determined by the diameter of the water globule.

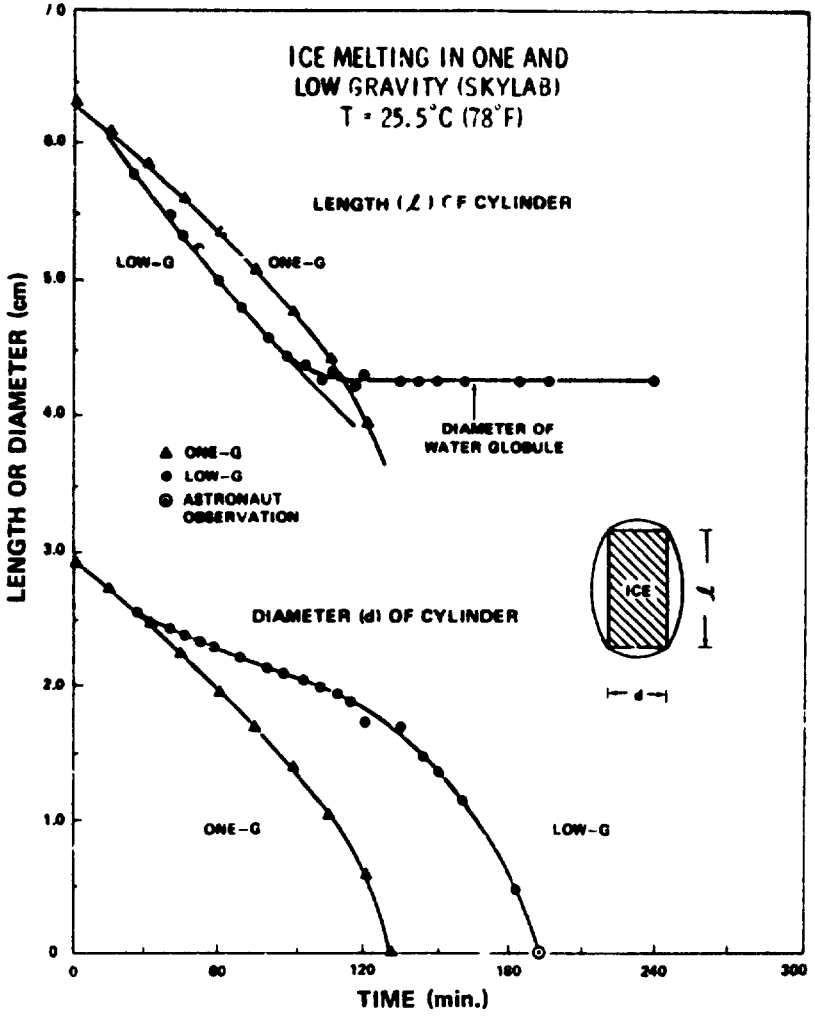


Figure 31. Time dependent dimensions of the melting ice cylinder on earth and on Skylab.

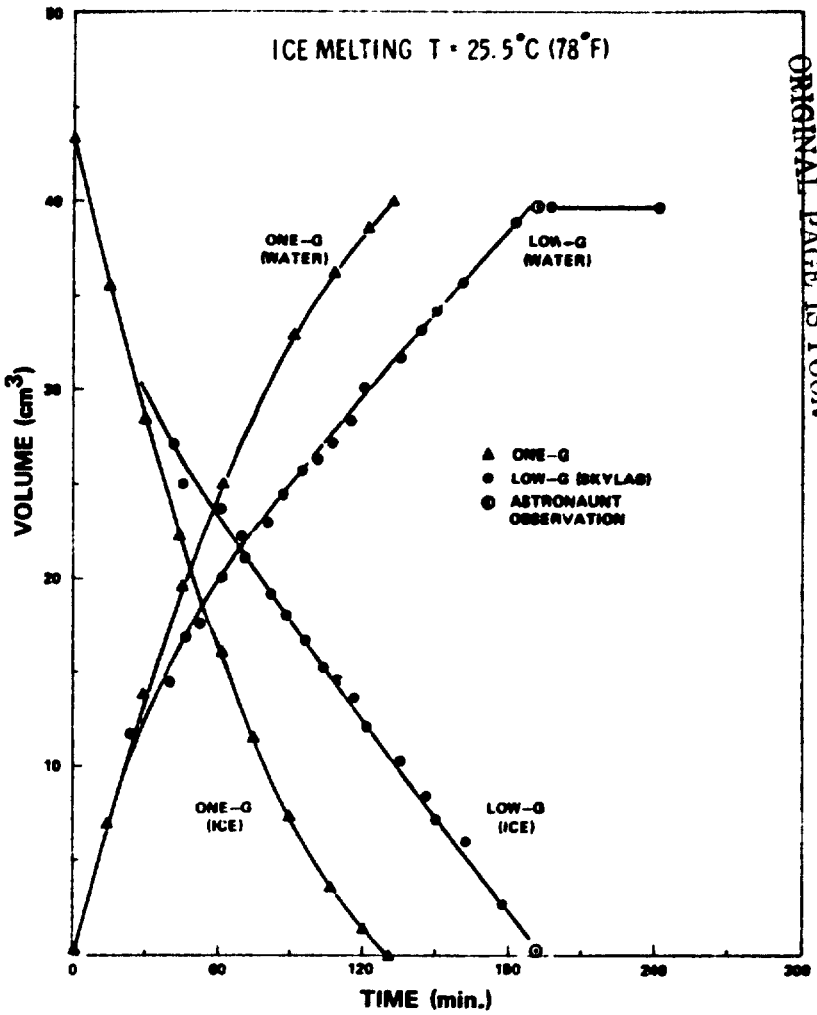


Figure 32. Time-dependent volume of ice and water for melting on earth and on Skylab.

Using the data from Fig. 31, the time-dependent volume of water and ice can be calculated for the melting ice. These volumes are given in Fig. 32. The volume for the ground-control case, which was measured directly, is also given in Fig. 32. Again, the end of the melting process is determined by the condition $d_{ice} \rightarrow 0$. The astronauts' observation for total melting agrees well with the extrapolation obtained from the experimental data. It should be mentioned that the change in volume of ice or water with time is a smooth non-linear curve for the ground experiment, whereas, it is a linear function of time for the Skylab experiment ($t > 70$ min). On the basis of these curves, the experimental total heat flow into the ice will be derived and will be compared with theoretically expected values of heat flow for both the low-g and one-g melting.

## 4. General Heat Flow Analysis

The transfer of energy (latent heat) arising from the temperature difference between the melting ice and its surroundings can be achieved by the following mechanisms:

Radiation

Conduction

Convection.

An experimental measure for the time dependence of the total heat flow is the amount of melt water being generated. We will now theoretically calculate the individual heat inputs into the ice cylinder and then compare the sum of the individual contributions with the experimentally observed values. We should thus be able to explain the progress of melting on ground and in low-g. To simplify the calculations, the surface temperature of the melt

water is assumed to be 0 °C. The impact of this simplification on the experimental results will be discussed later.

We will, however, not consider minute convective currents, caused by g-jitter [44] or surface tension driven convection [45] because the obtained data is not sensitive enough to these effects.

a. Heat Transfer by Radiation

The ice is surrounded by air at the temperature of 25.5 °C [46], which emits thermal radiation with the wave-length of $\sim$ 10 μm. The absorptivity $\alpha$ of ice [47] for this wavelength is 0.95, indicating nearly complete absorption of this infrared black-body radiation. The Stefan-Boltzmann law can be applied for the calculation [48] of the radiative heat flow $\dot{Q}$ from the surrounding ($T_2$ = 298.5 K) to the ice ($T_1$ = 273 K) as

$$\dot{Q} = A\sigma\alpha\left(T_2^4 - T_1^4\right), \qquad (12a)$$

where A refers to the area of the ice and $\sigma$ is the Stefan-Boltzmann constant with the value of $\sigma = 5.67 \times 10^{-12}$ W cm$^{-2}$ deg$^{-4}$. The quantity $\sigma\alpha\left(T_2^4 - T_1^4\right)$ for the stated temperatures yields the value of

$$\dot{Q}/A = 0.0128 \text{ W/cm}^2. \qquad (12b)$$

The surface area of the ice during melting is not constant but changes as a function of time in Skylab as well as on the ground. The area A of the ice cylinder at the start of the melting (t = 0) can be derived as 71.6 cm$^2$. We have neglected the contribution of the gas bubbles and the wooden swab (2 mm diameter; v = 0.2 cm$^3$) to the surface area since their contributions tend to increase the surface area only slightly. After complete melting of the ice on Skylab, a water sphere is formed with the volume of 39.7 cm$^3$, having a diameter of 4.24 cm and a surface area of 56.3 cm$^2$. The complete melting causes a decrease in surface area of about

22%. Evaporation losses over the three-hour period can be neglected because it has been shown in the laboratory simulation that they are less than 1.5% by volume.

With Eq.(12b), two heat flow rates by radiation can now easily be calculated:

At the start of the melting process and, after 90 min melting on Skylab when the melt water first showed a spherical appearance.

$$\dot{Q}\ (t=0) = 0.919 \text{ Watt} \quad \text{or} \quad 0.219 \text{ cal/sec}$$

$$\dot{Q}\ (90 \text{ min}) = 0.720 \text{ Watt} \quad \text{or} \quad 0.172 \text{ cal/sec}$$

The heat flow obtained for t=0 is also the same for the ground control experiment. However, to calculate the flux at any other time, the changing surface has to be considered.

b. Heat Transfer by Conduction

Energy is transferred to the ice by means of heat conduction from the surrounding atmosphere (being at 25.5 °C). For the magnitude of this quantity, the thermal conductivity K of the conducting medium and the temperature difference are of prime importance. Since gases are generally poor heat conductors, it is expexted that this contribution will be small. To exactly calculate the conductive heat flow, the differential equation

$$\dot{Q} = - K \text{ grad } U(r, T) \qquad (13a)$$

has to be solved for the cylinder. We will approximate the expected result by calculating the heat flow into a sphere of ice, having the same volume as the cylinder. Then Eq.(13a) transforms into the simple relationship.

$$\dot{Q} = 4 K r_1 (T_2 - T_1), \qquad (13b)$$

where $r_1 = 2.18$ cm is the radius for the equivalent ice sphere. Using

the conductivity K for dry air or oxygen [47] as $K = 2.59 \times 10^{-4}$ Watt $cm^{-1}$ $deg^{-1}$, then the following approximate conductive heat flow can be calculated

$$\dot{Q}\ (t = 0) = 0.180 \text{ Watt} \quad \text{or} \quad 0.042 \text{ cal/sec.}$$

We see that the heat flow by conduction is only one-fifth of the heat flow by radiation. After 90 min in low-g melting, a sphere with $r_1 = 2.13$ cm is formed and then the exact heat flow of

$$\dot{Q}\ (t=90 \text{ min}) = 0.176 \text{ Watt} \quad \text{or} \quad 0.041 \text{ cal/sec}$$

is generated.

c. Heat Transfer by Convection

The con tions for natural convection will apply since the air surrounding the ice is not in a forced movement. Gravity causes the heavier cold air to move along the outside ice and sets convective currents in motion. The gravity field is the "pump" in this type of convection and the room temperature air supplies heat steadily to the melting ice. On ground, accumulated melt water drops off and we may assume it to have the temperature of 0 °C. Of dominant importance for the exact treatment of natural convection are the dimensionless quantities, like Grashof, Prandtl and Nusselt numbers. We will not calculate those numbers directly for the experiment but rely instead on published data.

Generally, the Newton Rate Equation,

$$\dot{Q} = hA(T_2 - T_1), \tag{14}$$

can be applied to this problem where the convective heat transfer coefficient h, which is a product of the above mentioned numbers, has to be determined for the specific geometry. According to McAdams [49],

the heat transfer value for cylinders is given approximately as

$$h = \frac{-}{+} \left( \frac{T_2 - T_1}{\ell} \right)^{1/4}, \qquad (15)$$

with $\ell$ being the length of the cylinder. A value of $F = 5.1 \times 10^{-4}$ Watt $cm^{-7/4}$ $deg^{-5/4}$ has been used for the calculations, [49] accounting also for a 10% overall contribution of the end caps. With $T_2 = 25.5$ °C, the value for h becomes $7.3 \times 10^{-4}$ Watt $cm^{-2}$ $deg^{-1}$ and should be accurate to within 5% [49].

The value of h can be put in Eq. (14) to yield:

$$\dot{Q}\ (t=0) = 1.33 \text{ Watt} \quad \text{or} \quad 0.321 \text{ cal/sec.}$$

The convective heat input is by about 50% larger than the radiative contribution.

In order for Eq. 15 to be applicable, it is essential that laminar flow of air around the ice does exist. We have verified the laminar air flow with laser interferometry of an orthorhombic piece of ice having a nearly rectangular cross section. The orthorhombic structure had to be chosen to achieve high temperature sensitivity by increasing the path-length of the light along the ice. A detailed description of the set-up is published elsewhere [50]. The interference pattern in Fig. 33* represents isotherms around the ice with one ring generated for every five degrees change in temperature. The temperature difference in the experiment was about 21 °C. It is also demonstrated in Fig. 33 that the temperature gradient sustained in air is very steep, that one centimenter away from the vertical surface of the ice room temperature conditions are already

---

* We would like to thank Dr. A. Martin of Athens College and Dr. R. L. Kurtz of MSFC for supplying us with the photograph.

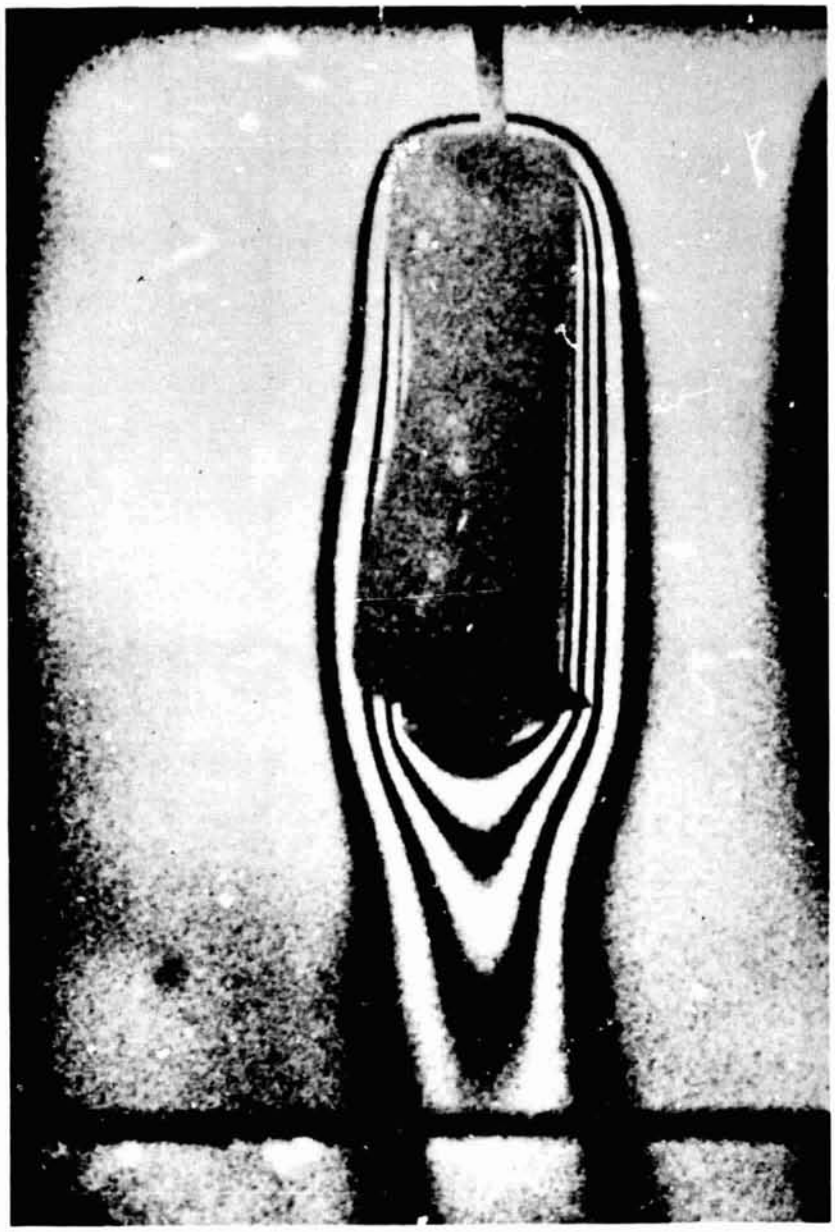

Figure 33. Verification of laminar air flow around melting ice in the ground control experiment. Temperature profile made visible by laser interferometry.

established. The interference pattern on the left side of the picture is partially covered by a protruding piece of ice and by optical parallax.

d. Total Heat Transfer

Fig.34, calculated from Fig.32, contains the time-dependent accumulative heat inputs for both the ground control and Skylab melting. Both curves end when a total of 3.17 kcal has flowed into the ice, representing complete melting. For the ground-based melting, the total theoretical heat input at the beginning of the melting process would be

$$\dot{Q}_{total}\ (t=0) = 0.582\ \text{cal/sec} \qquad \text{(Theory)}$$

This value compares with the experimentally obtained total heat flow from Fig.34 during the first 10 min of the ground-based melting

$$\dot{Q}_{total}\ (t=0) = 0.610\ \text{cal/sec.} \qquad \text{(Experiment)}$$

Although it will not be shown here, we have found [52] that the theoretical experimental values of the total heat flow agree to within 6% over the entire melting duration. Therefore, it can be concluded from these calculations that for the ground-based melting, the total heat flow is achieved by the following individual contributions:

convection (55%)

radiation (38%)

conduction ( 7%)

These findings are schematically illustrated in Figure 35.

An accurate record for the first 10 min of melting on Skylab is not available. However, very good data of volumes are obtained for $t > 50$ min up to the total melting time. According to Fig.34, a constant heat flow of 0.203 cal/sec in the melting ice is observed for $t > 60$ min. This

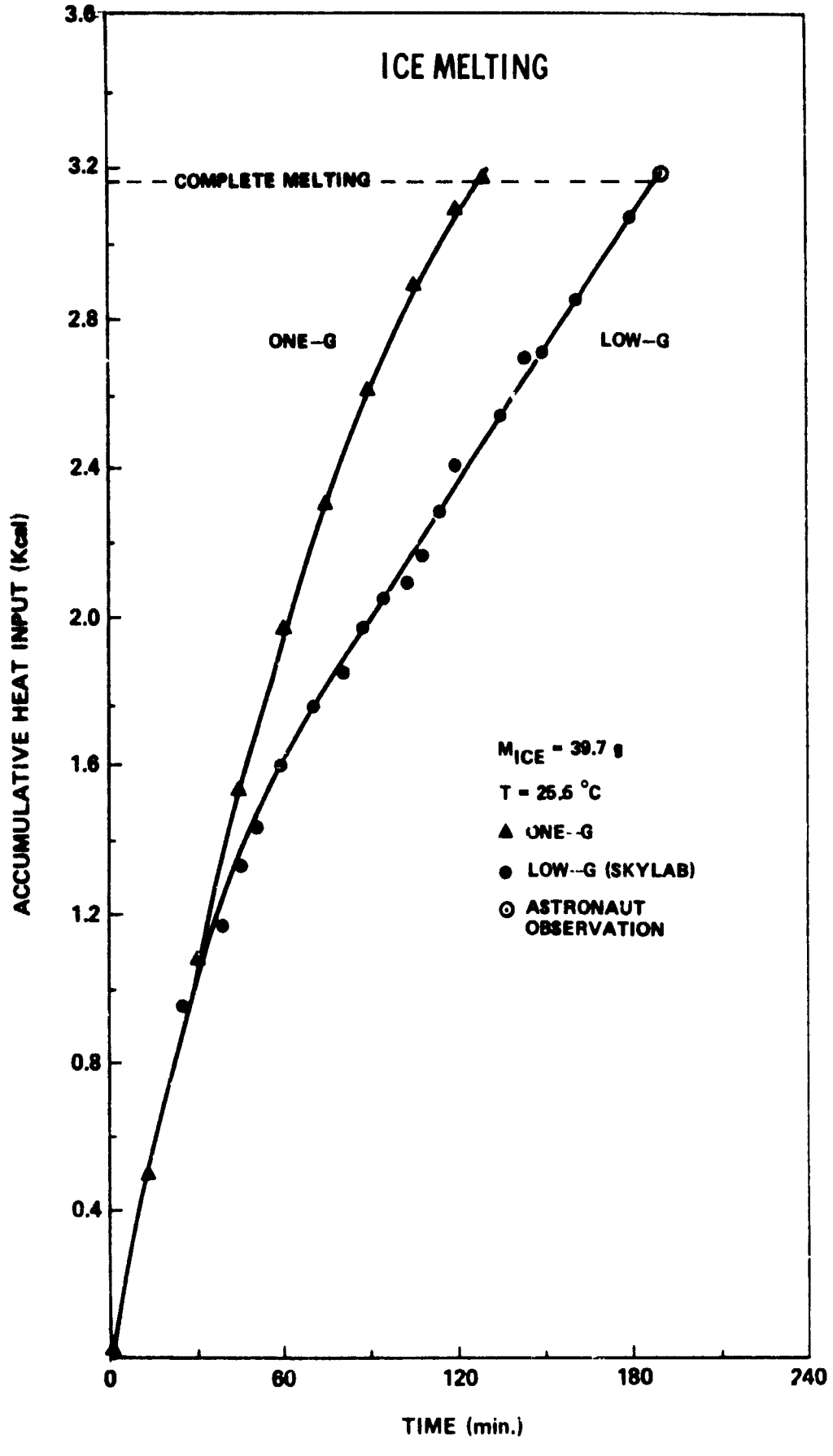


Figure 34. The accumulative heat input into melting ice on earth and on Skylab.

corresponds to the stage when spherical symmetry is achieved. We have already theoretically derived the radiative heat flow at t = 90 min to be 0.172 cal/sec. Adding to this value the expected conductive contribution on Skylab with 0.041 cal/sec gives a subtotal value of 0.213 cal/sec. This amount is comparable with the experimentally observed value, leaving no room for a convective heat flow contribution. The Skylab data for t > 60 min rule out the existence of any convective heat transfer.

Thus, it may be concluded that in low-g, the latent heat of melting is supplied by

radiation (81%)

conduction (19%)

as schematically illustrated in Fig. 35.

The first useful data from the Skylab record are obtained 40 min into the melting. From Fig. 34, an average total heat flow of 0.480 cal/sec for this time span is derived. This value is 0.220 cal/sec higher than the maximum allowable heat input by conduction and radiation for t = 0 (0.261 cal/sec). An explanation for this discrepancy could be that the handling of the ice by the astronaut (weighing, mounting) caused some ice already to melt by body heat before the recording started.

e. Secondary Considerations

Certain simplifications have been applied during the course of the computations for the theoretical heat input. The implications on the results obtained will be discussed below.

In order to determine the radiative heat input into the melting ice on Skylab, a surface termperature of 0 °C of the melt water was assumed. This assumption is probably only true for the first part of the melting

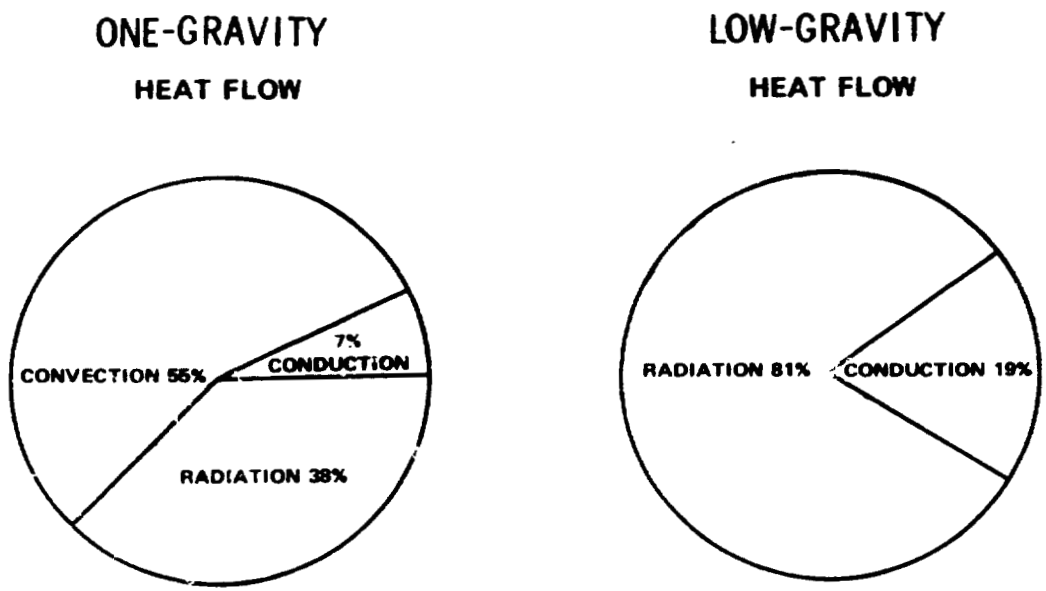


Figure 35. Schematic representation of the heat flow in one-gravity and low-gravity.

process. A 2 °C rise of the surface temperature will affect the amount of the radiative heat input by 7%. Such a 2 °C temperature differential can be sustained over a water thickness of between 0.6 and 2 cm, depending upon the geometry considered. Such a water thickness can only occur during the latter stages of the melting process (i.e., t > 60 minutes) and even then preferentially only at the equator.

A negative heat input into the water/ice system can be caused by evaporation losses of the melt water. Ground-based experiments at 1 °C have been performed which indicate that a maximum of 1.4 volume percent of the water could have evaporated during the 3-hour period of the experiment. This would account for a maximum negative heat flow of 0.025 cal/s which is 10% of the total heat flow. Experimental data of evaporation losses from a free water surface are given in Fig. 36. If a negative heat input is added to the total theoretical heat input, the theoretical results could come closer to the experimental results.

The experimental results for the melting on Skylab can be explained by disregarding any convective heat flow. However, a steady air stream with an average velocity of 2.5 cm/sec was maintained in the workshop area for circulation. The ice melting on Skylab was performed below water tank #2, in an area selected by the astronauts for minimum air flow. The air velocity measured was less than 0.5 cm/sec, the lowest meaningful reading on the air flow meter. We would like to consider the worst possible case of a flow with this magnitude. Because of the low heat conductivity of air, the temperature gradient close to the surface is in the order of 50 °C/cm. We assume a convective heat input of streaming air moving along the ice with a velocity of 0.5 cm/sec and a thickness of 1 cm. This worst case analysis indicates that the air stream will contribute an energy of no more than 0.021 cal/sec or 7% of the total energy required for melting.

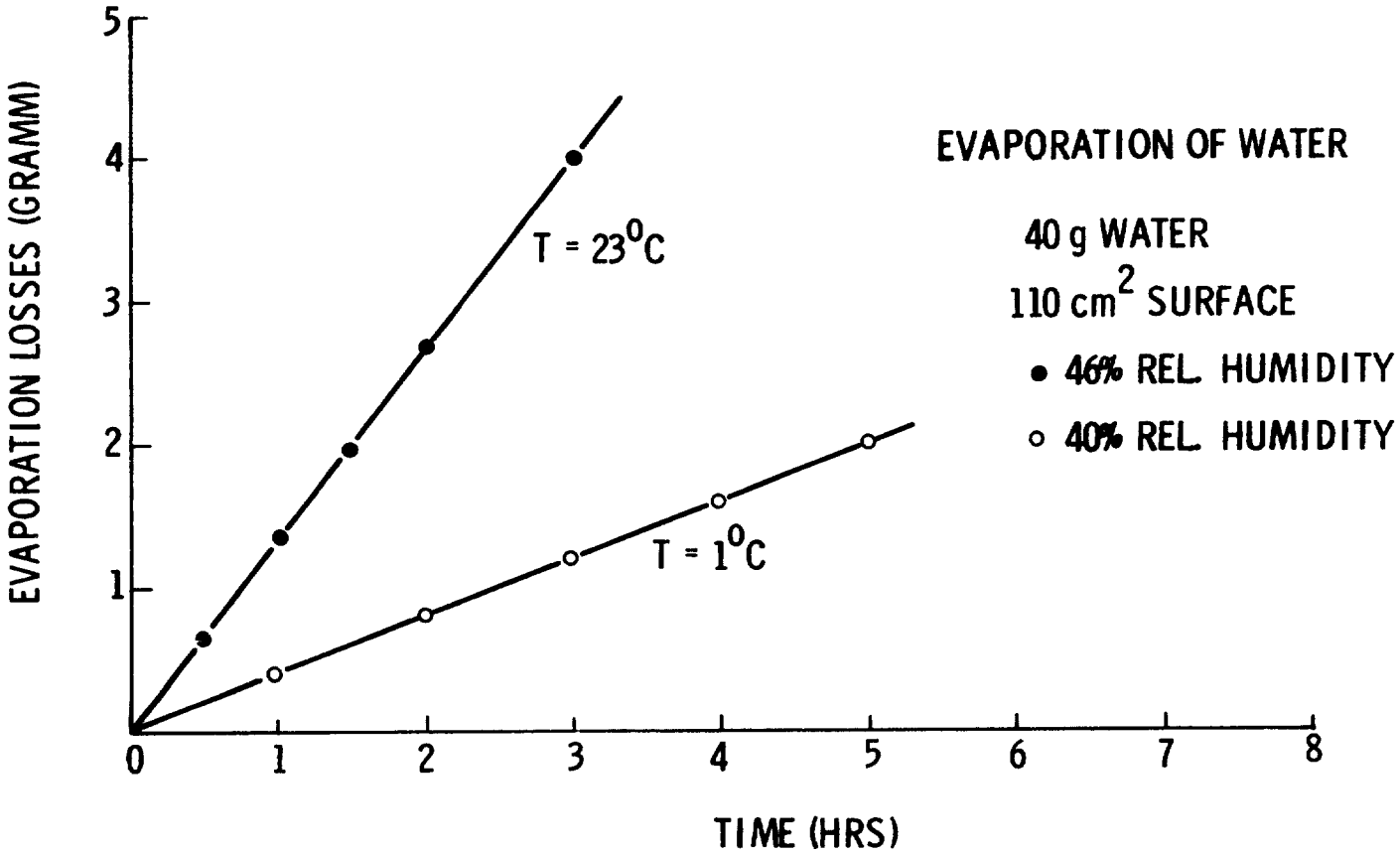


Figure 36. Experimental data of evaporation losses from a free water surface of 110 $cm^2$ area.

In summary, if one considers all secondary effects, it is found that some tend to cancel out, and in the worst case, the secondary effects will not exceed 10% of the total heat input. Thus, according to the results given in Table 12, the theory and experiment agree to within the experimental accuracy.

TABLE 12

COMPARISON OF THEORETICAL AND EXPERIMENTAL HEAT FLOW (CAL/SEC) INTO THE ICE AT t=60 MIN

| | | ONE-G | LOW-G |
|---|---|---|---|
| THEORY | | | |
| Radiation: | | 0.16 | 0.17 |
| Conduction: | | 0.04 | 0.04 |
| Convection: | | 0.24 | -- |
| | TOTAL | 0.44 | 0.21 |
| EXPERIMENT | | | |
| | TOTAL | 0.46 | 0.20 |

## 5. Conclusions and Recommendations

The returned photographic data from Skylab illustrate the importance of surface tension for low-g containerless melting. We have used the image of the solid/liquid interface of a melting ice cylinder to determine the thermodynamic heat transfer under low-gravity conditions. It can be concluded that the melting of ice on Skylab occurred without the mode of convective heat transfer. Whereas, on earth, the convective heat flow is dominant, in low-g, the latent heat of melting is mostly supplied by black-body radiation and, to only a small degree, by conduction.

Although the photographic images of the solid/liquid interface are slightly blurred by technical error, the resulting thermodynamic data are

accurate enough to completely account for all the modes of latent heat input and to study the dominant importance of surface tension in low-g melting. Since direct observations of the liquid/solid interface allows for an accurate determination of the morphological and thermodynamic states in low-g melting, it is recommended that additional investigations be performed using direct observations to study low-g solidification.

## 6. Acknowledgements

We would like to express our sincere appreciation to the crews of Skylab 3 and 4 who made, through their active participation and personal interest, these science demonstrations possible. We also deeply appreciate the never ending support of Mr. T. Bannister of Marshall Space Flight Center, Mr. J. Vellinga of the Martin Marietta Corporation (Denver), and Mr. C. Chassay of Johnson Space Center.

# V. APPRAISAL

## 1. Summary

It has been shown with this investigation that a homogeneous dispersion of immiscible alloys in bulk form can be prepared in a drop tower experiment. The physical properties of the alloys obtained were correlated with the microstructure. Especially, the electrical properties of Ga-Bi alloys were shown to be modified by the presence of a fine gallium dispersion so that a peak in the resistivity occurs. The resistivity peak is associated with a reduction in the carrier concentration and causes semiconducting properties in a temperature region above 100 K. From the experimental data obtained, we can predict the behavior of a hypothetical alloy with 0.1 μm particle size, which should have a small semiconducting energy gap of about 10 eV. A clear correlation of the controlling factors for the particle size could not be revealed but it is anticipated that this quantity is controlled by the cooling rate.

The bahavior of two immiscible liquids of different densities was illustrated in a Skylab Science Demonstration. The experiment indicated that dispersions were stable over a period of 10 hours and that the coalescence rate was at least $3 \times 10^5$ times smaller on Skylab than on earth. The recorded melting of a cylindrical piece of ice could be used to study the mode of heat transfer for containerless melting in low-gravity. The convective heat transfer was essentially eliminated on Skylab. Both experiments indicated that residual spacecraft acceleration tended to cancel out so as to give better results than predicted by first order theory.

## 2. Credits to Contract NAS8-27809

### A. Publications

1. "Shock Wave Synthesis and Characterizations of $Nb_3Sn$," J. Less-Common Metals 32, 355 (1973). With U. Roy and O. Y. Reece.

2. "The Electrical Properties of Zero-gravity Processed Immiscibles," AIAA Paper No. 74-208 (1974), with L. L. Lacy.

3. "The Electrical Properties of Zero-gravity Processed Multicomponent Materials." Proc. of the Third Space Processing Symposium - Skylab Results, Vol. 2, p. 1031, MSFC, 1974, with L. L. Lacy.

4. "The Behavior of Immiscible Liquids in Space," AIAA Paper No. 74-668, (1974) with L. L. Lacy.

5. "The Stability of Liquid Dispersions in Low-Gravity," AIAA Paper No. 74-1242 (1974) with L. L. Lacy.

6. "Observations of the Liquid/Solid Interface in Low-Gravity Melting," AIAA Paper No. 74-1243 (1974) with L. L. Lacy.

7. "The Electrical Resistivity of Gallium-Bismuth Solidified in Free Fall," AIAA Journal 13, 219 (1975) with L. L. Lacy.

8. "The Density of Indium-Bismuth Alloys," J. Less-Common Metals, 45, 163 (1976).

9. "The Precipitation of $In_2Bi$ from Supersaturated Indium," Scripta Met., in print.

10. "The Decomposition of Indium-Bismuth Solid Solutions," J. Materials Sciences, in preparation.

### B. Reports

1. "Immiscible Materials - Ground Based Studies," NASA/MSFC Technical Report, MISC-SSL-73-2, August 1973, with L. L. Lacy.

2. "Immiscible Alloys - Ground-Based Studies," First Semiannual Progress Report, UAH, June 1974.

3. "Studies on Immiscible Alloys," Second Semiannual Progress Report, UAH, October 1974.

4. "Studies on Immiscible Alloys," Third Semiannual Progress Report, UAH, March 1975.

B. Reports (Contd)

5. "Superconducting Compounds and Alloys Research," UAH Interim Research Report No. 174, June 1975.

6. "Quick-Look Report on Skylab 3 Science Demonstration TV-111, Ice Melting," NASA-MSFC, Space Sciences Laboratory, November 1973, with L. L. Lacy.

7. "Quick Look Report on Skylab 4 Science Demonstration TV-102, Immiscible Liquids," NASA-MSFC, Space Sciences Laboratory, March 1974, with L. L. Lacy.

C. Presentations

1. "The Precipitation of $In_2Bi$ from Supersaturated α-Phase," 1972 Meeting of the Alabama Academy of Sciences, May 7, 1972, Huntsville, AL. Journal of the Ala. Acad. Science 44, 200 (1973).

2. "Time-Dependent Resistivity of In-Bi Eutectic," 1972 Meeting of the Southeastern Section of the American Physical Society, November 16-18, 1972, Birmingham, AL. Bull. of the APS, Series II, 18 253 (1973).

3. "Shock Wave Synthesis of $Nb_3Sn$," 1972 Meeting of the Southeastern Section of the American Physical Society, Nov. 16-18, 1972, Birmingham, AL. Bull. of the APS, Series II, 18 262 (1973).

4. "The Electrical Properties of Zero-Gravity Processed Immiscibles," AIAA 12th Aerospace Sciences Meeting, Washington, DC, February 1, 1974, by L. L. Lacy.

5. "The Electrical Properties of Zero Gravity Processed Multicomponent Materials." Third Space Processing Symposium - Skylab Results, Marshall Space Flight Center, May 1, 1974.

6. "The Behavior of Immiscible Liquids in Space," AIAA/ASME 1974 Thermophysics and Heat Transfer Conference, Boston, MA, July 15, 1974, by M. P. L. Siebel.

7. "The Stability of Liquid Dispersions in Low-Gravity," AIAA/AGU Conference on Scientific Experiments of Skylab, Huntsville, AL, Oct. 30, 1974, by L. L. Lacy.

8. "Observations of the Liquid/Solid Interface in Low-Gravity Melting," AIAA/AGU Conference on Scientific Experiments of Skylab, Huntsville, AL, Oct. 30, 1974.

## VI. REFERENCES


1. J. T. Davies and E. K. Rideal: "Interfacial Phenomena," 2nd Edition. Acad. Press, New York, N.Y. 1963.

2. J. L. Reger: Interim Report on NASA Contract NAS8-28267, TRW-Systems Group Report No. 14725-6010-RU-00, May 1973.

3. L. L. Lacy and G. H. Otto: "The Behavior of Immiscible Liquids in Space," AIAA/ASME Heat Transfer and Thermophysics Conference, Boston, MA, AIAA Paper No. 74-668 (1974).

4. J. L. Reger and I. C. Yates: "Preparation and Metallurgical Properties of Low-Gravity Processed Immiscible Materials." Paper No. 74-207, AIAA 12th Aerospace Science Meeting, Washington, D. C., February 1, 1974.

5. L. L. Lacy and G. H. Otto: "The Electrical Properties of Zero-Gravity Processed Immiscibles." Paper No. 74-208, AIAA 12th Aerospace Sciences Meeting, Washington, D. C., February 1, 1974.

6. T. C. Bannister: "Skylab 3 and 4 Science Demonstrations," MSFC Preliminary Report, NASA TMS-64835, March 1974.

7. "MSFC Skylab Corollary Experiment Systems - Mission Evaluation," NASA TMX-64820, Marshall Space Flight Center, Huntsville, AL, September 1974.

8. M. Hansen, F. A. Shunk, R. P. Elliott, "Constitution of Binary Alloys," McGraw-Hill, NY, 1958, 1965, 1969.

9. J. L. Reger: "Experimental Development of Processes to Produce Homogenized Alloys of Immiscible Metals." Final Report on NASA Contract NAS8-27805, TRW Systems Group Report No. 18677-6019-RU-00, January 1973.

10. These samples were obtained from Dr. L. L. Lacy and Mr. I. C. Yates of MSFC Space Sciences Laboratory.

11. G. A. Chadwick: J. Inst. Met. 91, 169 (1962-63).

12. R. Becker and W. Döring: Ann. Phys. 24, 719 (1935).

13. D. Turnbull and J. C. Fisher, J. Chem. Phys. 17, 71 (1949).
D. Turnbull: J. Metals 188, 1144 (1950).

14. P. Duwez and R. H. Willens: Trans. Met. Soc. AIME 227, 362 (1963).

15. American Institute of Physics Handbook, 3rd Ed., McGraw-Hill (1972).

16. C. Kittel, "Introduction to Solid State Physics," 3rd Ed., John Wiley and Sons (1967).

17. M. Olsen-Bär and R. W. Powell, Proc. Roy. Soc., Ser. A 209, 542 (1951).

18. V. Chopra, R. K. Ray, and S. M. Bhagat, Phys. Stat. Sol. (a) 4, 205 (1971).

19. R. Hartmann: Phys. Rev. 181, 1070 (1969).

20. N. Thompson: Proc. Roy. Soc. A, 155, 111 (1936).

21. G. A. Ivanov and A. R. Regal: Chem Abstracts 49, 12908 (1955).

22. C. S. Barrett: Phys. Rev. 125, 1227 (1965).

23. W. Bridgman: Proc. Roy. Soc. A209, 525 (1951).

24. Gmelins Handbuch der Organischen Chemie, Vol. 19, Verlag Chemie, Weinheim 1964.

25. N. Kürti and F. Simon: Proc. Roy. Soc. 151, 6 (1935).

26. N. E. Phillips: Phys. Rev. 134, A385 (1964).

27. M. A. Il'ina and E. S. Itskevich: JETP Lett. 11, 218 (1970).

28. W. Buckel and W. Gey: Z. Physik 176, 336 (1963).

29. A. Eichler and J. Wittig: Z. Angew. Phys. 25, 319 (1968).

30. E. Stephens: Phil. Mag. 8, 273 (1929).

31. D. Hardin: M. S. Thesis, The University of Alabama in Huntsville. In preparation.

32. L. L. Lacy and G. H. Otto: AIAA Journal 13, 219 (1975).

33. Technical Bulletin No. L5 of the E. I. DuPont de Nemours & Co., Wilmington, Delaware.

34. A. W. Adamson: "Physical Chemistry of Surfaces," Interscience Publishers, NY 1967, p. 505.

35. Astronaut Crew Debriefings, Johnson Space Center, March 4, 1974.

36. See for example: S. Glasstone and D. Lewis: "Elements of Physicsl Chemistry," Van Nostrand Co., NY, 1962, p. 147.

37. B. J. Mason: "The Physics of Clouds," Clarendon Press, Oxford, 1957, p. 569.

38. J. Parker: Private Communication: Marshall Space Flight Center, Space Sciences Laboratory.

39. Additional computer studies on coalescence are being carried out at Batelle, Columbus. See for example: S. H. Gelles: Proceedings of the Third Space Processing Symposium - Skylab Results, Marshall Space Flight Center, Alabama (1974).

40. G. H. Otto and L. L. Lacy: "Quick-Look Report on Skylab 3 Science Demonstration SD-16: Ice Melting," Space Sciences Laboratory, Marshall Space Flight Center, November 1973.

41. Proceedings of the Third Space Processing Symposium - Skylab Results, Marshall Space Flight Center, Alabama, Report No. M-74-5, June 1974.

42. Johnson Space Center, Houston, Texas, Voice Transcripts of Skylab 3, September 20 and 21, 1973.

43. L. F. Belew and E. Stuhlinger: "Skylab - A Guide Book," National Aeronautics and Space Administration, Report No. EP-107 (1973).

44. P. G. Grodzka and T. C. Bannister, "Heat Flow and Convection Demonstration Experiments Aboard Apollo 14," Science 176, 506 - 508 (1972).

45. S. V. Bourgeois and M. R. Brashears: "Fluid Dynamics and Kinematics of Molten Metals in the Low-Gravity Environment of Skylab," AIAA 12th Aerospace Sciences Meeting, Washington, D. C., AIAA Paper No. 74-205 (1974).

46. This temperature could be read from an air thermometer close to the experiment.

47. "American Institute of Physics Handbook," 3rd Edition, McGraw-Hill, New York, 1972.

48. M. W. Zemansky: "Heat and Thermodynamics," 5th Edition, McGraw-Hill, New York, 1967, p. 100.

49. W. H. McAdams: "Heat Transmission," 3rd Edition, McGraw-Hill, New York, NY, 1954, p. 167.

50. A. Martin: 1975 NASA-ASEE Summer Faculty Fellowship Research Program, MSFC Report (to be published).

51. J. L. Reger and R. A. Mendelson: "Study on Processing Immiscible Materials in Zero-Gravity," Final Report of TRW-Systems Group for Contract NAS8-28267, June 1975.

52. G. H. Otto: "Studies on Immiscible Alloys," Third Semiannual Progress Report, UAH, March 1975.